Investigation of transport regimes in restricted geometries of ultra-pure natural heterostructures

Elina Zhakina

A thesis submitted for the degree of PhD
at the
University of St Andrews

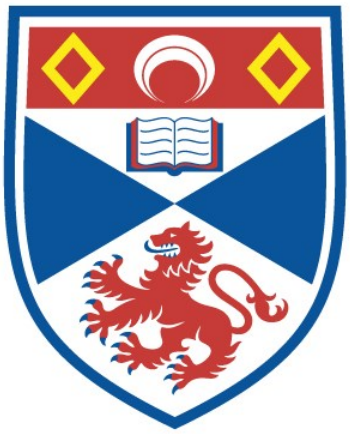

2022

Declarations

Candidate's declarations:

I, Elina Zhakina, do hereby certify that this thesis, submitted for the degree of PhD, which is approximately 35,000 words in length, has been written by me, and that it is the record of work carried out by me, or principally by myself in collaboration with others as acknowledged, and that it has not been submitted in any previous application for any degree. I confirm that any appendices included in my thesis contain only material permitted by the 'Assessment of Postgraduate Research Students' policy.

I was admitted as a research student at the University of St Andrews in September 2018.

I received funding from an organisation or institution and have acknowledged the funder(s) in the full text of my thesis.

Date: 11.11.2021 *Signature of candidate:*

Supervisor's declaration:

I hereby certify that the candidate has fulfilled the conditions of the Resolution and Regulations appropriate for the degree of PhD in the University of St Andrews and that the candidate is qualified to submit this thesis in application for that degree. I confirm that any appendices included in the thesis contain only material permitted by the 'Assessment of Postgraduate Research Students' policy.

Date: 11.11.2021 *Signature of supervisor:*

Permission for publication:

In submitting this thesis to the University of St Andrews we understand that we are giving permission for it to be made available for use in accordance with the regulations of the University Library for the time being in force, subject to any copyright vested in the work not being affected thereby. We also understand, unless exempt by an award of an embargo as requested below, that the title and the abstract will be published, and that a copy of the work may be made and supplied to any bona fide library or research worker, that this thesis will be electronically accessible for personal or research use and that the library has the right to migrate this thesis into new electronic forms as required to ensure continued access to the thesis.

I, Elina Zhakina, confirm that my thesis does not contain any third-party material that requires copyright clearance.

The following is an agreed request by candidate and supervisor regarding the publication of this thesis:

Printed copy

Embargo on all of print copy for a period of 2 years on the following ground(s):

- Publication would preclude future publication

Supporting statement for printed embargo request

The thesis includes work that has not yet been published.

Electronic copy

Embargo on all of electronic copy for a period of 2 years on the following ground(s):

- Publication would preclude future publication

Supporting statement for electronic embargo request

The thesis includes work that has not yet been published.

Title and Abstract

- I agree to the title and abstract being published.

Date: *11.11.2021* *Signature of candidate:*

Date: *11.11.2021* *Signature of supervisor:*

Underpinning Research Data or Digital Outputs:

Candidate's declaration

I, Elina Zhakina, understand that by declaring that I have original research data or digital outputs, I should make every effort in meeting the University's and research funders' requirements on the deposit and sharing of research data or research digital outputs.

Date: 11.11.2021 *Signature of candidate:*

Permission for publication of underpinning research data or digital outputs

We understand that for any original research data or digital outputs which are deposited, we are giving permission for them to be made available for use in accordance with the requirements of the University and research funders, for the time being in force.

We also understand that the title and the description will be published, and that the underpinning research data or digital outputs will be electronically accessible for use in accordance with the license specified at the point of deposit, unless exempt by award of an embargo as requested below.

Embargo on all of electronic files for a period of 2 years on the following ground(s):

- Publication would preclude future publication

Supporting statement for printed embargo request

The data relates to work that has not yet been published.

Title and Description

- I require an embargo on the title and description

Date: *11.11.2021* *Signature of candidate:*

Date: *11.11.2021* *Signature of supervisor:*

Abstract

This thesis describes investigations into the origins of the unconventional electrical transport of the non-magnetic delafossite metals $PtCoO_2$ and $PdCoO_2$ and the magnetic delafossite metal $PdCrO_2$ using focused ion beam microstructuring techniques. These compounds are among the highest conductivity materials known, with an extreme purity of up to 1 defect in 120,000 atoms. This remarkable purity, together with the hexagonal Fermi surface, opens the possibility of studying novel regimes of mesoscopic physics.

This work is split into two parts. In the first part, I will review the key properties of non-magnetic delafossite metals and the application of focused ion beam microstructuring to transport measurements within low resistivity materials. The related experimental chapter describes an investigation which uses the high energy electron irradiation investigation to probe the effects of a non-circular Fermi surface on the transport within bars and four-terminal, square-shaped junctions inside the ballistic regime.

The other studies were concentrated on the magnetic delafossite metal $PdCrO_2$. I will describe a new method of microstructure preparation which was created for $PdCrO_2$ transport studies but is widely applicable to other materials. This material obeys the Planckian bound at a wide range of temperatures between 200 K and 500 K. The accompanying experimental chapter details an investigation by high energy electron irradiation of the origin of this behaviour. The new method of mounting microstructures also allows, for the first time, the study of studying unconventional transport regimes in $PdCrO_2$.

Acknowledgements

This work has been carried out at the Max-Planck-Institut für Chemische Physik fester Stoffe in Dresden over four years and would not have been possible without colleagues and friends to whom I would like to express my gratitude.

First and foremost, I would like to thank my supervisor, Andy Mackenzie, for guiding me through this PhD. Despite a very busy schedule, he was always very willing to find time for scientific discussions. His unique take on physics with more words and imagination over equations has given me a new perspective on my understanding. I also greatly appreciate his support during these years and, of course, opening the 'world of hiking' to me.

The work presented in this thesis would not have been possible without the help and support of our collaborators from the Laboratory for Irradiated Solids Ecole Polytechnique in France. In particular, I am grateful to Marcin Konczykowski, Jeremie Lèfevre and Romain Grasset, all of whom worked extremely hard to facilitate some challenging irradiation experiments. Oliver Cavani provided excellent and tireless technical support.

Special thanks go to my friend and 'delafossite-team' member, Philippa McGuinness, whose support and help during our experiments made my PhD years better. I appreciate not only her clear explanations but also her patience and dedication to answering any question. We spend many hours discussing, measuring together and developing protocols for making microstructures suitable for irradiation, for making the delafossite squares.

I would also particularly like to thank another 'delafossite team' member Veronika Sunko, who also taught me a lot of physics and experimental techniques during these years. Our irradiation beam times were only possible because of her clear explanation and patient teaching of the initial electron irradiation protocols they developed with Philippa. I greatly enjoyed working with Veronika and Philippa during these times and our joint establishment of the excellent post-beamtime wine and steak tradition.

I very much appreciated the theoretical discussion with Sean Hartnoll,

who gave a clear introduction to the Planckian dissipation problem.

I would like to thank the administrative staff at our institute, Claudia Strobach and Uta Prautzsch, who have always been very helpful in sorting out every small problem. Thanks must also go to the CM-CDT administrative staff that provided excellent online help with any questions.

Special thanks should go to Stanislav Nikitin, whose cheerful support helped me a lot during hard experimental times. He proposed the idea of a neutron scattering experiment in $PdCrO_2$, and I hope for a fruitful future collaboration.

All the experimental work was possible only due to the fantastic technical support available at the institute. I would like to thank Renate Hempel-Weber and Heike Rave for their invaluable work, which allowed me continue my experiments even during the COVID-19 pandemic. Special thanks also to Sebastian Seifert for teaching me the art of lithography and helping in a clean room. In particular, I would like to thank Markus König for his advice and effort in maintaining the FIB instruments.

I very much appreciate the friendly work environment in the group, which is possible because of the old and new group members like Mark Barber, Maja Bachmann, Veronika Sunko, Alexander Steppke, Dan Sun, Jack Bartlett, Igor Markovic, Po-Ya Yang, Belen Zuniga, Edgar Abarca Morales, Hilary Noad, Alex Stern, Dorsa Fartab, Cliff Hicks, Kim Modic, Nabhanila Nandi, Ekta Singh, Eteri Svanidze, Haijing Zhang and lots of others. Fabian Jerzembeck, thank you for online and 'safe distance' outside coffee talks, making pandemic times easier and more joyful. Your wise advice also helped a lot during my experimental work.

Last but not least, I would like to thank Seunghyun Khim for growing the world's cleanest and prettiest oxide metals, $PtCoO_2$ and $PdCrO_2$, which enabled the ballistic transport studies presented here and Microstructuring Quantum Matter group members, Tino Zimmerling and Kent Shirer, for the help in developing a new method of microstructure fabrication.

Contents

Chapter 1

Introduction

Nature provides various materials within which the different forms of the interactions lead to a wide range of possibilities including insulators, semiconductors, semimetals and metals. The main aim of condensed matter physics is to understand these interactions and the wide variety of collective behaviour resulting from them. The microscopic interactions between the fundamental excitations of the solids, e.g. electrons, phonons, magnons etc., lead to different macroscopic effects that can be observed, for example, in transport measurements. One method of characterising the conductivity is by the mean free path, the average distance travelled by a conduction electron before a momentum-relaxing scattering event. In most metals, scattering from defects ensures this length scale is very short, often only a few interatomic distances. However, a small number of materials exhibit a remarkably high conductivity. The mean free path can reach near macroscopic scales of tens or even hundreds of microns. With care, elemental metals, such as copper and gold can be prepared with extremely small defect concentrations, leading to mean free paths in the millimetre scale at low temperature. The electronic structure in these elements is strongly three-dimensional, allowing some classes of physics to be accessed, but preventing study of ultraclean materials in low dimensions where interactions are expected to have stronger effects.

In the late 20th century, progress in fabrication technologies allowed the creation of semiconductor heterostructures, where a 2D electron gas (2DEG) is formed at the interface between two semiconductors with different bandgaps. Initially, the 2DEG formed at the surface interface had relatively low mobility. However, in the 1980s and 1990s, the mobility of 2DEGs within GaAs-based heterostructures increased by a factor of over 10 000 [1]. Thus, ultrapure heterostructures and other ultra conductive materials received high interest in research due to the mean free path, typically tens of microns, achieved in such structures.

The micron-scale mean free paths were obtained in graphene by 2010, causing intense study of its electronic transport [2, 3]. The Weyl and Dirac semimetals recently have been developed as another class of ultrahigh mobility materials with evidence of a novel mechanism which limits backscattering [4].

In this thesis, I dedicated myself to studying three compounds from a class of high conductivity materials different from those described above: the delafossite metals $PtCoO_2$, $PdCoO_2$ and $PdCrO_2$. The large majority of layered delafossite materials are insulators or wide-gap semiconductors. A small number of them are metals with very low resistivity. For example, the resistivity of $PdCoO_2$ and $PtCoO_2$ at room temperature is smaller than that of almost every metal except gold, silver and copper. All three compounds consist of metallic Pd or Pt layers separated by insulating spacer layers of transition metal oxides. In $PdCoO_2$ and $PtCoO_2$ the Co is in its low spin state and the spacer layers are band insulating. However, in $PdCrO_2$ the CrO_2 layers are Mott insulating, so nearly free and Mott localised electrons exist in alternating layers, forming natural heterostructures.

Although $PtCoO_2$ and $PdCoO_2$ were first synthesised almost fifty years ago, [5], they have only been recently carefully studied. Several advanced experimental techniques are required to fully establish the fundamental physical properties of new classes of materials. For example, characterisation of the Fermi surface is vital to establish essential quantities like the mean free

path. In the last few decades, the resolution of characterisation techniques has dramatically improved. Of particular relevance to the materials investigated in this thesis are the improvements to angle-resolved photoemission spectroscopy (ARPES) that can directly characterise the Fermi surface and dispersion relation, allowing determination of properties such as the Fermi velocity. This technique is particularly well-suited to study of materials with a quasi-2D electronic structure like the delafossites.

Recently, focused ion beam (FIB) scultping has created many new and exciting opportunities for investigating materials. This comparatively young technique has just started to transform traditional sample fabrication methods. In principle, the FIB is a unique tool that can precisely remove material while preserving the crystalline quality of the remaining material. Lamellae of any desired orientation can be cut from single crystals, a capability that has seen widespread use in the preparation of samples for transmission electron microscopy.

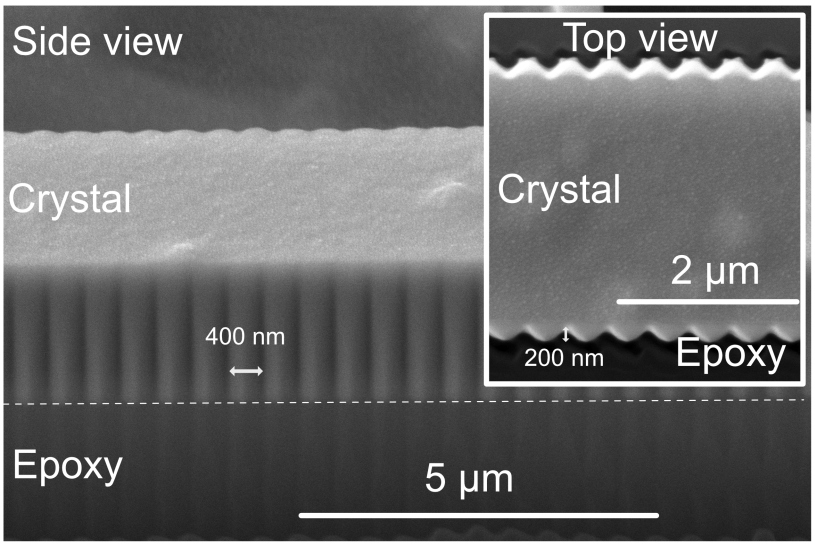

Figure 1.1: An example of the possibilities brought by FIB sculpting: An SEM image of $PtCoO_2$ bar with 400x200 nm corrugations cut using a FIB.

However, the potential use of FIB is not limited only to lamela cutting. Various physical regimes can be implemented by tuning the sample dimen-

sions across an intrinsic, characteristic length scale of the system. Therefore, FIB becomes an indispensable tool for such studies. The example of possible microstructuring of a $PtCoO_2$ bar to produced corrugated boundaries is shown in fig. 1.1. Because FIB sculpting can go down to tens of nanometer scales, once the challenges related to a material cut discussed in Chapter 3.2 are overcome, the microstructuring procedure is limited only by the set goals and user's imagination. However, the FIB microstructuring of materials has only been developed within the last decade. It is still a relatively new technique with many open questions and opportunities. In this respect, I will show new ways of using microstructuring techniques in Sections 3.3 and 6.1.

Microstructured devices not only provide accurate resistivity measurements but also offer the possibility of investigating mesoscopic transport regimes, which are difficult but not impossible to achieve in many materials. In the mesoscopic regime, the sample shape and dimensions become relevant parameters for the observed behaviour as the device's size is shorter or comparable with the mean free path. Throughout this thesis, form and size influence will be an underlying theme when studying ballistic regimes in non-magnetic $PtCoO_2$, $PdCoO_2$ (in the first part of my thesis) and magnetic $PdCrO_2$ (in the second part of my thesis) in various devices geometries.

The thesis consists of two parts. The first one explores non-magnetic delafossite metals as follows:

Chapter 2 outlines the properties of non-magnetic delafossite metals $PdCoO_2$ and $PtCoO_2$ and the background physics of conduction of electrons in metals which are most relevant for understanding the studies described within later chapters.

Chapter 3 gives a basic overview of the sample preparation procedure. I discuss the FIB and the effects of FIB irradiation on the target material, the 'classical' and 'new' techniques used to create microstructures and methods that we use to measure the resistivity of microstructures made from ultrapure delafossite metals. The high energy irradiation experiment used to introduce additional defects to the delafossite metals is also outlined.

Chapter 4 investigates ballistic transport in $PtCoO_2$ thin bars and within square-shaped junctions, which were structured using the FIB to have a device's width approximately equal to the electron mean free path, bringing them into the ballistic regime. I studied the ballistic decay in both these types of devices in $PtCoO_2$, decreasing the mean free path of electrons by high energy electron irradiation.

The second part of my thesis is dedicated to the properties of the magnetic delafossite metal.

Chapter 5 describes the properties of magnetic delafossite metal $PdCrO_2$ and the background physics of Planckian dissipation, which are most relevant for understanding the studies presented in Chapter 6.

Chapter 6 describes the 'new free-standing method' of creating microstructures of $PdCrO_2$. In this chapter, I investigate Planckian dissipation in $PdCrO_2$ and its dependence on elastic and inelastic scattering, the nature of unconventional transport regimes and the influence of the exotic coupling between conductive and magnetic layers on magnetotransport.

Chapter 7 gives conclusions and an outlook for future work.

Chapter 2

Non-magnetic delafossite metals: $PtCoO_2$ and $PdCoO_2$

The delafossite metals are a new class of ultrahigh purity metals. The combination of the ultrahigh purity and simplicity of the band structure make these metals a model system for the study of electrical transport within low resistivity materials. I have performed some such studies, in both as-grown crystals and crystals that I have deliberately disordered using high energy electron beam irradiation. In this chapter I will first review the properties of the two non-magnetic delafossite metals, $PtCoO_2$ and $PdCoO_2$, that I have worked with, and introduce background physics relevant to those studies. In the second part of the chapter I will give introductions to the main experimental techniques that I have used.

In the most general terms, delafossite materials have the generic formula ABO_2, where A is either Pt, Pd, Ag or Cu and B is a transition metal such as Co, Cr, Rh, Fe, Sc, Ga, Al, Ga, Tl or In. Most of the delafossite materials are insulators or semiconductors. As shown in fig. 2.1, the A sites form triangularly coordinated planes between layers of B site octahedra, with the A site cations linearly co-ordinated with the oxygen cations located at the octahedra vertices [5]. Most delafossites are insulating or semiconducting and frustrated magnetism is often present due to the triangular co-ordination of

the B site in-plane [5].

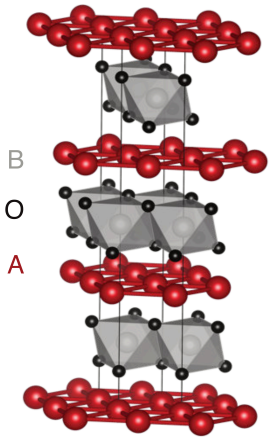

Figure 2.1: The delafossite crystal structure. The A-site cations are the large red spheres and the oxygen cations are the smaller black spheres. The grey B-site cations are within the octahedra.

The synthesis of 18 delafossite materials was published in 1971 [6, 7, 8] by Shannon and co-workers. In Pt and Pd based oxides, they found highly conductive metallic behaviour with the resistivity of 2 $\mu\Omega$cm in $PdCoO_2$ and 3 $\mu\Omega$cm in $PtCoO_2$ at 300 K in the *ab* plane. The values of these remarkably small resistivities are smaller than those for pure Pt or Pd metals. They also noted a high anisotropy of resistivity: the ratio between the *ab* plane and *c*-axis resistivities was over 1000 for $PtCoO_2$ and $PdCoO_2$. Despite these remarkable results, the delafossite metals were not paid too much attention for about two decades. In 1997 the first measurements of the temperature dependence of the resistivity were reported by Tanaka *et al*. [9, 10]. However, the in-plane resistance ratio (ratio of the room temperature resistivity and in-plane resistivity at 4 K) for this work was a modest 10. In 2007 Takatsu *et al*. grew new crystals of $PdCoO_2$ with increased in-plane resistance ratios of over 400 [11]. And then the growth of the first single crystal of the related compound $PdCrO_2$, with in-plane resistivity ratios of over 200, was reported in [12].

In delafossite metals transport of the electrons occurs through the metallic A layers, and the BO_2 layers are insulators. This quasi 2D conduction makes delafossite metals behave like natural heterostructures. However, to predict the correct band structures and Fermi velocities, electronic correlations in

the insulating layers must be taken into account. These correlations may play an important, but not completely understood, role in high conductive electronic transport in delafossite metals.

2.1 Resistivity and scattering in ordinary metals

To better understand the unusual transport properties of delafossite metals, I have to discuss the origin of the temperature dependence of the resistivity in ordinary metals. In a free electron gas, the simplest kinetic model assumes that the microscopic behaviour of electrons may be treated classically. This approach was proposed in 1900 by Paul Drude [13]. Formula (2.1) shows the Drude conductivity definition, where τ is the relaxation time, m_* is the effective mass of the electrons, and n is the density of electrons.

$$\sigma = \frac{ne^2\tau}{m_*} \tag{2.1}$$

The kinetic method determines the conductivity of Fermi gas at a specific temperature, assuming all scattering processes being identical. The only property that this theory considers is a probability that the particle will make a collision in the infinitesimal time interval. I can define this theory as a purely classical one, and Drude made incorrect assumptions about the nature of electronic scattering. However, the basic form of eq. 2.1 can still be used to parameterising semiclassical transport in quantum materials, and is widely used in the modern literature. Sommerfeld applied the principles of quantum mechanics to classical free electron theory.

According to quantum theory, specifically the Pauli principle, the free electrons occupy different energy levels, up to the Fermi level. Electrons at the Fermi level have the Fermi velocity v_F. At the origin of wave-vector space (k-space), electrons are sitting on sphere of radius k_F. This sphere is also known as the Fermi sphere. If we apply an electric field E along the

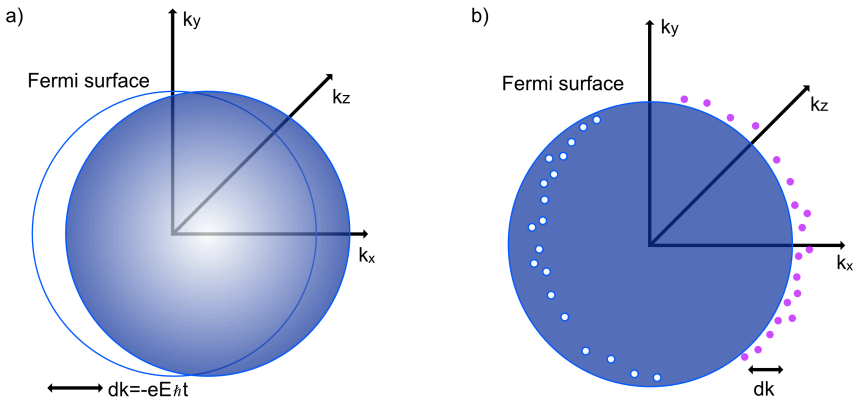

Figure 2.2: a) The shift of the Fermi surface in k-space under electrical field E. b) quasiparticles as excitations model

x-direction, the Fermi surface shifts along this direction as force eE acts on each electron (fig. 2.2a). In the Drude-like picture each state in the Fermi sphere is displaced by $\hbar dk$ = -$eEdt$. However, this is an entirely wrong picture from the quantum theory point of view.

We can consider the filled Fermi sea at T = 0 as inert, so it is like a vacuum (fig. 2.2b). Temperature and external fields excite special particle-antiparticle pairs, illustrated as small circles and holes in fig. 2.2b respectively. It is important to note here that the energy scale of the field is low, and excitations take place near the Fermi surface, i.e. $dk<<k_F$. Compared to a quasi electron with the same wave-vector k, the quasi-hole has opposite charge and spin, opposite mass and therefore opposite kinetic energy, and the same group velocity $v = d\epsilon/\hbar dk$, where the ϵ-k relation is that of the plane-wave states.

To simplify the derivation of conductivity, I will consider the 2-D case. By applying electric field E, I excite quasi-electrons and quasi-holes from the vacuum, and thus, the number per unit area of quasi-particles is:

$$n_{qe} = n_{qh} = \frac{k_F eE\tau}{h}, \tag{2.2}$$

where, n_{qe} is the number per unit area of quasi-electrons, and n_{qh} is that of

quasi-holes.

The current from the quasi-electrons can be determined by the number of them multiplied by the average component of their velocity along the direction of the applied electric field:

$$j_{qe} = j_{qh} = \frac{k_F e^2 E v_x \tau}{h} \tag{2.3}$$

As the charge and the average velocity of quasi-holes are opposite to that of the quasi-electrons, the current of quasi-holes j_{qh} is the same as the current of quasi-electrons j_{qe}. Thus, both types of excitations add to the total current instead of cancelling each other out. The total conductivity can be calculated by:

$$\sigma = \frac{j_{tot}}{E} = \frac{2k_F e^2 \tau v_x}{h} = \frac{e^2 k_F l}{h} = \frac{ne^2\tau}{m}, \tag{2.4}$$

using the general relation for the mean free path $l = v_F\tau$ and for the free electron ones $n = \frac{k_F^2}{2\pi}$ and $v_F = \frac{\hbar k_F}{m}$.

Thus, the quantum theory gives identical (2.1) to the Drude theory definition of conductivity. So purely classical theory and quantum one give the same answer, even though one of the theories is incorrect. However, this is only the case for a sphere. Fermi surfaces in solids are not always spherical. In this case, the Drude-like picture is wrong, and the conductivity must be calculated using a Fermi surface integral. After that is done, the parameters are sometimes averaged across the whole Fermi surface(s) and expressed using the form of 2.1, so it is important to know that seeing something written in the form of 2.1 does not imply that the actual material has a simple spherical Fermi surface.

2.1.1 Electron-phonon scattering

To bring this electron model closer to real metals, I will consider the positive ion cores in the solid through a periodic potential. There are temperature dependent vibrations, known as phonons.

2.1 Resistivity and scattering in ordinary metals

In ordinary metals, a considerable contribution to electrical resistivity arises from the scattering of electrons by lattice vibrations and defects. At temperatures higher than the Debye temperature, the quantisation of phonons is irrelevant, because all the phonon modes are excited. The scattering is proportional to the square of the amplitude of the fluctuations of the ions about their equilibrium state. Thus the scattering is almost elastic. Each scattering event consists of emitting or absorbing a phonon with a short wavelength. In every scattering event, the momentum changes significantly. The electron can not change energy more than Θ_D, but the ionic vibration amplitude, and hence the scattering cross-section, is proportional to temperature. Therefore, the resistivity of the metal will be proportional to T (2.5) [14].

$$\rho \sim T,\ T > \Theta_D \tag{2.5}$$

Below the Debye temperature, the electron-phonon interactions play a significant role. At low temperatures, the resistivity of metals falls very rapidly. Taking into account an additional estimate of a Debye phonon spectrum, an approximate solution of the Bloch-Boltzman equation will give the Bloch-Grüneisen formula (2.6) [14].

$$\rho \sim T^5,\ T << \Theta_D \tag{2.6}$$

The simple presentation of the electron-phonon scattering in fig. 2.3, can explain the temperature dependence of the resistivity in (2.6). In the scattering process, an electron will emit or absorb a phonon. Thus, it will change its state with wave vector k and energy E_k to the state with wave vector k' and energy E'_k. Due to energy and quasimomentum conservation, the energy of the phonon should satisfy the following relation:

$$E_k = E'_k \pm \hbar\omega_{(k-k')} \tag{2.7}$$

This relation limits the possible wave vectors q of the phonons capable of participating in scattering processes:

$$\omega(q) = \pm\frac{1}{\hbar}(E_{k+q} - E_k) \tag{2.8}$$

When the temperature is lower than the Debye temperature $\hbar\omega < k_B T$ phonons have wave vectors q an order of $k_B T/c\hbar$ or less. Thus, all the phonons that can participate in the scattering process will be inside the purple sphere in fig. 2.3.

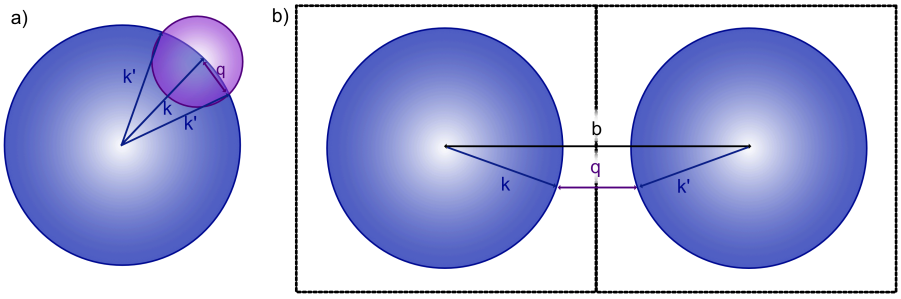

Figure 2.3: a) Electron-phonon scattering. At temperatures $T < \Theta_D$ phonons, that can participate in scattering process, have wave vectors in the sphere with diameter $k_B T/c\hbar$, where c is speed of sound in the material. b) Umklapp electron-phonon scattering.

According to the Debye law, the total density of phonons is proportional to T^3. Each phonon has small momentum proportional to T so that the electron can change direction by a small angle (fig. 2.3a) at each scattering process. If the angle is small, the scattering depends on the square of the angle. Thus, it gives another factor of T^2. The overall effect is proportional to T^5 [14]. A smooth curve describes the temperature behaviour of resistivity between high and low temperatures. In 1933 Grüneisen showed that the experimental data for a wide range of metals fit this curve remarkably well [15].

The above example of scattering describes the electron-phonon process only inside one Brillouin zone, which is also called a normal process. If a phonon has sufficient momentum, it can transfer an electron to the Fermi surface of the neighbouring band. In the simplest case, sketched in fig. 2.3b, there is a minimum phonon q-vector at which Umklapp processes become

possible. Thus, for the closed Fermi surface the activation energy for the umklapp process is $c\hbar q$, where c is the speed of sound in the material. With the nearly free electron model, there is a large change in the velocity of electron due to the umklapp scattering. Metals, free of defects, have finite conductivity because the umklapp scattering can occur. The q-vector shown in fig. 2.3a is a minimum wave vector of a phonon that can participate in an umklapp process. At temperatures below those corresponding to the energy of q-vector ($k_B T_U = c\hbar q$), the contribution from umklapp scattering to the transport of electrons should drop exponentially as the number of phonons participating in the scattering is proportional to $exp(-\hbar\omega_{min}/k_B T)$. Thus the resistivity is $\sim exp(-T_U/T)$ [14, 16]. The exponential rise of the conductivity at low temperatures was observed in ultra-clean alkali metals [17, 18].

2.1.2 Electron-defect scattering

Beside scattering electrons by phonons, a considerable contribution to electrical resistivity arises from defects. Generally, crystalline defects mean any region where ions' microscopic arrangement is different drastically from that of a perfect crystal. Defects in crystals come in a seemingly endless variety. But here, I will mention two more essential types of defects that are significant for my experiment: vacancies and interstitials. These are the point-like defects consisting of the absence of ion or the presence of extra ion.

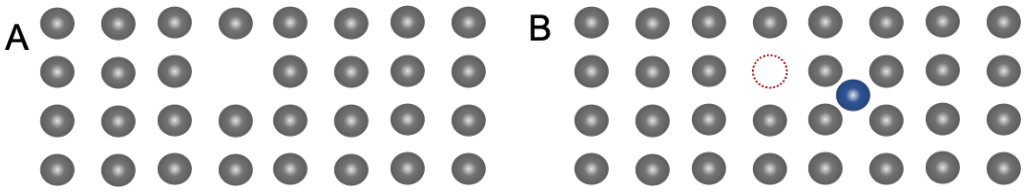

Figure 2.4: A: Bravais lattice with Schottky defect. B: crystal with Frenkel--type defects: equal number of vacancies (red) and interstitials (blue)

The simplest kind of defect is a vacancy or a Schottky defect on a monoatomic Bravais lattice (fig. 2.4A). It occurs when a Bravais lattice site has no ion

associated with it. In general, of course, there could be many types of vacancies, for example, in polyatomic crystals. There is also the possibility of an extra ion occupying a region not occupied in a perfect crystal; in other words, an interstitial. The case of a defect consisting of one vacancy and one interstitial atom is known as a Frenkel pair defect (fig. 2.4B) [16, 14].

The question that I would like to answer here is how electron scattering from impurities happens in metals. Most types of defects and impurities are ionised. In metals, the wavelength of electrons at the Fermi surface is usually comparable to the size of the defects so that diffraction can not attenuate the scattering processes.

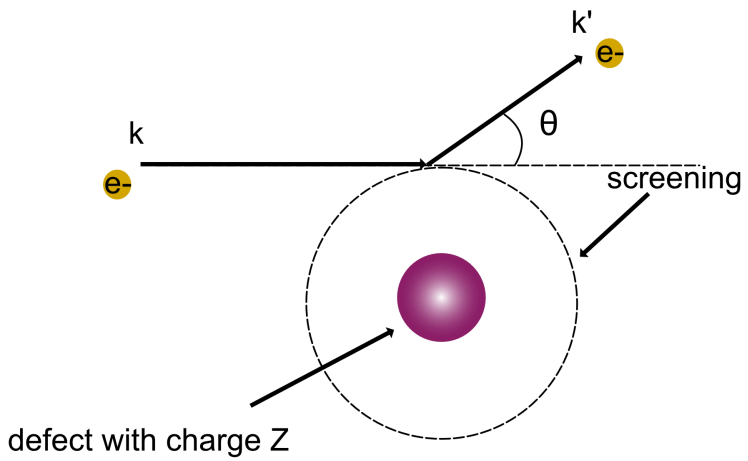

Figure 2.5: The schematic of the scattering of electron by a defect with charge Z.

To simplify the case, I will consider the scattered electrons as free ones. Fig. 2.5 illustrates the scattering of the electron by the defect with charge Z. Thus, the scattering power depends only on the form of a potential associated with a defect. Because metals have conduction electrons, it is impossible to have a bare electrostatic charge. We have to take into account screening by these electrons. The impurity potential will fall off much more rapidly to zero at large distances than the simple Coulomb field Ze/r emanating from the charge of the defect Z [19]. Thus, this defect creates the potential:

$$\phi = -Ze\frac{e^{-\kappa r}}{r}, \tag{2.9}$$

where κ is the inverse Debye radius, equal to:

$$\kappa = (4\pi e^2 \frac{\delta n}{\delta \mu})^{1/2} \tag{2.10}$$

The differential cross-section per unit solid angle, which characterises the probability of scattering through the angle θ between k and k' states is [14]:

$$Q = (\frac{2mZe^2}{\hbar^2})^2 (\frac{1}{(|k-k'|)^2 + \kappa^2})^2 \tag{2.11}$$

Electrons screen the Coulomb potential at the Debye radius κ^{-1}, which can be estimated as of order the interatomic distance ($\kappa \sim a \sim 10^{-8} cm$). Thus, for describing the contribution of impurities to the resistivity, we can consider scattering of electrons by hard spheres. In the simplest ionic picture that I presented, the electron scattering process is elastic and isotropic in direction. If n_i is the density of impurities in metal, the electron travels between collisions by the distance:

$$l \sim (n_i Q_{eff})^{-1} \tag{2.12}$$

where Q_{eff} is the effective scattering cross-section. Using the Drude formula 2.1 we can derive the conductivity [19]:

$$\sigma \sim \frac{ne^2\tau}{m_*} \sim \frac{ne^2 l}{m_* v} \sim \frac{ne^2}{p n_i Q_{eff}}, \tag{2.13}$$

where p is the electron momentum.

Thus the impurity contribution to the conductivity is independent of the temperature. This contribution gives the minimum resistivity of the metals at low temperatures.

The next question that comes to the mind is how the total resistivity of a metal behaves if there are several scattering sources? If the presence of one mechanism does not alter the other mechanism, then it is reasonable to

postulate that the total collision rate will be given by the sum of the collision rates due to separate mechanisms. In addition, we assume a k-independent relaxation time for each mechanism. Since the resistivity is proportional to $1/\tau$, for the total resistivity we will have:

$$\rho = \frac{m_*}{ne^2\tau} = \frac{m_*}{ne^2\tau_1} + \frac{m_*}{ne^2\tau_2} + ... = \rho_1 + \rho_2 + ... \tag{2.14}$$

This proposition is known as Matthiessen's rule.

2.1.3 Electron-electron scattering

Going beyond the independent electron approximation, we should also consider scattering between the electrons. The interactions between electrons were considered first by Landau in Fermi liquid theory, which describes the electrons in a solid as quasiparticle excitations that arise from liquid with electron-electron interactions [16].

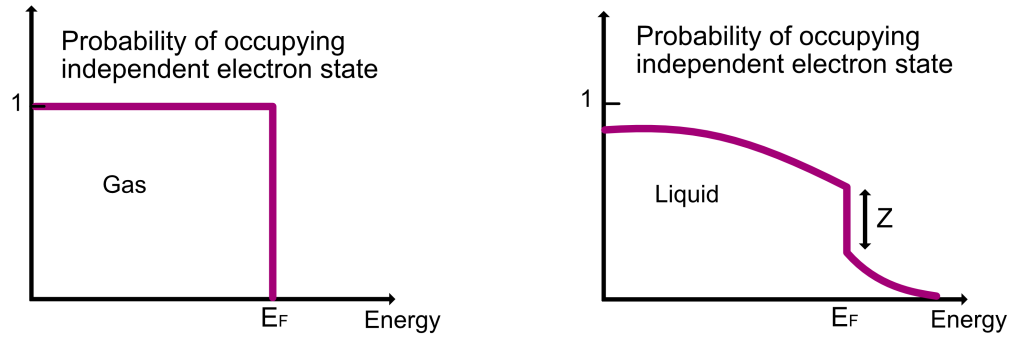

Figure 2.6: The distribution function for independent electrons on the left and for Fermi liquid on the right. Z quantifies the interaction strength between the electrons

The quasiparticle states emerge continuously from the stationary independent electron states, with a slow introduction of interactions. The quasiparticles conserve the flavour of the fundamental electrons by preserving the Fermi surface. The Fermi-Dirac distribution shown in fig. 2.6 evolves under the electron-electron interactions. The value of the Z parameter charac-

terises the interaction strength: the stronger the interaction is, the smaller Z. The distribution function for the electron liquid has some similarities with a thermally broadened gas distribution function, but one crucial difference is that there is still a discontinuity of the derivative at the non-interacting Fermi surface. Therefore, the possible number of k states for an electron to scatter into will be smaller with lower T [14, 16]. All the complications of the spread of occupancy caused by the interactions have disappeared, and we have a straightforward distribution function near the Fermi surface, if we describe the system not in terms of electrons but quasiparticles formed from the superposition of single electron states, as the excitations determine the properties of metals in the vicinity of E_F. Thus, a fraction T/T_F of electrons around the Fermi surface (with $T << T_F$) participate in the transport in a metal. This is the connection to the original system, which can be explained by adiabatic continuity. The effect of correlation between the electrons can be seen in the effective mass of electron m_e higher than the free electron mass.

Therefore, the scattering probability of the interacting electrons can be treated independently, taking a similar approach to the scattering mentioned above sources and added in parallel to derive the overall scattering probability,

$$\frac{1}{\tau} = \frac{1}{\tau_{ph}} + \frac{1}{\tau_d} + \frac{1}{\tau_e}, \tag{2.15}$$

where τ_{ph} is electron-phonon scattering, τ_d is electron-defect scattering, and τ_e is electron-electron scattering.

The electron-electron scattering process shown in fig. 2.7 can be presented as a perturbation to a filled Fermi sea by introducing a quasiparticle with energy $E'' > E_F$. A quasiparticle with energy E'' above the Fermi surface scatters off another one from the Fermi sea and drops energy E_0 to create an additional particle-hole pair. Only states within k_BT around the Fermi surface participate in the scattering. The probability of a quasiparticle decay in a 3D case can be calculated as:

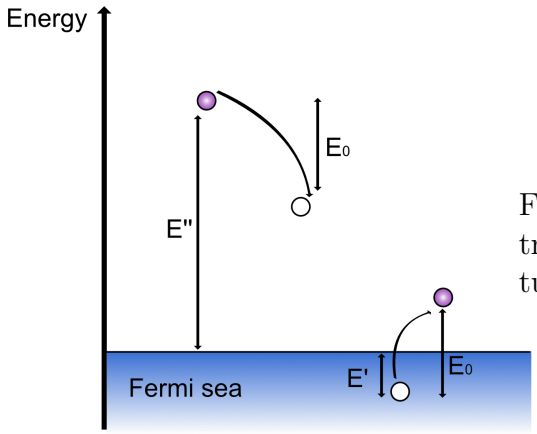

Figure 2.7: Schematic of electron-electron scattering in a qausi-particle picture.

$$\frac{1}{\tau_e} = A_{ee}\frac{1}{\hbar}\frac{(k_BT)^2}{E_F}, \tag{2.16}$$

where A_{ee} is a constant of order 1 – 100 and the ratio $\frac{k_BT}{E_F}$ indicates the fraction of phase space available for the initial and final states [16].

The same approach can be extended to the 2D case. However, in a planar geometry, the phase space available for scattering introduces an additional factor to the decay rate. At the temperatures $k_BT << E_F$ the 2D scattering rate is given by [20],

$$\frac{1}{\tau_{e(2D)}} = -\frac{1}{2\pi\hbar}\frac{(k_BT)^2}{E_F}ln(\frac{k_BT}{E_F}) \tag{2.17}$$

For the typical metal, E_F is of the order of a few eV, and at room temperature, k_BT is of the order of 10 meV. If $A_{ee} \sim 1$, for both 2D and 3D cases of Fermi surface τ_e is of the order of 10^{-11} s. However, relaxation times for other scattering processes are of the order of 10^{-14} s [16]. Therefore, at room temperature, the electron-electron scattering has a negligible effect on resistivity. As the scattering rate falls as $1/T^2ln(k_BT/E_F)$ with temperature, it has a minor impact throughout the temperature range down to the lowest achievable temperature. At very low temperatures where the phonon contribution is insignificant due to few thermal vibrations and when the impurity scattering is significantly low, a prominent signature of e-e scattering could

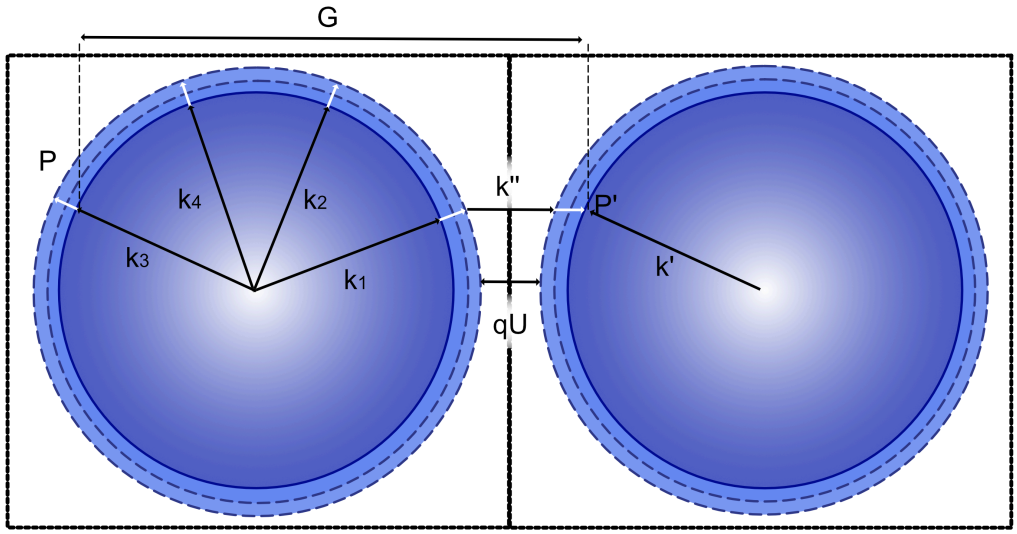

Figure 2.8: The electron-electron U-process involving two electrons with wavevectors k_1 and k_2 given by $k_1 + k_2 = k_3 + k_4 + G$, where $k_4 - k_2 = k''$. The black (white) arrows illustrate the minimum (maximum) wavevector available for a U-process.

be seen in the resistivity. For example, Sr_2RuO_4 has a T^2 dependence of the resistivity up to almost 25 K [21].

Similar to the case of electron-phonon interaction, the electron-electron scattering also possesses normal and umklapp processes. The electron-electron umklapp process, shown in fig. 2.8 and can be expressed as $k_1 + k_2 = k_3 + k_4 + G$ or similar to the phonon-electron umklapp shown in fig. 2.3b as $k' = k_1 + k''+G$. Only an electron in a region $2k_BT$ can provide the change in wave-vector k'', therefore, the number of electrons for the umklapp is compelled by $\omega(k_F)$ - $k_BT/\hbar < \omega(k'') < \omega(k_F) + k_BT$. However, there is a difference between the electron-electron and the electron-phonon umklapp processes. The temperature in electron-electron U-process cannot be used as a parameter to tune the number of available electrons as for phonons in the electron-phonon case, as only the electrons near the Fermi surface can participate.

The temperature dependence is contained in the same phase space argument for the normal scattering process giving a T^2 dependence. For the

closed Fermi surface, electron-electron umklapp is possible only for $k_F \sim G/2$, because when $k_F << G/2$, the electrons do not have sufficient wave vector to scatter to the next Brillouin zone. In the case of $k_F > G/2$, the phase space available for the umklapp processes increases and, therefore, the probability of electron-electron umklapp scattering is enhanced.

Contributions from different scattering mechanisms dominate the resistivity of metal, depending on the measurement temperature. The Debye temperature for typical metals is around room temperature, and hence, the phonons have enough thermal energy for normal and umklapp processes at room temperature. The scattering cross-section for the defect contribution is, however, temperature-independent. The contribution of electron-electron scattering is usually negligible compared to the phononic one at high temperatures. Thus, with decreasing the temperature, either the T^5 or $e^{-T_U/T}$ dependence should dominate the resistivity. In a Fermi liquid, at low temperatures, $T << \Theta_D$, the population of phonons is negligible, hence, T^2 dominates the resistivity due to the electron-electron interactions. At sufficiently low temperatures, only the constant contribution from impurities is observed in resistivity as all the other scattering mechanisms are extinguished.

2.2 Electronic structure and Fermi surface of the non-magnetic delafossite metals

Shannon and co-authors grew a single crystal of $PdCoO_2$ and established the unusual valence character of $Pd^{1+}Co^{3+}O^{2-}$ [8]. Pd^{1+} is an unusual state that had never been observed in an oxide. In 1998 [22, 23] Tanaka *et al.* and Higuchi carried out photoemission spectroscopy (PES) studies on low-purity single crystals and determined a Pd domination of the states at the Fermi energy. In addition, they did specific heat measurements and proposed that the high conductivity of $PdCoO_2$ may come from Pd $4d$-$5s$ hybridisation as the coefficient of the T-linear term lay between the typical values for s and d electron materials. Similarly, Higuchi *et al.* proposed Pt $5d$-$6s$ hybridisation

for $PtCoO_2$ [24].

Trying to understand the origin of the quasi 2D behaviour of $PdCoO_2$ and $PtCoO_2$ the electronic structure of $PdCoO_2$ and $PtCoO_2$ was calculated by DFT in [25]. Eyert *et al.* confirmed that electrical conductivity in these materials is based on a Pd d-orbital derived Fermi surface. In $PdCoO_2$ and $PtCoO_2$, Co is in the low spin $3d^6$ state, meaning that CoO_2 layers are non--magnetic, in contrast to the CrO_2 layer in $PdCrO_2$, that I will discuss in Chapter 5. Eyert *et al.* regarded the CoO_2 insulating layer as a charge carrier reservoir and suggested this as a reason for the Pd-Pd interlayer coupling. They also established that the strong anisotropy of the electric conductivity is caused by the cylindrical Fermi surface that is shown in fig. 2.9. Therefore, the non-magnetic delafossite metals are natural heterostructures of high conductivity metallic layers and band insulators.

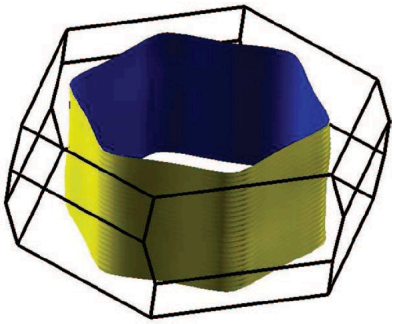

Figure 2.9: Fermi surface of $PdCoO_2$. Reproduced from [25].

One of the most direct ways to study the electronic structure of solids is angle-resolved photoemission spectroscopy (ARPES). Photoelectron spectroscopy is based on the application of the photoelectric effect observed by Hertz and explained by Einstein, who recognised that when light is incident on a sample, an electron can absorb a photon and escape from the material. We can obtain information on the energy and momentum of the electrons propagating inside a material by measuring the kinetic energy and angular distribution of the electrons photo-emitted from a sample illuminated with sufficiently high-energy radiation [26].

2.2 Electronic structure and Fermi surface of the non-magnetic delafossite metals

The first ARPES measurements by Noh *et al.* [27] confirmed the bulk electronic structure predicted by DFT. ARPES measurements of $PtCoO_2$ showed the similarity of the Fermi surface to that of $PdCoO_2$. The Fermi surface of $PtCoO_2$ has sharper corners and more rounded facets. Such studies in $PdCoO_2$ and $PtCoO_2$ have shown their bulk Fermi surfaces to be single band, half filled, and with a broadly hexagonal cross-section, as shown in fig. 2.10 [27, 28]

The ARPES studies also allow measurement of the dispersion of the conduction band, which enables the calculation of the Fermi velocity. Such measurement of the dispersion of the conduction band for $PtCoO_2$ is shown in figure 2.11. It is linear, sharp and steep in both cases. The Fermi velocities are huge, in the case of $PtCoO_2$ within 20% of the free-electron value [28]. Thus, we can conclude the nearly free electron nature of the conduction, which originates from the *s*-orbital contribution to the conduction band.

Another way to determine the Fermi surface of a material is by studying the de Haas van Alphen effect (dHvA), is a quantum mechanical effect in which the magnetic susceptibility of a metal oscillates as the magnetic field is increased. In an external magnetic field, the orbits of electrons in k space are quantised into so-called Landau levels. Because the quantisation happens in reciprocal space, the distance between these levels is proportional to $1/B$. Thus, the physical quantities, for example, magnetic susceptibility will oscillate in the external magnetic field with period proportional $1/B$. Knowing the angular and temperature dependence of these oscillations, we can reconstruct the Fermi surface of the metal [16]. The dHvA effect is far better than the ARPES at establishing the Fermi area because it is a bulk probe, and not subject to the surface charging effects that can affect ARPES.

The dHvA measurements by Hicks *et al.* for $PdCoO_2$ [29] and Arnold *et al.* for $PtCoO_2$ [30] confirmed the conclusions from ARPES. They observed in these two materials two high frequencies, corresponding to neck and belly orbits, alongside a beating frequency. These oscillations had a $1/cos(\theta)$ angular dependence (θ is the angle of the magnetic field to the z-axis), proving

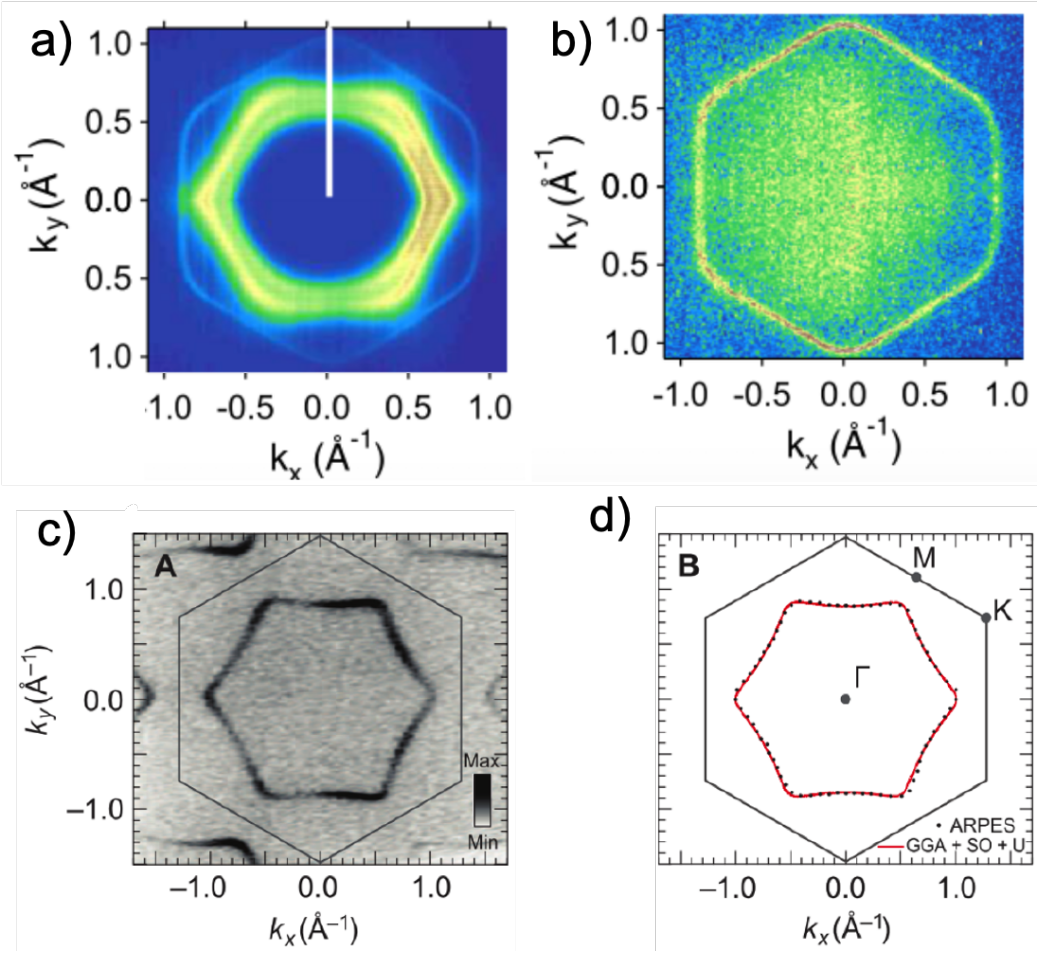

Figure 2.10: The first published angle resolved photoemission Fermi surface of $PdCoO_2$. a) The Fermi surface observed by Noh *et al.* via ARPES before and b) after thermal cycling to remove surface states. Reproduced from Ref. [27]. c) Fermi surface of $PtCoO_2$ measured by ARPES integrated. The solid line represents the Brillouin zone. d) The dots represent the Fermi momenta extracted from (c) by radially fitting momentum distribution curves (MDCs) around the measured Fermi surface. Reproduced from Ref. [28]

the cylindrical nature of the Fermi surface. The dHvA effect also allows calculating the effective mass by fitting so-called the Lifshitz-Kosevich formula by the temperature dependence of the oscillation amplitudes [16]. Thus, cyclotron masses for $PdCoO_2$ and $PtCoO_2$ from dHvA measurements [29, 30] are around 1.5 m_e and 1.05 m_e respectively, where m_e is the free electron

2.2 Electronic structure and Fermi surface of the non-magnetic delafossite metals

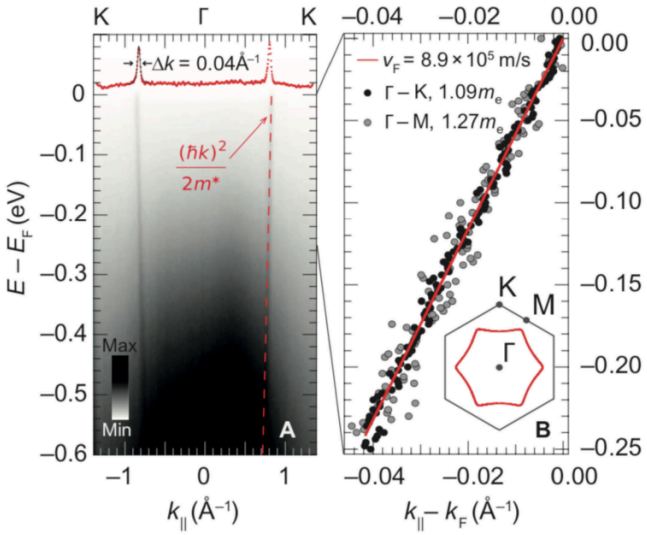

Figure 2.11: Left panel: The electronic structure of $PtCoO_2$ in the direction Γ-K as measured by ARPES. Right panel: Dots showing the peak position of fits to the momentum distribution curves along the Γ-K and Γ-M direction. Linear fitting to this data allows for the calculation of the Fermi velocity. Reproduced from Ref. [28].

mass. The $PtCoO_2$ value is in agreement, within experimental error, with the value from ARPES of 1.14 m_e for $PtCoO_2$ [28].

However, the small electron masses confirmed experimentally contradict the purely *d*-orbital picture of the conduction band shown by early DFT calculations in $PdCoO_2$. Pure d-bands are expected to have higher effective masses. Eyert *et al.* [25] focused on determining the dominance of Pd 4*d* or Pt 5*d* orbitals at the Fermi energy. This inconsistency proves the possible *s*-*d* hybridisation in these materials. The DFT calculations computed by Ong *et al.* [31] showed a small contribution from Pd 5*s* orbital located at adjunct sites in the *ab* plane at the Fermi level. The hybridisation of *d* and *s* electron physics leads to a highly faceted Fermi surface occupied by nearly free electrons, causing the novel transport behaviour in the ballistic regime that I will discuss in Chapter 4.

2.3 Transport properties of the non-magnetic delafossite metals

The measurements of resistivity in delafossite metals are challenging because of the tiny resistance of typical samples and because of the large anisotropy of resistivity between in-plane and c-axis transport. When the current has top-surface injection, it penetrates the full depth of the crystal only after an extended distance in the ab-plane due to anisotropy. The first published $PtCoO_2$ room temperature resistivity [7] was 3 $\mu\Omega cm$. In the latest research, Nandi *et al.* [32], used focused ion beam microstructuring techniques to ensure a homogeneous current profile, and reported a record for oxide of 1.8 $\mu\Omega cm$ room temperature resistivity. It indicates the significant impact of this effect on the measured properties and emphasises the importance of the careful fabrication method of the delafossite resistivity device.

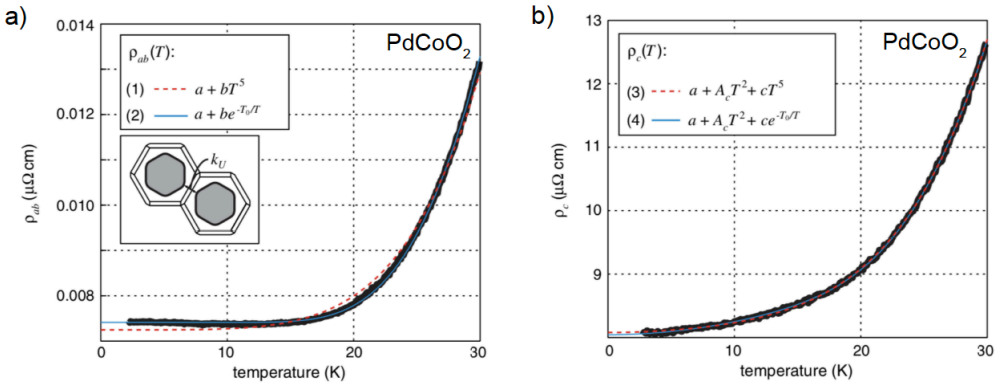

Figure 2.12: The $PdCoO_2$ temperature dependence of the resistivity a) ab plane b) c axis with fits. Reproduced from [29].

The first careful measurements of the temperature dependence of the $PdCoO_2$ resistivity in the ab plane and along the c-axis were done by Hicks *et al.* [29] (fig. 2.12). The different overall scale of the resistivity in fig. 2.12a and b proves the quasi 2D nature of the electron transport. The c-axis resistivity fig. 2.12b shows the features of the fermi-liquid behaviour with $a + A_cT^2 + cT^5$ temperature dependence, where a, A_c and c are constants.

However, the *ab* plane resistivity fig. 2.12*a* does not show the typical electron-phonon T^5 Bloch–Grüneisen behaviour and is well fitted with the activated function $a+be^{-T/T_0}$. Normal electron-phonon scattering relax momentum and dominates in resistivity. However, in some materials, for example, in alkali metals [33], the phonon population is pushed out of equilibrium by electron flow. In this situation, the electron-phonon collisions do not relax momentum but only transfer it between electrons and phonons. Thus, this scattering does not contribute to resistivity. This so-called phonon drag effect can be one possible explanation of the activated behaviour of $PdCoO_2$ [34, 35].

As I discussed above, momentum can be transferred to the lattice through umklapp processes. For in-plane conduction in $PdCoO_2$, the Fermi surface is closed, and there is an activation energy $k_B T_U = c\hbar k_U$, where c is the speed of sound in $PdCoO_2$ and k_U is the minimum wave number for umklapp processes (illustrated in fig. 2.12*a*). In $PdCoO_2$ $k_U = 0.5$ Å. This leads to the observed activation temperature of 165 K [29, 34]. Below this temperature, umklapp scattering is suppressed, electron-phonon scattering transfers momentum between electrons and phonons but does not relax it, and the temperature dependence of the resistivity is exponential.

There is a slight in-plane resistivity upturn at temperatures below 10 K fig. 2.12*a*. It varies between crystals and is more extended in $PtCoO_2$. This effect does not weaken in an external magnetic field and also there is no sign of magnetic impurities that might contribute to a Kondo effect [34]. Therefore it is unlikely the Kondo effect [31] and has an undetermined origin.

The resistivity-derived mean free paths of $PdCoO_2$ and $PtCoO_2$ at low temperatures are around 20 μm and 5 μm respectively, and therefore are extremely large for metals. However, these values are different from the Dingle mean free path 0.6 μm and 0.3 μm, determined from the dHvA experiment [29, 30]. This discrepancy suggests that small-angle scattering, which reduces the Dingle mean free path but does not contribute significantly to resistivity, is more frequent than large-angle scattering. Additionally, the hexagonal

Fermi surface limits the impact of small-angle scattering on electron transport [30]. If the scattering happens between states on the same facet of the hexagon, it does not significantly affect the resistivity as the electron trajectory is not changed. But the small-angle scattering would still broaden the Landau levels and therefore decay the quantum oscillations. I will discuss the influence of the high symmetry Fermi surface on transport in delafossite metals later in Chapter 4.

In Ref. [36] we studied the origin of such a long mean free path. A key question is whether these extremely low resistivities result from strongly suppressed backscattering due to special features of the electronic structure or are a consequence of highly unusual levels of crystalline perfection. The results of the irradiation experiment confirmed the second scenario. The as-grown crystals have an extremely low number of in-plane defects of approximately 0.001%. These results demonstrate that crystalline perfection is the crucial factor in achieving the long mean free paths and emphasises how unusual these delafossite metals are compared to the vast majority of other oxides and alloys. However, the irradiation experiments answer only 'how' questions. Thus, it is still not understood 'why' as-grown delafossite metals are so pure.

Chapter 3

Sample preparation

Delafossite crystals $PtCoO_2$, $PdCoO_2$ and $PdCrO_2$ usually grow in a hexagonal platelet shape with thickness typically about $1 - 6$ μm for $PtCoO_2$ and $5 - 15$ μm for $PdCoO_2$ and $PdCrO_2$. The size of the crystals in the *ab*-plane usually varies from 100 μm to 500 μm in all compounds. An example of a $PdCoO_2$ crystal is shown in fig. 3.1.

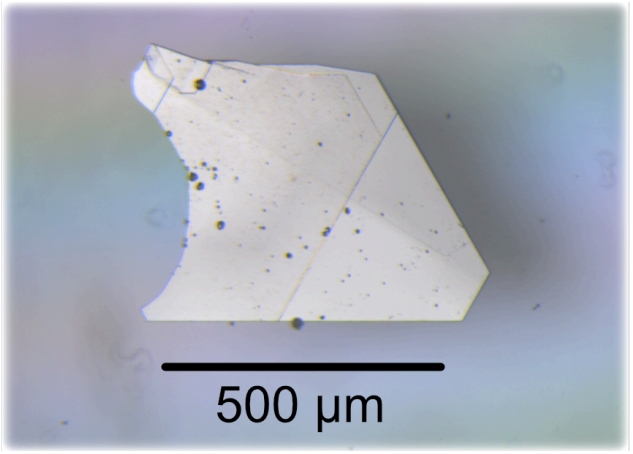

Figure 3.1: Example of a $PtCoO_2$ crystal

As mentioned above, the mean free path in delafossite materials can be as long as 20 μm, which is very large in comparison with other metals. This property is one of the reasons why the delafossites are subject to widespread study. But to study transport properties of these materials, the dimensions

of the device (for example in the ballistic regime) should be the same length scale or even smaller than mean free path of the electrons. In standard methods of mounting crystals 'by hand', one could reach sizes around 100 – 150 μm. That is still not enough, even in delafossites, to study different transport regimes. For that reason Focused Ion Beam (FIB) micromachining, that will be discussed next, has become an extremely useful tool in precise transport studies of delafossite materials.

FIB has been a vital tool for my thesis research. Therefore, I will start with a basic introduction to the FIB and its fundamental working principles in this chapter, followed by different techniques of creating a final device from an as-grown crystal that we developed. I will close the chapter by describing the range of measurement techniques that were employed to explore the delafossite metals in my projects.

3.1 FIB

The FIB has existed since the mid-1970s. The initial uses were primarily for the semiconductor industry [37], for cutting transmission electron microscopy (TEM) samples [38] and for imaging in the biological sciences [39]. However, it has begun to be used to structure modern quantum materials into bespoke devices only in recent years.

FIB is an excellent micro-sculptor to fabricate devices suitable for exploring the mesoscopic regimes as it offers both high-resolution imaging and flexible micro-sculpting of the samples in a single tool.

3.1.1 Basic design

In my studies, I used a dual FIB/SEM (scanning electron microscope) platform (a schematic is shown in fig. 3.2) from a company manufacturing such instruments, FEI. An SEM is typically used for high-resolution electron beam imaging, and FIB is used for micro-structuring. The e-beam column is placed vertically in the middle of the sample chamber, and the FIB column is set at

52°. Both beams can be simultaneously focused at the same point. Therefore, the same part of a sample can be milled with the FIB while a high-resolution image is taken simultaneously with the SEM.

The design of a FIB column is similar to an SEM one. The key features of a FIB are a source of ions and an evacuated column with electrodes to accelerate the ions. A schematic of the FIB column is shown in fig. 3.2. A set of apertures defines the ion beam current, electrostatic lenses focus the beam, and octupole plates are used for beam scanning.

The sample is placed on a 5-axis moveable stage in an evacuated chamber. To prevent interaction between the ions and other particles, both the column and the chamber are evacuated to low pressure, around 10^{-8} and 10^{-6} Torr, respectively.

The ion column should provide a controlled ion beam with the smallest possible focal spot for a given current. It can be achieved with electrostatic, rather than magnetic, lenses due to the high ion mass. The apertures primarily determine the beam current. Depending on the ion source, possible current values are from around 1 pA to 1 μA and a typical acceleration voltage of about 30 kV.

Most FIB systems use a liquid metal ion source (LMIS) [40, 41]. In this source, metal is held in a reservoir above a sharp tungsten tip. The metal is melted by a heater, which wets the tip. A very high voltage of several thousand volts is applied between the tip anode and an apertured cathode, namely the extractor. At a voltage greater than a threshold, the liquid metal film at the tip becomes distorted, resulting in the formation of a Taylor cone at the tip due to the combined effect of the electrostatic forces, surface tension, and droplet pressure. As the voltage increases, field ionisation causes an emission of ions, with the typical acceleration voltage of 5 - 30 keV.

Using Gallium as a source has several benefits. It has a low melting temperature, around 30 °C, a high ion mass, low volatility, low vapour pressure, and it is not reactive with the tungsten tip, so it has a long lifetime. How-

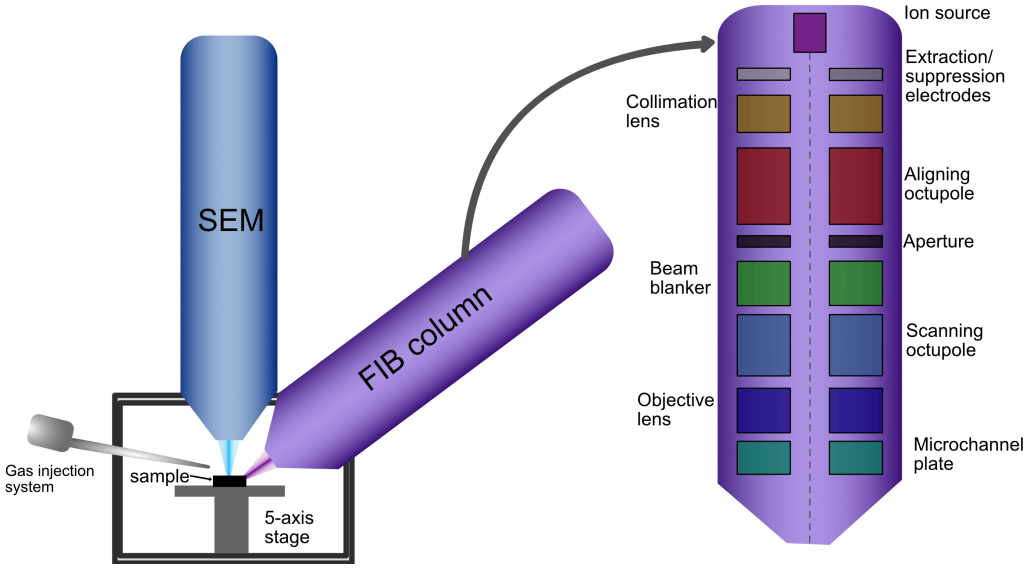

Figure 3.2: A schematic of a typical dual beam FIB-SEM system.

ever, limitations of an LMIS are most significant with the increase of the beam current as the energy spread is affected by Coulomb forces. Above the current value of around 5 nA, the beam diameter increases rapidly due to spherical aberration [42]. This makes the use of the LMIS impractical at currents above around 50 nA.

The inductively coupled plasma source (ICPS) [42] can be used to go to a higher beam current. In this source, a gas, often xenon, is used instead of metal. This gas is inductively coupled to a coil which forms a radio frequency antenna. A current driven through this coil ionises some atoms and creates a plasma. A set of electrodes then accelerate the ions and emit them from the source.

At small currents, the diameter of the beam from an ICPS is larger than that from the LMIS, however, above the current value of around 30 nA, it is smaller. At the highest practical current of 2 μA, the beam's spot size is of order 1 μm. Due to the much higher currents that are achievable, our Xe plasma FIB has a cutting rate typically 100 times higher than that of our Ga LIMS FIB. Processes that do the 'rough cut' with the plasma FIB and

finer work with the Ga FIB are also possible.

Several detectors are typically installed for use with both the SEM and FIB. Two detectors are implemented for electron imaging, a through-lens detector (TLD) and an electron multiplier. The TLD is mounted vertically above the sample in the objective lens of the electron column. This detector detects electrons ejected of a direct collision between the e-beam and the sample atom generated through direct interaction with the sample, and imaging is done at a very short working distance. Therefore TLD provides a very high resolution and achieves excellent surface information.

The Everhart-Thornley detector (ETD) is mounted on one side at a 45 degree angle. It is essentially a photomultiplier tube. A collector grid and screen, basically a Faraday cage, are mounted on one side of the sample stage where a scintillator is placed. Strong contrast and shadow are essential features of the ETD.

Ion imaging is also possible in a FIB. However, users should be careful with it as it damages a sample with ions. The yield of SI generation is entirely independent of beam energy and depends rather strongly on the surface composition of the material. The secondary ions, ionised atoms sputtered from the sample surface due to interaction with the beam, are used for this imaging.

3.1.2 Milling of the sample

Particles generated due to inelastic processes are used as probes for imaging, while elastic collisions are the primary tool in milling the sample. The collision cascade triggers momentum transfer from the ion beam to the sample, resulting in atoms being knocked off the sample surface.

Grounding of the sample is an important step in the milling process. Otherwise, Ga^+ ions accumulated on the sample surface repulse the ion beam, defocusing it around the pattern. The pattern ends up having indistinct features. Therefore, insulators can be quite tricky to cut in a FIB. One way to minimise charging artefacts is to coat an insulating sample with a layer of

conducting material.

To mill a sample with a FIB, the machine software is used to create a pattern which defines the area which the beam should scan over. The critical parameters for the milling are the beam current and the total depth of the cut. With the set parameters, the total time is automatically calculated based on known sputter rates for materials such as silicon. Then the beam passes multiple times over each part of the pattern until the desired depth is achieved. There are also two options for the several milling patterns. With serial milling, one pattern trench is milled at a time. Parallel milling makes a single pass of ion beam over each trench. The total time for patterning is dependent primarily on the ion beam current. Choosing larger currents for cutting can significantly reduce the time of the milling, however, it also increases the spot size of the beam, thereby decreasing the pattern resolution.

Some of the sputtered material is often deposited back onto the sample's surface during the milling process. The amount and form of redeposition vary depending on the geometry, chosen current and milling material. The critical aspect ratio for the milling of the sample is the width of the trench to its depth. If the width of the pattern is much smaller than its depth, the milling of the sample is not possible. To increase the visibility of the crystal sidewalls, which is vital for thickness measurements, the optimal ratio of the depth of the trench to its width should be below one. Parallel milling is preferable if pattern features overlap to prevent redeposited material into a previously milled trench.

Redeposition of the material is a general challenge for FIB milling. However, the redeposited material has a high resistance in most cases due to its amorphous nature. Redeposition of the ultra-pure metallic delafossites becomes problematic as it remains highly conductive and can easily cause significant electrical shorts, which cause issues in the form of pathways for electrical conduction.

A vital step to remove the redeposition and prevent the small electric shorts is sidewall polishing. The schematic of this process is shown in fig.

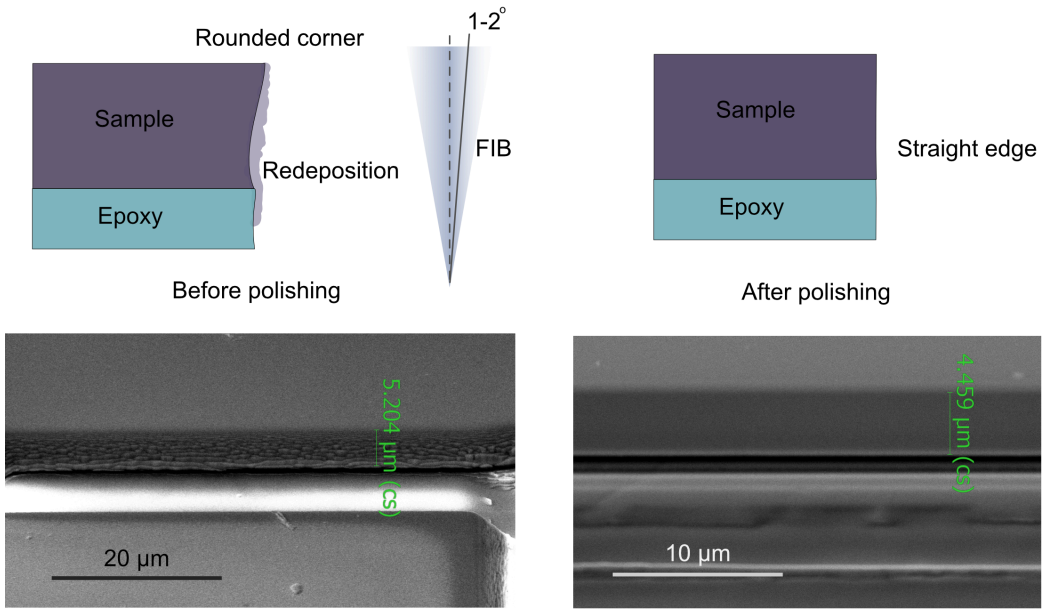

Figure 3.3: A schematic of the FIB polishing process. Before polishing, the sidewall is not straight and there is a substantial layer of redeposition. After polishing with the beam at a glancing angle, the redeposition layer has been removed and the side of the sample is straight. The lower panels show SEM images of the sidewall of the device before and after polishing.

3.3. Normally the FIB beam is rotated to a glancing angle of $1 - 2°$ to the side of the sample. Typically for the polishing, the beam current is chosen to be lower than that for the milling. The beam is then swept in several linear passes, reaching the set depth in each pass to the final intended sidewall position. The SEM image of the example of the sample before and after polishing is shown in fig. 3.3. This process also ensures that the side walls are vertical, which is important for accurate resistivity measurements.

The FIB can damage the sample quite substantially in the process of milling. The damage layer is primarily formed when the collision cascades overlap, creating a sustainable layer on top. The ion-solid interaction can be simulated by a program called SRIM (Stopping Range of Ions in Matter), with input parameters: ion energy, weight and incident angle and the sample depth and material. Using this simulation, it is possible to predict the in-

duced damage of the material from the ions. In the delafossites the damage layer is tens of nm, so insignificant in devices with minimum dimension of order 1 μm.

3.1.3 Deposition of materials using FIB

The FIB can also be used to deposit materials in a process known as ion-assisted chemical vapour deposition (IA-CVD) [43]. The main limitation of this process is the availability of the required precursor gases. For example, in our instruments at the present time, it is possible to deposit only Pt, W, SiO_2, and C for which the precursor gases are readily available.

In the IA-CVD process shown in fig. 3.4, a retractable needle is placed in the vicinity of the area of interest to provide a local flow of the desired organometallic gas. This gas adsorbs onto the surfaces, and the ion beam scans over the desired deposition area. The ion current, acceleration voltage and precursor should be carefully chosen, because, imbalance in either can provoke inefficient deposition or milling away sample material in the worst case. The process of IA-CVD removes only the highly volatile organic materials, leaving the desired material deposited on the surface.

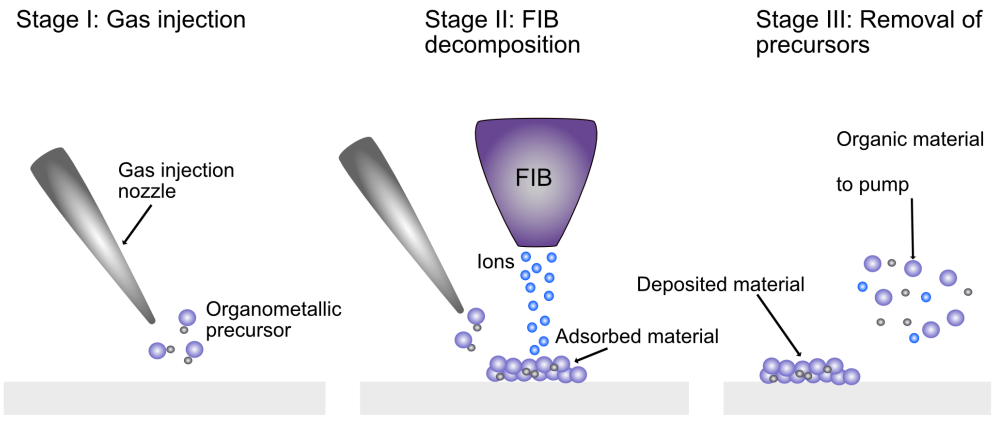

Figure 3.4: A schematic of the IA-CVD process

Unfortunately, FIB deposited metals are far from pure. The composition

of the deposition is an amorphous mix of different materials. Studies in Ref. [44] showed that FIB deposited Pt was around 73% C, 10% Ga and only 17% Pt. Thus the resistivity of the deposited materials is a factor of 50 larger than that of pure Pt, and W [45]. Application of a high voltage in-situ to cause annealing can improve the resistivity of deposited W. However, no method to lower resistivity of deposited Pt was reported so far. Therefore, in the absence of techniques for high conductivity materials, I used the deposited material only as a platform for clean metal, for example, gold, to be sputtered on top of it.

3.2 'Classical' sample mounting

Producing a delafossite metal device for resistivity measurements brings several challenges even at the first steps. Before starting fabricating a device out of delafossite metal, we should consider the homogeneity of current distribution throughout the sample thickness in highly anisotropic materials using top-injection current contacts. For the accurate resistivity measurements in *ab* plane, the current should flow perpendicular to the *c*-axis and should penetrate the whole depth of the sample. However, if the current path in the device is too small for homogenisation through the whole sample depth to occur, the conduction will only happen at the top of the crystal, producing a higher resistance. A straightforward solution to this problem is to extend the current path before the voltage contacts are reached. This can be achieved via a meander, a long snake-shaped path that we sculpt using the FIB in both current contacts.

In addition, the handling of delafossite metal crystals requires meticulous care. The crystals are incredibly fragile. Therefore, movement via tweezers is not possible in work with these crystals. Another safe alternative method is to use electrostatic forces. The MiTiGen polymer MicroTools or tips made from PTFE tape on the end of a toothpick can be used as a tool.

The schematic steps to create a final device from the delafossite crystals

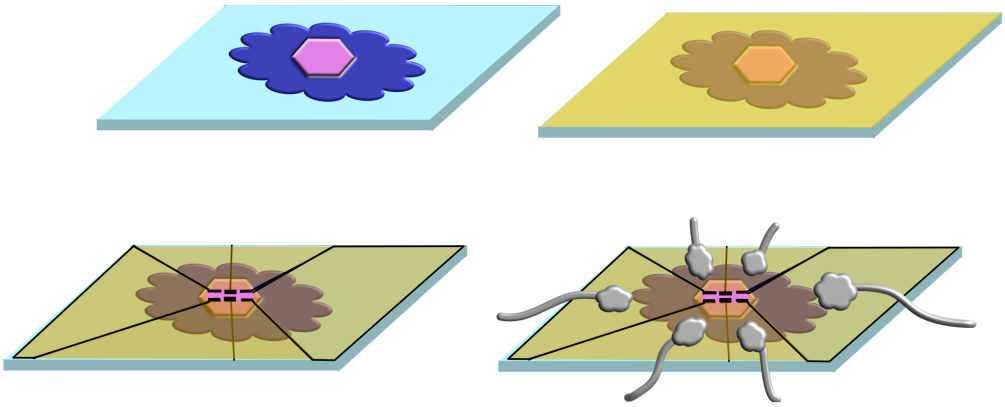

Figure 3.5: Schematic four main steps of structuring a device

are shown in fig. 3.5. As-grown crystals are mounted on a drop of two-component glue on a pre-cleaned sapphire substrate. Crystals are mounted in the glue by hand with help from kapton micro-tools. Then, 200 nm of gold with a 5 nm sticking Ti layer is sputtered on the substrate with the crystal. The 2-component glue creates very smooth contacts to the delafossite crystal. After sputtering gold, the crystal is structured into the required shape and the contact configuration is established by selectively removing the gold, with both steps performed using either the Ga-FIB or the Xe-FIB. Using the Ga-FIB, feature sizes of 200 nm are achievable. After structuring the crystals and cutting the gold pads, silver wires are glued to the gold contacts using silver epoxy and the whole substrate is stuck onto a chip carrier.

With the help of the FIB, it is possible to go to very small dimensions (in comparison with the mean free path of the electrons) of the devices. Also, the accuracy of electronic transport experiments is increased by precisely defining the geometry of the device in FIB, and measuring its dimensions with an accuracy of several tens of nm.

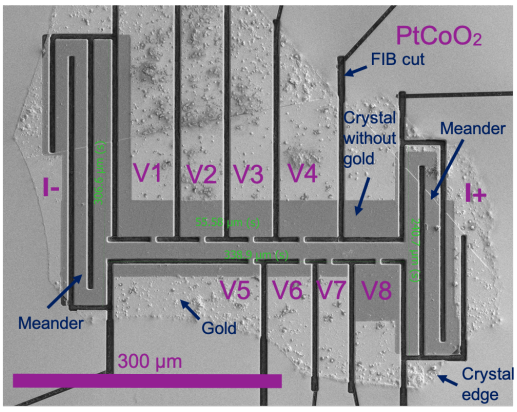

Figure 3.6: SEM image of the final device device

3.3 Epoxy-free method

For certain experiments (for example electron irradiation, that I will discuss below) the above method of mounting samples is not suitable because of the presence of the epoxy. For that reason, we developed an epoxy-free method of mounting samples. This method is based mainly on the FIB Pt deposition tool.

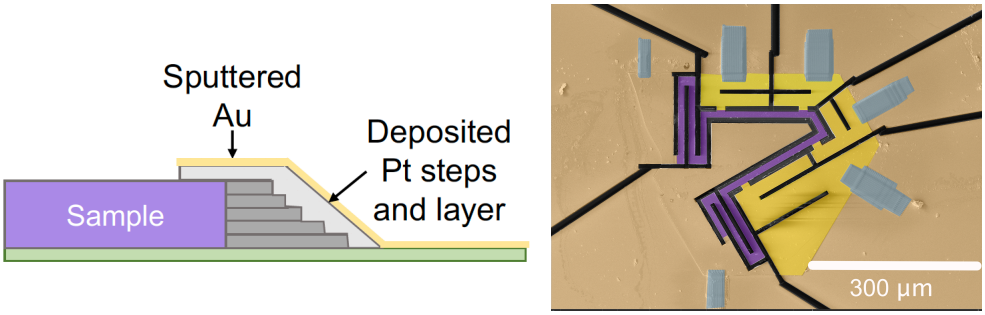

Figure 3.7: Left: Scheme of the epoxy-free method of mounting samples, right: SEM image of the sample mounted in epoxy-free way. Pt contacts are coloured in blue. Purple is the 'effective part' of the device, yellow - voltage contacts with meanders (part of the crystal).

As it is shown in fig. 3.7 left, the first step is to place the crystal on a thin layer of acetone or isopropanol on a pre-cleaned substrate. The solvent will evaporate and create static forces which will hold the crystal on a substrate

without movement during the next steps. The substrate with the crystal on it is covered by a 200 nm layer of sputtered gold with a 5 nm sticking Ti layer. Then, several Pt layers are deposited in a FIB creating the 'step' on the edge of the sample. Deposited Pt 'steps' create not only electrical but also mechanical contact. This geometry can help to increase the stiffness of the Pt contact, stick the edge of the sample to the substrate and keep it in place. FIB-deposited Pt does not have very good conductivity, so to decrease contact resistance a second sputtered layer of gold is required. After this, the sample can be structured in the FIB. An example of the sample mounted in this way is shown in fig. 3.7 right panel. Pt contacts are coloured in blue, the device is coloured in purple, the voltage contacts with meanders are yellow. Here, meanders of the voltage contacts are structured only for mechanical purposes. Current contact meanders (also shown in purple in the figure) are made for current homogeneity.

Usually, substrates are made of insulating material, for example, sapphire. Because the crystal is stuck to a substrate that has low thermal expansion or contraction, stiff Pt contacts create mechanical stresses in the sample during cool down. Making meanders in all contacts of the crystal is an effective way to decrease such stresses.

3.4 Measurement of low resistivity materials

Because of the high conductivity of delafossite metals, resistivity measurements are quite challenging. The first difficulty that comes with these resistivity measurements is the common-mode voltage. A common-mode signal is a voltage common to both input terminals of an electrical device. These issues occur when the sample resistance is small compared to the resistance of the contacts and wires.

Typically in such resistivity measurements, ac currents are created by using the shunt resistor and ac voltage supplied by a lock-in amplifier (fig. 3.8a). In this case, the common-mode voltage (V_{CM}) will begin to affect

lock-in amplifier measurements of the voltage difference.

Usually, a low-temperature resistance for the delafossite sample is $R_S \sim 10\ \mu\Omega$, and the contact resistance is $R_c \sim 5\ \Omega$. Thus, in this configuration (fig. 3.8a) with a measurement current of 5 mA the common-mode voltage is $V_{CM} = \frac{V_1+V_2}{2} \sim 25$ mV. The sample voltage difference is $\Delta V \sim 50$ nV, $5{*}10^5$ times smaller than the common-mode voltage.

Most lock-in amplifiers, for example, the Stanford Instruments SR830, can reject common-mode voltage up to around 100 dB, which means the common-mode rejection ratio should be below 10^5. However, above this ratio, the common-mode signal starts to influence the measured voltage. For the delafossite sample, the contribution is a $25{*}10^{-3}/10^5 \sim 250$ nV signal before amplification, much bigger than the experimental signal.

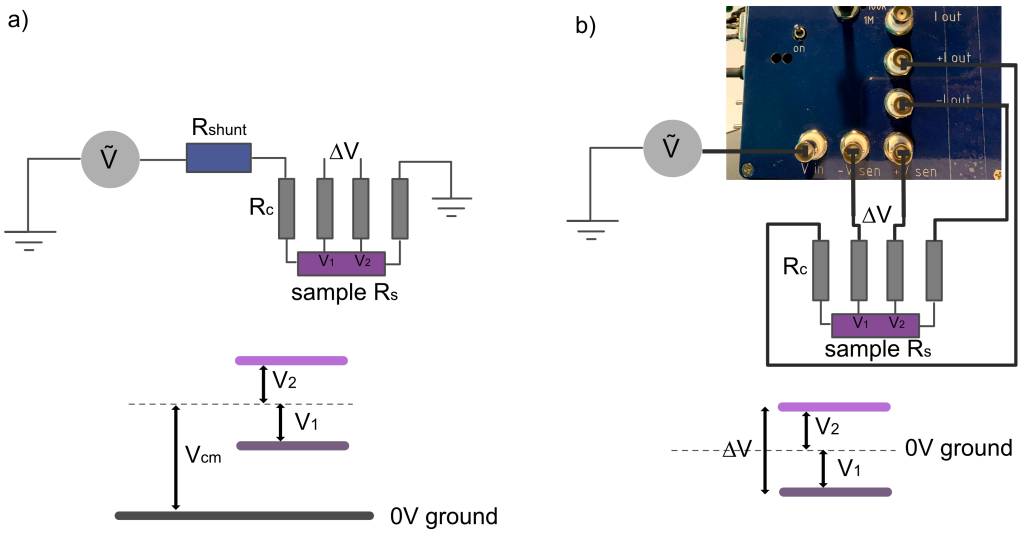

Figure 3.8: Resistivity measurement schematics for a) the standard method of producing a current for an ac measurement, with a shunt resistor. There is a large common-mode voltage. b) A measurement with the CMR source. The common-mode contribution to the signal has been eliminated.

To solve this problem, a bespoke dual-sided current source was designed by Mark Barber, and Alexander Steppke [46]. This current source with common-mode rejection (CMR source), as shown in fig. 3.8b sources current from both sides of the sample with an opposite sign, ensuring that the ground

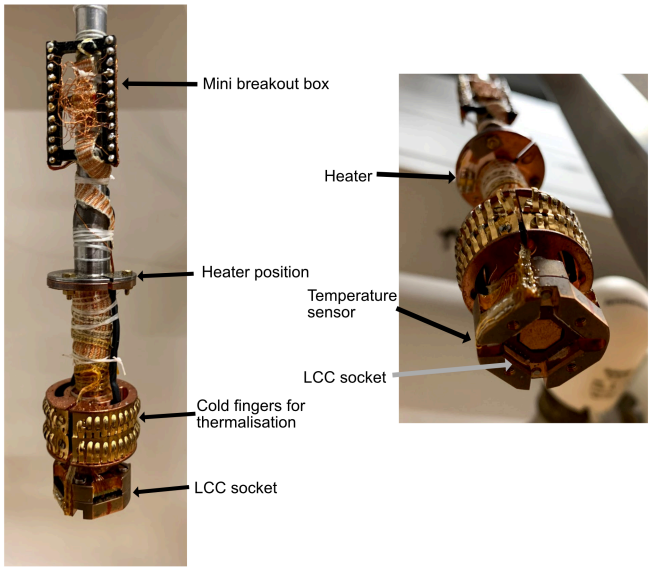

Figure 3.9: Images of the lowest part of the custom PPMS insert the LCC socket at the end of the insert.

is effectively in the middle of the sample. This CMR source has an active feedback mechanism to sense offset voltage at the sample. It, therefore, senses the voltage at the sample via the voltage contacts (Vsen in fig. 3.8b) and adjusts the current input accordingly to ensure the ground is precisely at the midpoint of the two voltage contacts. In this measurement, $V_1 = -V_2$ and the common-mode voltage is near zero.

For the low-temperature measurements, I used a Quantum Design Physical Property Measurement System (PPMS) with 9 T or 14 T magnets that provide measurement capability down to at least 1.8 K within a magnetic field. The advantage of using PPMS instead of another type of cryostat is the ability for rapid sample changes. However, the in-built resistivity measurement system does not provide the required noise level limiting the signal size to 20 nV and allows only five simultaneous voltage measurements. Therefore, I used a bespoke PPMS insert, previously designed and constructed by Nabhanila Nandi [47]. The insert, shown in fig. 3.9, has 12 twisted pairs of measurement wires leading to a small breakout box in the lower section. The mini-breakout box allows reconfiguration of the wiring between

the twisted pairs and the pins on the chip carrier, offering flexibility in voltage wiring. The sample is usually mounted on 28-pin leadless Kyocera chip carriers (LCCs), which are inserted into the LCC socket at the bottom of the PPMS insert. The same chip carriers are used in the high energy electron irradiation, will be discussed in section 3.5, which facilitates the device characterisation before and after the irradiation beamtime.

Thermometry, provided by a Cernox temperature sensor, placed close to the sample, ensures the careful reading of the sample temperature. An additional heater of the sample is also available for PID control of the temperature.

I used a Synktek MCL1-540 lock-in amplifier for the voltage measurements. This amplifier is capable of measuring up to 10 voltage channels simultaneously. The noise level is around 1.8 nV/$\sqrt{Hz}$.

3.5 High energy electron irradiation

In previous sections, I discussed the importance and influence of defects on transport properties. Often, scientists want to achieve the best quality of the samples, i.e. make them as pure as possible. I hope to show that defects can become a powerful tool in studying the physical properties of materials. But for systematic studies, it is crucial to know the type and number of defects in a material. It is even better if one can introduce a certain type of defects into the material.

Irradiation by high-energy electrons (1 - 10 MeV) is the ideal technique to introduce point-like defects in a controlled way. Electrons of these energies can transmit enough energy to an atom to displace it from the lattice site. But these energies are not enough for the substituted atom to create a significant number of additional defects. Therefore individual Frenkel pairs are created. For my purposes, other types of irradiation are not suitable. For example, in ion irradiation, the incoming particles' larger mass turns every collision into a collision cascade, making larger columnar defects.

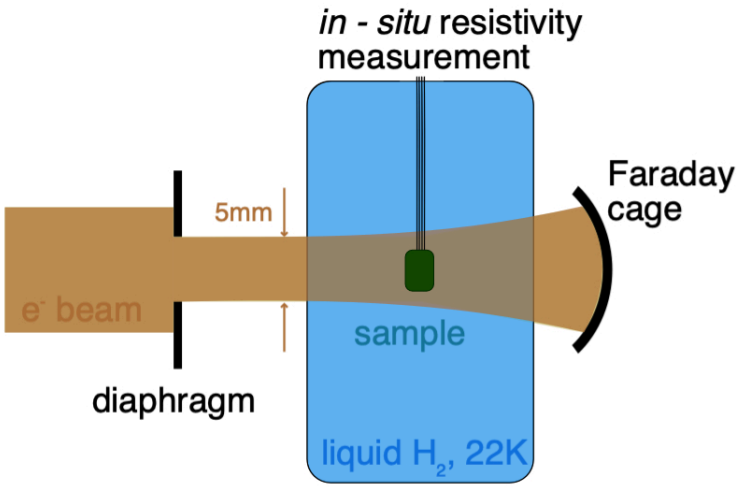

Figure 3.10: A sketch of electron irradiation experiment. The yellow area indicates the range in which the electron beam is swept, rather than representing the beam cross-section

I performed the irradiation experiment with electrons with a kinetic energy of 2.5MeV at the SIRIUS Pelletron linear accelerator operated by the Laboratoire des Solides Irradi´es (LSI) at the Ecole Polytechnique in Palaiseau, France. A sketch of the experimental set-up is shown in fig. 3.10. During the irradiation, to ensure that the introduced defects are not mobile, the sample was placed in a bath of liquid hydrogen at a temperature of approximately 22 K. The accelerator beam passed a current of 1.5 - 2.5 μm through a circular diaphragm with an aperture of 5 mm diameter before reaching the sample. The current passing through the diaphragm was experimentally determined using a calibration metallic sample. The beam was swept horizontally and vertically at two incommensurate frequencies, ensuring the homogeneous irradiation of the sample. During the calibration procedure, a thin metallic test sample is placed in the cryostat, with the accelerator current at a set value. The accumulated charge on this sample is recorded and the irradiation current calculated. Then this process is repeated for another value of accelerator current. Thus, the current on a calibration sample, I_S, is known

as a function of the accelerator current, I_A. To calculate the total irradiation dose, the charge accumulated at the Faraday cage, Q_{FC}, is divided by the average of the current incident on the Faraday cage, I_{FC}. With all these parameters known, it is possible to calculate the final dose D in units of C/cm^2:

$$D = \frac{1}{0.2}\frac{Q_{FC}}{I_{FC}} I_A \frac{\Delta I_S}{\Delta I_A}, \tag{3.1}$$

where, $\Delta I_S/\Delta I_A$ is the gradient of the calibration sample, and 0.2 cm^2 is the cross-sectional area of the beam.

The penetration range of electrons with energies of 2.5 MeV is estimated to be $\sim$ 1.8 mm in the investigated delafossite metals. Such an extended penetration depth guarantees homogeneous irradiation through the sample thickness, which is typically two or three orders of magnitude shorter than the estimated penetration range of electrons. These two facts further ensure that the majority of electrons could be measured using a Faraday cage behind the sample stage. It also allows monitoring the current fluctuations during a measurement. The unique set-up at the Laboratoire des Solides Irradi´es (LSI) additionally provides an opportunity to perform in-situ four-point resistivity measurement. Thus we could monitor the change of the resistivity during irradiation as a function of electron dose. The irradiation is paused at regular intervals, to perform the in-situ resistance measurement. Measuring resistivity of crystals as conductive and as small as delafossites in those demanding conditions presents additional challenges. We addressed these challenges by developing the dedicated sample preparation method, described above in Section 3.3.

3.6 Conclusions

This chapter described the key aspects of applying focused ion beam microstructuring, low noise resistance measurement techniques, and external facility techniques to transport studies of delafossite metal samples. The

3.6 Conclusions

FIB is a highly flexible tool that enables the rapid creation of bespoke structures. The design of the microstructures could be chosen to either enhance the resistance, therefore improve the signal to noise ratio, or provide the unconventional transport regime in the material, which I will illustrate in Chapter 4 to examine the ballistic regime in delafossite metals. In addition, the ability of the FIB to deposit certain materials is vital to the epoxy-free methods of sample mounting, which will be used in Section 4.4 for electron irradiation studies.

The high energy electron irradiation facility becomes a unique technique to study delafossite metals. Previously, this experiment helped us to understand the origin of extremely high conductivity [36]. However, in Section 4.4 I will show the new application of the high energy electron irradiation experiment.

Chapter 4

Ballistic transport in $PtCoO_2$

In section 2.1 I discussed the scattering processes that affect the resistivity in ordinary metals. However, this typical textbook picture changes when the mean free path (l_{MR}) of the electron (the average distance between collisions that relax the electron momentum) becomes significant compared to the dimensions of the device, such that the boundary scattering starts to measurably influence the electron transport. Delafossite metals, as described in Chapter 2, are a unique model system for the investigation of unconventional transport regimes in an ultrapure material with a non-circular Fermi surface and quasi-2D electrical transport. In this chapter, I will discuss the essential aspects of this regime in the delafossite metals. The experiment that I performed in square junctions of $PtCoO_2$ studying the ballistic regime in delafossite metals shows the advantages of studying the ballistic regime in a novel model system and gives a new example in which high energy electron irradiation helps to uncover intrinsic physics.

4.1 Unconventional transport regimes

The majority of metals have much lower purity than the delafossite metals. This increases the number of momentum-relaxing collisions with defects and ensures that the mean free path of electrons is much smaller than the typical

device size. In this Ohmic (sometimes also referred to as 'diffusive') regime the scattering in the bulk crystal rather than the boundary scattering affects the resistivity (fig. 4.1). However, if the mean free path of sample becomes larger than its width, then the device is in a ballistic regime. The behaviour becomes nonlocal, therefore, it is impossible to define the direct relationship between current density and electric field, i.e. the Ohmic relations for resistivity are no longer valid.

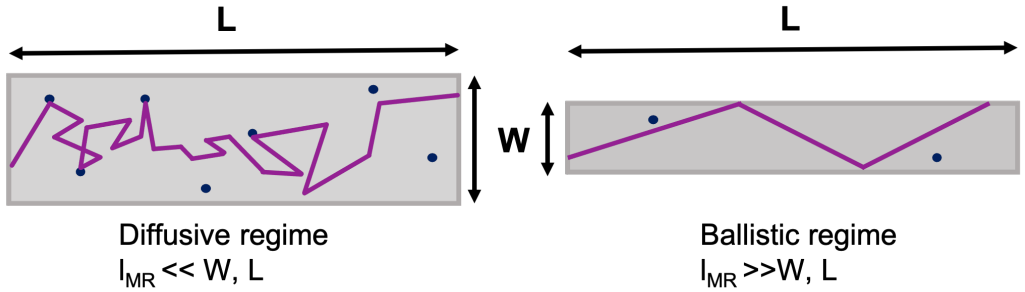

Figure 4.1: Diagrams of diffusive (Ohmic) and ballistic regime transport in a channel

In the ballistic regime, the size of the Fermi wavelength ($\lambda_F = 2\pi/k_F$) also becomes vital as it determines if the boundary scattering is specular or diffusive and is also relevant to the conditions required to achieve a quantum point contact. When the boundary roughness s is smaller than the Fermi wavelength λ_F, then the scattering is specular, and the momentum parallel to the boundary is conserved. The parameter p describes the fraction of specular scattering, with $p = 1$ corresponding to fully specular scattering. In the opposite case, the scattering is diffusive, the direction after scattering is randomised, and p=0.

The restricted geometrical length scales also allow coherent quantum mechanical effects to occur if the phase breaking length l_ϕ is longer than the device's geometry. This length l_ϕ is mainly limited by the inelastic processes of electron-phonon or electron-electron scattering.

The early studies of the ballistic regime were primarily performed in ultra-pure metals. The simplest theoretical model by Nordheim [48] applies

Matthiessen's rule for the combination of the resistivity in a wide channel ρ_{bulk} and an extra resistivity coming from the boundary scattering ρ_{bound}:

$$\frac{\rho}{\rho_{bulk}} = \frac{\rho_{bulk} + \rho_{bound}}{\rho_{bulk}} = 1 + \frac{1}{w}, \tag{4.1}$$

where ρ is a total resistivity and w is the width of the channel. This model assumes only fully diffusive boundary scattering, with p=0. Within the early theoretical studies, the boundary scattering conditions were a challenge. A later theoretical model by Fuchs [49] was more sophisticated and based on the Boltzmann equation, also including the possibility of non-diffuse boundary scattering. However, the exact method of preparation of the ballistic device influenced the agreement with theoretical calculations due to the poor control of the boundary roughness. Even within the same material, the wide range of possible values for the specularity of the boundary scattering impairs the accuracy of comparison experiments and theory. Another significant challenge in a more general understanding of transport behaviour in ultrapure materials also became the electronic structure and 3D Fermi surface of these metals.

The emergence of semiconductor heterostructures allowed the fabrication of a much more comprehensive range of devices. The high mobility 2DEGs and new microstructuring techniques allowed more careful control over the device geometry and the specularity of the boundary scattering than was possible with elemental materials. Electrostatic gating also allows for varying the boundary scattering specularity. Thus, the resistivity in a GaAs-based heterostructure was enhanced over the value for a wide channel [48, 49]. Because specular boundary scattering does not change the resistivity, it is possible to observe such an effect only if the boundaries are partly diffusive.

The Nordheim equation (4.1) could be adjusted by application of Matthiessen's rule but also considering the possibility of specular scattering p. Thus, the resistivity at zero magnetic field in a narrow channel can be determined in terms of the value in an infinitely wide channel, ρ_{bulk} as [50]:

$$\rho = \rho_{bulk}[\frac{1}{l_{MR}} + \frac{1-p}{w}] \tag{4.2}$$

It is important to note here that boundaries in FIB structures can be regarded as diffusive, as FIB sculpting can damage the sample quite substantially in the process of milling and introduces many point defects in this damage layer because of the implanted ions. The damage level for each material is different and can be calculated as discussed in Section 3.1.2.

As shown in fig. 4.2 the magnetoresistance in narrow semiconductor channels is initially positive in a transverse magnetic field. In a zero magnetic field, electrons have trajectories mainly parallel to the channel axis. As we turn on the magnetic field, the trajectory of the electrons diverts toward the boundaries increasing the resistivity. It reaches the maximum at $w/r_C \sim 0.55$ in GaAs-based heterostructures, where w is the width of the channel and r_C is cyclotron radius. In graphene, this value is around 0.9 [51]. With a further increase of the magnetic field, the cyclotron radius decreases, reducing the frequency of contact of the electrons with boundaries and, therefore, the resistivity decreases. When $w/r_C > 2$, the electrons cyclotron orbits become tiny, therefore the resistivity becomes equal to the bulk value.

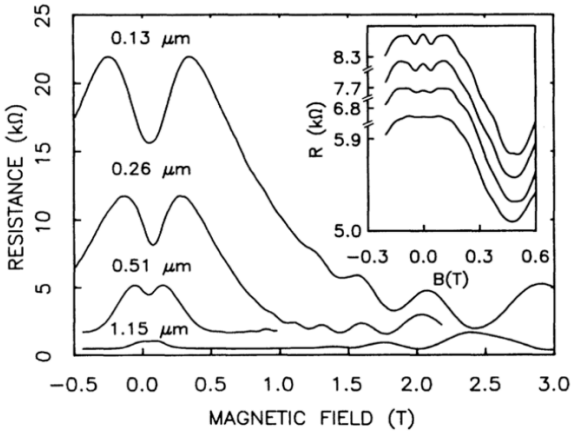

Figure 4.2: The magnetoresistance at 4 K of 12 μm long 2DEG GaAs-AlGaAs wires with width as indicated, reproduced from [49]. Inset: low magnetic field data for a wire defined electrostatically at four gate voltages.

It is vital to note that the models described above assumed a spherical (circular in 2D) Fermi surface and that any scattering was isotropic, with an equal relaxation time around the Fermi surface.

4.2 Directional ballistic effects

The original motivation for the project I have undertaken so far was to study the ballistic transport regime in delafossites to improve understanding of the hydrodynamic flow regime. But the results that we obtained have revealed interesting and unique properties of delafossite metals.

Reaching the ballistic regime, with $w < l_{MR}$, is challenging on two fronts. Firstly the material has to be pure enough to have a long mean free path. The second challenge is microfabrication techniques. They should define devices on length scales, which, even in the purest materials, are typically below 50 μm. Thus, the combination of the delafossites' extremely purity and the FIB technologies discussed in chapter 3.2 gives the unique opportunity to study the ballistic regime in these materials.

4.2.1 Anisotropic or isotropic?

The low-temperature resistivity behaviour in an initial set of measurements in a narrow channel did not agree with the Ohmic regime prediction. The resistivity data reported in Ref. [52] showed deviation from the prediction of a standard Boltzmann theory for circular Fermi surface including boundary scattering but neglecting momentum-conserving collisions.

In a typical metal majority of collisions (impurity, normal electron-phonon, Umklapp electron-electron, and Umklapp electron-phonon) relax momentum, taking the electrons far from the hydrodynamic limit. Moll *et al.* performed accurate resistivity studies varying the $PdCoO_2$ channel width to investigate if the electronic viscosity plays a role in determining electrical resistance. $PdCoO_2$ has several remarkable and unique properties that make it a candidate for searching for the hydrodynamic regime. Firstly the

electrical conductivity of $PdCoO_2$ is remarkably low. At room temperature, it has a resistivity of just 2.6 $\mu\Omega$cm, 30% lower per carrier than that of elemental copper. The resistivity below 15 K is essentially independent of temperature and reaches a value of several nΩcm. Secondly, there is evidence of the existence of phonon drag, in which the phonons follow the electrons into an out-of-equilibrium distribution [29]. The shear viscosity effects take over in resistivity due to momentum conserving scattering, such as electron--electron scattering. However, in special circumstances like the phonon drag, the electron-phonon scattering becomes momentum conserving. The unusual behaviour of $PdCoO_2$ was explained by including a the hydrodynamic correction to the ballistic Boltzmann theory for the circular Fermi surface.

However, the transverse focusing experiment in $PdCoO_2$ [53] showed strong directional behaviour, that contradicts the viscous theory and is assumed to have ballistic origin.

In the ballistic regime, the electrons injected from a nozzle do not scatter in bulk and follow trajectories determined by the field along the rectangular boundaries (fig. 4.3). When the cyclotron diameter is equal to the distance between two contacts, most electrons are focused into the second contact and give a peak in the voltage measurement. If we increase the magnetic field, further geometric resonances occur at integer multiples of the original focusing field, resulting in a series of peaks in the voltage [54].

Bachmann *et al.* [53] observed several focusing peaks over scales of up to tens of microns in $PdCoO_2$ device length, verifying the existence of an extremely long mean free path [55]. Intriguingly, the form of the focusing peaks depended on the orientation of the Fermi surface relative to the device. Usually, the symmetry of the unit cell constrains the properties of the material in an ideal crystal. However, within the Ohmic regime, for delafossite metals, with a triangular underlying lattice, in each Pd or Pt plane, the in-plane electrical transport is expected to be isotropic even though this is perhaps not obvious at first sight.

For a triangular lattice, such as shown in figure 4.4, there are a number

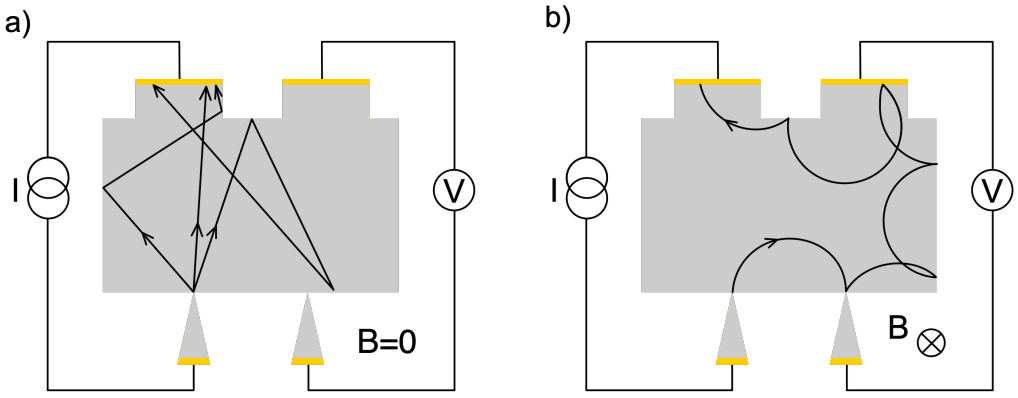

Figure 4.3: Sketch of the focusing device a) electron trajectories with zero magnetic field and b) in a magnetic field

of symmetries expected in the conductivity matrix: symmetry in reflection about two perpendicular in-plane axes and also rotations of modulus 60° about the z-axis.

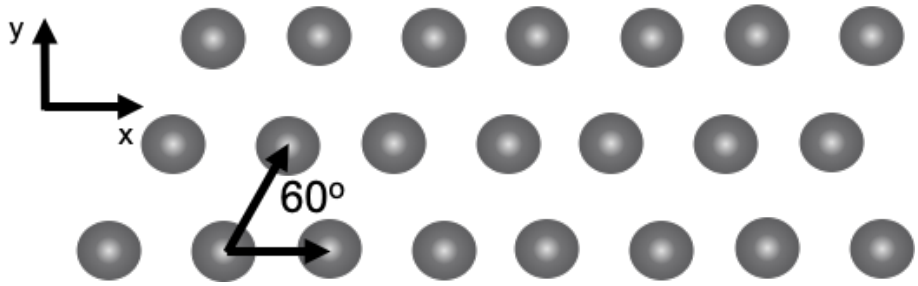

Figure 4.4: Schematic of a triangular lattice.

For the in-plane resistivity, I will neglect the z-dimension. Thus, in 2D, the generic conductivity matrix, σ, can be written as:

$$\sigma = \begin{pmatrix} \sigma_{xx} & \sigma_{xy} \\ \sigma_{yx} & \sigma_{yy} \end{pmatrix} \tag{4.3}$$

where σ_{ij} are the components of the conductivity tensor.

Reflection of the conductivity matrix about the x-axis can be obtained by

a reflection matrix, A,

$$\sigma = A\sigma A^T = \begin{pmatrix} 1 & 0 \\ 0 & -1 \end{pmatrix} \begin{pmatrix} \sigma_{xx} & \sigma_{xy} \\ \sigma_{yx} & \sigma_{yy} \end{pmatrix} \begin{pmatrix} 1 & 0 \\ 0 & -1 \end{pmatrix} = \begin{pmatrix} \sigma_{xx} & -\sigma_{xy} \\ -\sigma_{yx} & \sigma_{yy} \end{pmatrix} \quad (4.4)$$

so from symmetry $\sigma_{xy} = \sigma_{yx} = 0$.

A rotation matrix, R, for 60 degrees will give the following result:

$$\sigma = R\sigma R^T = \begin{pmatrix} cos60^\circ & -sin60^\circ \\ sin60^\circ & cos60^\circ \end{pmatrix} \begin{pmatrix} \sigma_{xx} & 0 \\ 0 & \sigma_{yy} \end{pmatrix} \begin{pmatrix} cos60^\circ & sin60^\circ \\ -sin60^\circ & cos60^\circ \end{pmatrix} \quad (4.5)$$

$$= \begin{pmatrix} \frac{1}{4}\sigma_{xx} + \frac{3}{4}\sigma_{yy} & \frac{\sqrt{3}}{4}(\sigma_{xx} - \sigma_{yy}) \\ \frac{\sqrt{3}}{4}(\sigma_{xx} - \sigma_{yy}) & \frac{3}{4}\sigma_{xx} + \frac{1}{4}\sigma_{yy} \end{pmatrix} \quad (4.6)$$

which leads to σ_{xx}=σ_{yy}.

Thus, there is no in-plane conductivity anisotropy expected in a material with a triangular lattice in the Ohmic regime. However, the results in Ref. [53] do not obey this conclusion of in-plane isotropy.

The resistivity anisotropy is often used as a probe of the broken symmetry. One of the drivers of spontaneously broken symmetry can be so-called electron nematicity. It is a unidirectional self-organised state that breaks the rotational symmetry of the underlying lattice. The electrons enter the nematic state as a phase transition, as the temperature drops below some critical value. Like some forms of unconventional superconductivity, nematicity can be ascribed to strong and anisotropic electron correlations [56, 57]. Is this low-temperature anisotropy in *ab* plane resistivity evidence of the unexpected exotic physics in $PdCoO_2$ and $PtCoO_2$ that was not observed before?

4.2.2 Directional ballistic effects in channels

During her PhD studies Maja Bachmann did a directional ballistic study on $PdCoO_2$ [55]. I decided to do it on $PtCoO_2$ both to check that the basic

picture is consistent with that of $PdCoO_2$ and also to assess whether small differences in Fermi surface shape makes a difference. Thus, I created a microstructure of $PtCoO_2$ with four channels which is shown in fig. 4.6. The hexagonal Fermi surface is the key feature that differentiates $PtCoO_2$ and $PdCoO_2$ from the ballistic structures of 2DEG. In the case of the circular Fermi surface electrons are injected in all directions (fig. 4.5). However, if the metal has a hexagonal Fermi surface, there are only six preferable directions for the electrons. Thus, I made the four microstructure channels aligned at different angles according to the Fermi surface. When the bar is aligned at 0°, electrons have two preferable directions; at 30°, there are three directions for electrons, 10° and 20° are intermediate states. The width of all the four channels of this microstructure is around 3.6 μm, which is smaller than the typical mean free path of $PtCoO_2$. The length of the channels is between 150 and 160 μm.

At high temperatures, when the mean free path is relatively small, the resistivity value of each channel is identical (fig. 4.7A) as the triangular lattice has an isotropic conduction tensor in the diffusive regime. However, within the ballistic regime, at low temperatures, we can observe the induced resistivity anisotropy. The magnitude of the low-temperature resistivity depends upon the orientation of the channels. The minimum resistivity occurs in the channel oriented at 30°. When the Fermi surface is rotated, the resistivity values increase and reach their maximum at 0° rotation.

The magnetoresistance shown in fig. 4.7B is normalised by the high field resistivity values and plotted against the ratio of the width of the sample to the cyclotron radius ($w/r_C \sim$ B). The magnetoresistance behaviour has the same qualitative structure as seen in the experiments in semiconductor heterostructures and graphene discussed above. However, the peak shape at a finite field depends on the orientation as the magnetic field forces trajectories parallel to the axis towards the boundary. When the cyclotron diameter matches the width of the channel ($w/r_C \sim 2$), the electron orbits become small, therefore, there is no distinction between orientations.

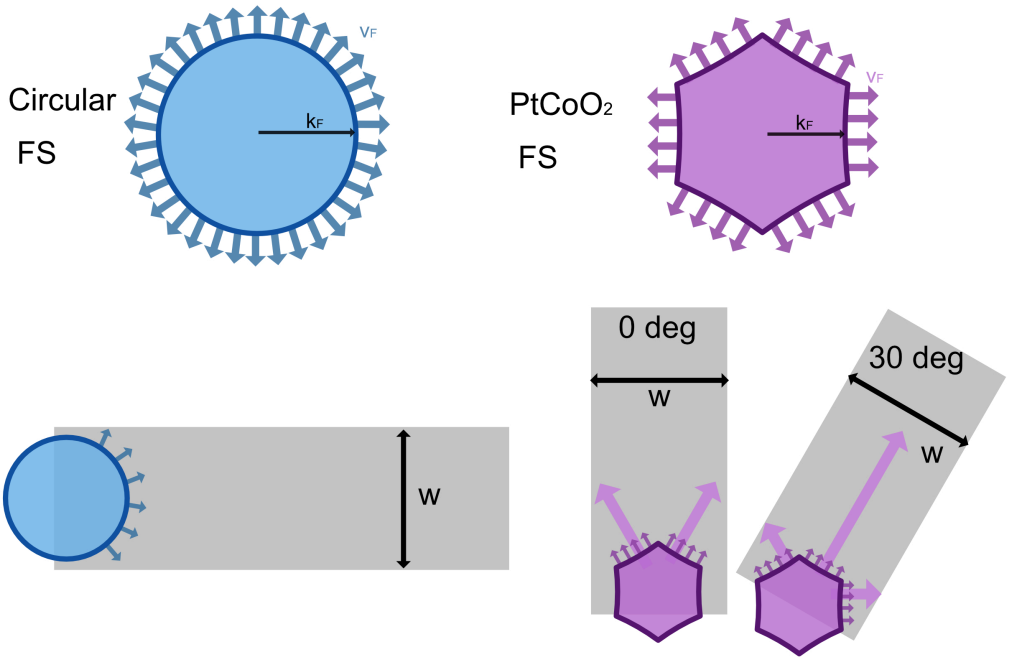

Figure 4.5: A schematic showing the range of the typical directions of the Fermi velocity for both a circular Fermi surface and the $PtCoO_2$ Fermi surface.

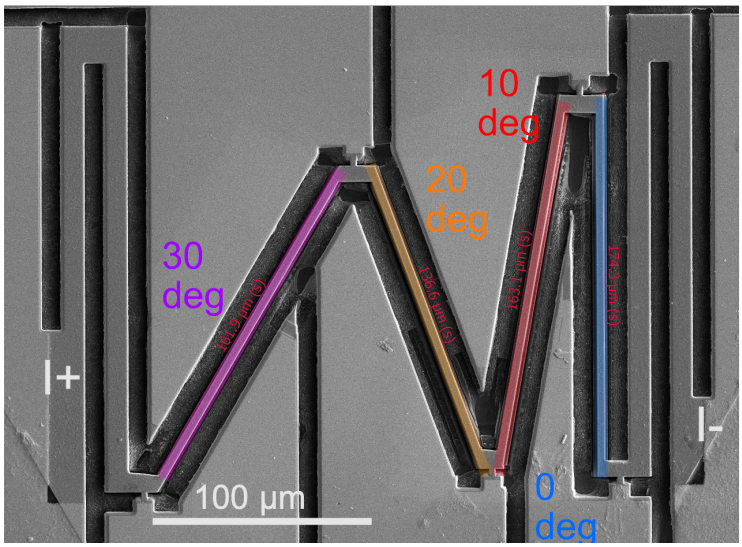

Figure 4.6: SEM image of the $PtCoO_2$ device with four channels

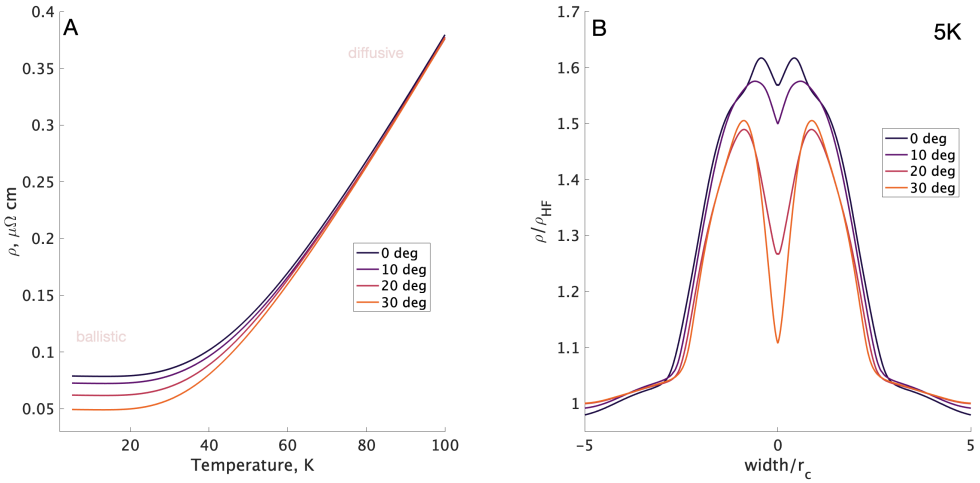

Figure 4.7: A: Temperature dependence of the resistivity of $PtCoO_2$ sample with four channels with width around 3.6 μm each rotated according to the Fermi surface orientation respectively. B: magnetoresistance at 5 K for these four channels normalised by high magnetic field values.

The experimental results suggest, that the above conclusion of in-plane isotropy does not remain the same in the ballistic regime. The intrusion of boundaries at distances equal to or less than the mean free path eliminates the translation symmetry and assumption of an infinite crystal implicitly required in the above derivation. Therefore, anisotropies in the electrical transport in the narrow $PdCoO_2$ channels become possible and are dependent upon the Fermi surface orientation and dimensions of the device rather than breaking the bulk symmetries of the underlying lattice.

4.2.3 From ballistic to diffusive

The critical parameter in the ballistic regime is the ratio of the device's dimensions to the mean free path of the electrons. Technically it is not easy to vary the dimensions of the device. Certainly, FIB broadens these boundaries. However, going accurately from diffusive to ballistic regime step by step using the FIB (i.e. decreasing the device's dimensions) can be challenging. This approach also adds more experimental uncertainties as the geometry of the

sample is changing.

The high electron irradiation experiment becomes a unique tool in studying ballistic regime in delafossite metals. Introducing point-like defects in a controlled way allows going backwards from the ballistic to the diffusive regime by decreasing the momentum-relaxing mean free path with the same geometry of the device and the same contact configuration.

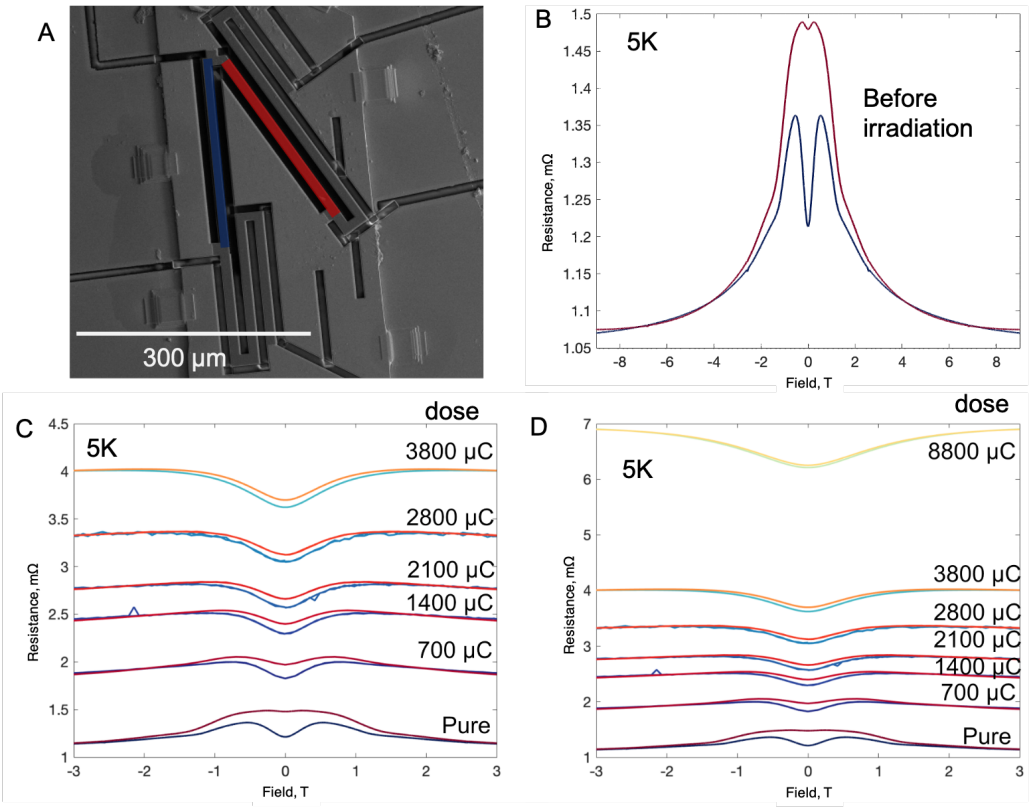

Figure 4.8: A: SEM image of the $PtCoO_2$ device with two channels aligned according to the Fermi surface orientation: red is 'hard' blue is 'easy'. B: magnetoresistance of the two channels before irradiation (red is 'hard' direction, blue is 'easy' direction), C: magnetoresistance of two channels after different doses of irradiation up to 3800 μC and D up to 8800 μC

To study the ballistic-diffusive cross-over, I made the microstructure of $PtCoO_2$ shown in fig. 4.8A. It is similar to that shown in fig. 4.6 but with only two extreme alignments of channels according to the Fermi surface. In

this device, 0° is the 'hard' direction and coloured red in the figure and 30° is the 'easy' direction and coloured blue. I used the epoxy-free method described in section 3.3 to create this microstructure. The magnetoresistance of these two channels, shown in fig. 4.8B at 5 K in the pure sample (before irradiation) exhibits similar behaviour to that shown in fig. 4.7.

However, as I start affecting the device by high electron irradiation (fig. 4.8C), the difference between two extreme orientations of Fermi surface in magnetoresistance at small fields becomes smaller every single irradiation step, eventually, at the dose of 8800 μC in units of charge (fig. 4.8D), the difference between these two channels disappears, and resistivity becomes isotropic as expected in a diffusive regime. Thus, we also estimated an approximate dose of electron irradiation for almost eliminating ballistic effect in $PtCoO_2$, which is important for the experiment that I will discuss below.

This work shows that in clean metals, the symmetry lowering by the sample shape itself can induce such an anisotropic response. The irradiation experiment proves that the induced anisotropy in resistivity is a consequence of the lowering symmetry by the device's geometry and symmetry of the Fermi surface.

4.3 Geometry of the square devices

Because boundary scattering determines electron transport, in the ballistic regime, the geometry of the devices becomes a key feature in these studies. Thus, as well as the narrow channels, other experimental geometries were widely measured in other ultrapure materials and confirmed to be a specially sensitive probe of the ballistic regime. These were four-terminal junctions, where the size of the junction is approximately equal to or smaller than the mean free path. Inspired by the novel phenomena observed in the narrow channels of $PtCoO_2$ and $PdCoO_2$, we proposed investigating whether these novel phenomena could be observed in square-shaped four-terminal junctions. Another question that we were interested in these studies was the influence

of the six-fold symmetry of the Fermi surface on ballistic effects. In this section, I will describe the basic features and transport behaviour of these junctions.

4.3.1 Van der Pauw method

The four-terminal junctions are typically either cross or square-shaped, as shown in fig. 4.9. In these configurations it is possible to perform two types of resistance measurement. The first one is the bend resistance $R_{12,34}$=V_3-V_4/I_{12}, where the voltage difference is measured between contacts 3 and 4 with current flow from contact 1 to contact 2. Such measurements are so named as the current must flow around a bend in the cross junction geometry, but the terminology has also been extended to squares. This configuration has a partner resistivity measurement $R_{23,14}$ where the voltage is measured between contacts 2 and 3 and current flows from contact 1 to 4, respectively (fig. 4.9 left panel). The second measurement configurations are Hall resistance measurements, such as the $R_{42,13}$ configuration, where voltage is measured between contacts 4 and 2 and current flows from contact 1 to 3 and the partner $R_{13,42}$. Both are shown in the right panel of figure 4.9.

In the Ohmic regime, where the mean free path is much smaller than the device size and the conductivity is isotropic, a device with an arbitrary shape can be used to determine the resistivity tensor using the Van der Pauw method [58]. With this method, multiple components of the resistivity tensor can be measured using a single set of contacts. The Van der Pauw method, therefore, allows performing the resistivity measurement of the material with a lamella device independent of its shape and geometry: only the thickness of the sample requires accurate measurement.

However, the most straightforward geometry for this kind of study is a square-shaped device with a small contact size. In the diffusive (Ohmic) regime, a series of resistance measurements $R_{ab,cd}$ are made with different configurations. Van der Pauw showed [58] that the measured resistances and the resistivity ρ obey the Van der Pauw equation:

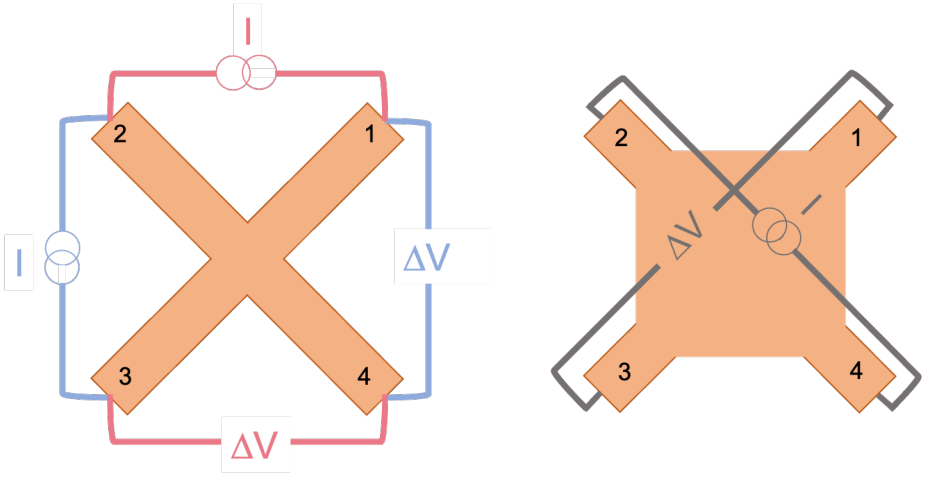

Figure 4.9: Left panel: A cross junction with two bend resistance measurement configurations. Right panel: A square junction with a Hall resistance measurement configuration.

$$e^{-\frac{\pi t R_{12,43}}{\rho}} + e^{-\frac{\pi t R_{23,14}}{\rho}} = 1 \tag{4.7}$$

where t is the sample thickness.

In the specific case of isotropic transport, when $R_{12,43} = R_{23,14} = R$, Equation (4.7) reduces to:

$$\rho = \frac{\pi t}{ln2} R. \tag{4.8}$$

In the ohmic regime and when a device has a square geometry, this resistivity is always positive and independent of the square's size. The magnetoresistance shows the typical behaviour of the properties of the material.

The Montgomery method is used for resistivity measurements for materials with anisotropic conductivities, such as those with orthorhombic lattices [59].

4.3.2 Early studies

When the mean free path becomes larger than the characteristic dimensions of a square or cross junction, the devices enter the ballistic regime. The behaviour of the Hall and Bend voltages becomes dramatically different to that in the Ohmic regime. This regime was first achieved in the 1980s in semiconductor 2DEGs at cryogenic temperatures but has since been extended to various materials.

Some of the initial studies were measurements of bend voltage $R_{12,43}$ and $R_{23,14}$, as shown in the left panel of fig. 4.9. Timp *et al.* carried the first bend voltage measurements within the mesoscopic regime in a GaAs-AlGaAs heterostructure [60]. Similar studies were performed in other ultrapure materials: InSb [61], HgTe [62] and graphene [63].

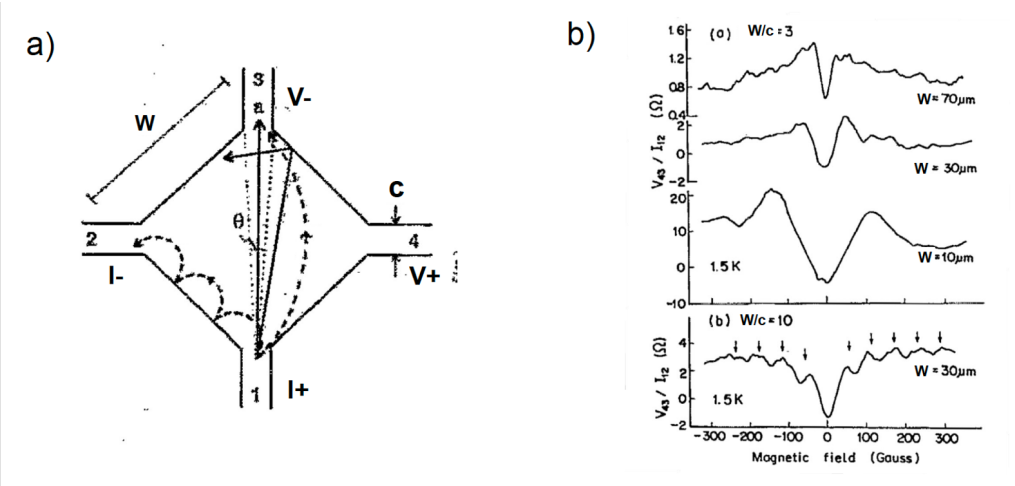

Figure 4.10: a) Schematic of a square shaped device with side length W and contact width c, adapted from [64]. b) b Bend voltage in magnetic field at 1.5 K for different values of W and c for a 2DEG in an AlGaAs-GaAs heterostructure, adapted from [64].

The bend voltage was qualitatively similar in both square and cross junctions and all the materials. However, the bend resistance behaviour notably deviates from the Ohmic one. In the case of a GaAs-AlGaAs square of side length W and contact size c (sketched in figure 4.10a), the measured volt-

age at zero field is negative (figure 4.10b). At a medium magnetic field, the magnetoresistance rises to a size-dependent peak and returns to zero at a high magnetic field [64]. However, a positive zero-field voltage and negligible magnetoresistance in the Ohmic regime would be expected for this material. The estimated mean free path, derived from the mobility, was 69 μm. An unusual trend was also observed. With the decrease of the device size, the magnitude of the negative peak increases and the peaks occur at a higher magnetic field.

Several quantum mechanical origins were proposed to explain this effect. However, it was eventually confirmed to be semiclassical. At zero field, the electrons emitted from the negative current contact pass predominantly along the square diagonal to the positive voltage terminal instead of the positive current contact, making the measured voltage negative. In the magnetic field, when the square side length becomes an integer multiple of the cyclotron diameter, a large number of the electron trajectories are focussed into the next contact. This picture is similar to the transverse electron focusing geometry discussed above. It leads to a series of voltage peaks at multiples of the focusing field $B_F = 2\hbar k_F/eW$, where W is the width of the square. Above this field, the cyclotron radius becomes smaller, and electrons travel along the side of the square to a contact adjacent to the injection contact, regardless of the magnetic field. Therefore, the voltage is nearly independent of the magnetic field.

In this ballistic regime in square devices with circular Fermi surfaces, the difference between the two bend resistance measurements is possible only due to fabrication induced geometrical asymmetries. All measurements reported within the literature showed the characteristic signals of ballistic transport in four-terminal junctions: a dip and a negative voltage at zero magnetic field and an increase in the voltage at higher fields.

4.3.3 Square junctions of $PtCoO_2$

The previous studies of the ballistic regime in the four-terminal junctions have mostly been within materials with circular Fermi surfaces. However, the effect of lower symmetry Fermi surfaces is unknown. The previous studies in the long channels of $PtCoO_2$ and $PdCoO_2$, discussed in section 4.2, imply that the hexagonal Fermi surface of these materials may have a significant impact on the ballistic transport and perhaps lead to novel phenomena.

Therefore, inspired by the Montgomery method, we developed a similar approach to establish the influence of the hexagonal Fermi surface of $PtCoO_2$ on the electrical transport in the ballistic regime and study in more details the nature of the anisotropy effect in transport, discussed in section 4.2. Creating the micron-scale square devices was possible by the development of the FIB techniques for ultrapure materials described in section 3.2. The critical parameter in the ballistic regime is the ratio of the momentum-relaxing mean free path to the width of the square. The high energy electron irradiation, discussed in section 3.5, also allows us to perform a unique experiment. By introducing point-like defects in a controlled way, we can change the momentum-relaxing mean free path of the electron without changing contact configuration, the device's geometry, and initial sample quality, which dramatically decreases experimental uncertainties.

To facilitate the study in delafossite metals, I fabricated a series of square $PtCoO_2$ junctions with a side length, W, typically about 15 μm and contact size c of around 5 μm. Figure 4.11 shows an electron image of the 15 μm $PtCoO_2$ square device prepared using an epoxy-free method of mounting, discussed in section 3.3. All four contacts of the square have meanders for current homogeneity. As irradiation experiments can decrease the mean free path, the square device should initially show a strong ballistic behaviour. In our previous studies [65, 66], the square device with the 15 μm side length showed strong ballistic behaviour, despite that this being larger than the typical mean free path of $PtCoO_2$ of approximately 4 μm.

Unlike with the circular Fermi surface shown in figure 4.12, we should also

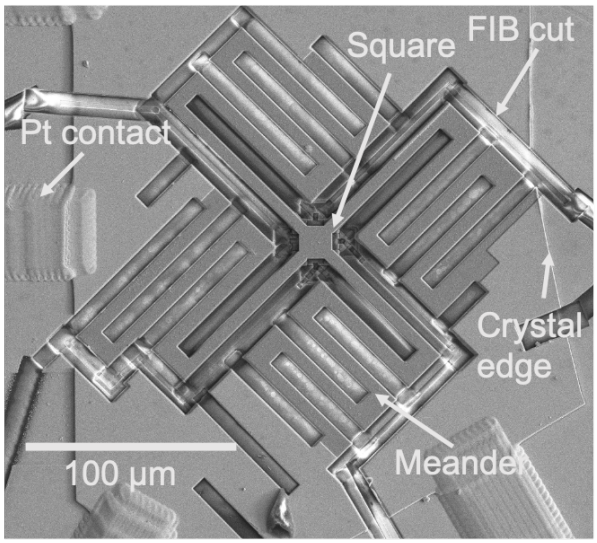

Figure 4.11: An SEM image of a $PtCoO_2$ square microstructure mounted by epoxy-free method.

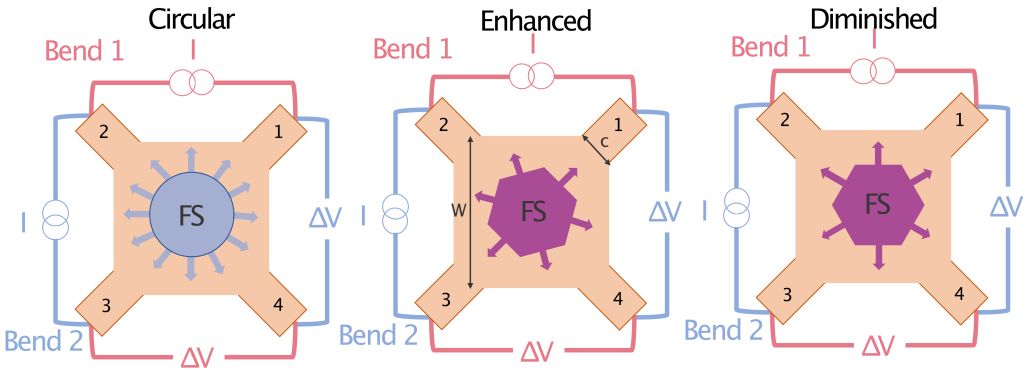

Figure 4.12: A schematic of the Fermi surface orientation relative to the square geometry for a circular Fermi surface and the enhanced and diminished orientations in $PtCoO_2$.

consider the orientation of the hexagonal $PtCoO_2$ Fermi surface relative to the square. For these studies, we used two different Fermi surface orientations shown in fig. 4.12. The orientation of the Fermi surface was chosen to vary the ease of transmission along the diagonal: the enhanced orientation should increase this transmission and the diminished one should decrease it. Figure 4.12 demonstrates that the enhanced orientation has one of the six primary

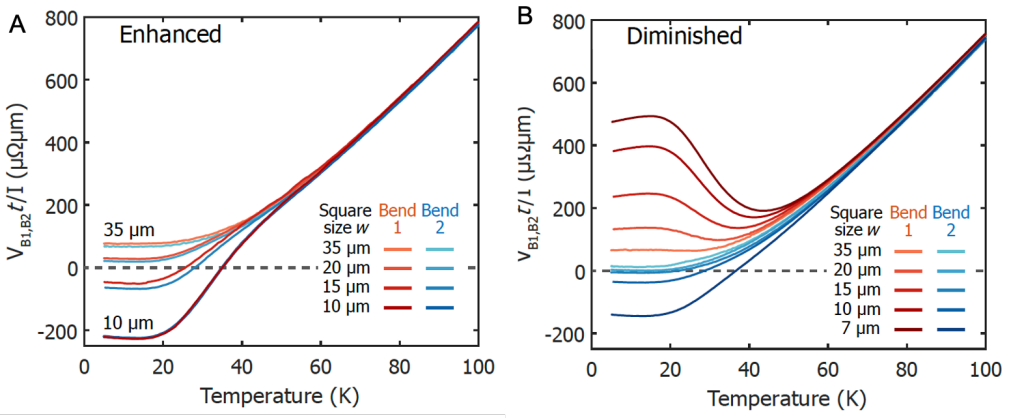

Figure 4.13: Temperature dependence of the bend resistance below 100K: A Enhanced orientation and B diminished orientation.

electrons directions orientated along the diagonal, whereas the diminished orientation has one of the electron directions along the side of the square. The orientation of the Fermi surface can be determined by visible hexagonal growth terraces or crystal edges. In $PtCoO_2$ and $PdCoO_2$ the Brillouin zone is parallel to these edges, with the Fermi surface orientation determined by a 90° rotation.

Within the Ohmic regime both measurements: Bend 1, $V_{B1} = V_{12,43} = V_4 - V_3$ when the current flows from contact 1 to contact 2 and Bend 2, $V_{B2} = V_{23,41}$ should be identical. There is no fundamental reason why in the ballistic regime, anisotropy should arise between the $R_{12,43}$ and $R_{23,14}$ measurements in a square junction. However, all the measurements of these junctions in the ballistic regime have been made in materials with a circular Fermi surface, which would not be expected to lead to anisotropy.

Repeating those measurements on $PtCoO_2$ brings a surprise. The results presented in Ref. [65] show the anisotropy between the $R_{12,43}$ and $R_{23,14}$ coming from the low symmetry of the Fermi surface. Although I co-performed those experiments, I will only summarise them here, because the work preceded the irradiation experiment and has been comprehensively described in [65] and [66]. In these studies, we varied the ratio of the size of the square to the electron mean free path by decreasing the size of the squares by FIB. At

temperatures above 80 K (fig. 4.13), there is little dependence of the voltage on the size of the square, the orientation of the Fermi surface or the choice of bend measurement, as expected within the Ohmic regime. At low temperatures, however, we observed a huge anisotropy in diminished orientation between two bend voltages, though the enhanced orientation did not exhibit this effect. Other surprising results that we observed were ballistic effects at a square size almost twenty times larger than the mean free path. The existence of a strongly faceted Fermi surface in $PtCoO_2$ leads to phenomena not previously observed in any system, opening the possibility of new regimes of mesoscopic physics.

4.3.4 Landauer-Büttiker theory

The novel behaviour observed in delafossite square junction motivated a new theoretical understanding of the ballistic phenomena. With the intrinsic non-locality of the ballistic regime, Ohmic methods of calculating the resistivity were no longer appropriate. Thus, we required a new approach.

We obtained further insight into the symmetries and the physics underlying the data shown in fig. 4.13 by performing a Landauer-Büttiker analysis of the square junctions in Ref. [65]. Landauer [67] had developed an alternative framework in which he considered the current and voltage terminals to be reservoirs of electrons with specific chemical potential. If all the chemical potentials are equal, there is no current. Electrons can flow between terminals by biasing the chemical potentials with respect to one another. Thus, the two-terminal measurement conductance, G, is determined by the probability, T, that an electron at the Fermi energy is transmitted to the second terminal rather than reflected into the first.

Büttiker [68] extended the Landauer formula to include additional terminals. The Büttiker multiprobe formula states that the net current, I_i, out of contact i at zero temperature is:

$$I_i = \frac{2e^2}{h}[(N_i - N_i R_i)\mu_i - \sum_{j,j\neq i} N_i T_{ij} \mu_F \mu_j], \tag{4.9}$$

where μ_j is the chemical potential at contact j, N_j is the number of modes at the Fermi level in contact j, T_{ij} is the probability of an electron at the Fermi energy to be emitted from contact j and transmitted to contact i and R_i is the probability of an electron to be emitted from contact i and reflected back into the same contact. An important note is that $N = k_F c/\pi \sim 12{,}000$ with a typical contact width $c = 4\ \mu m$ in $PtCoO_2$ squares, which is very different to the few modes in the 2DEG devices. Despite this, strongly ballistic behaviour is still observed. Landauer-Büttiker analyses of the bend and Hall voltages within four-terminal junctions are standard [69], but all assume fourfold symmetry between the contacts. We therefore had to perform an analysis specific to our experimental situation.

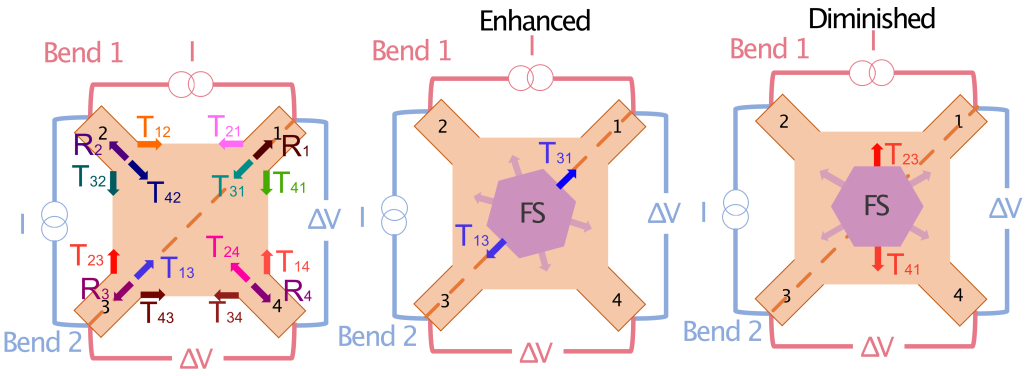

Figure 4.14: The transmission coefficients from each of the contacts in a square device. The measurement configuration for bend voltage in an enhanced orientation device is likely to enhance T_{13} and T_{31} and in a diminished orientation device is likely to enhance T_{23} and T_{41}.

The transmission, T_{ij}, and reflection, R_j, coefficients are normalised such that an electron emitted from a contact is either transmitted to another contact or reflected back into the emission contact: $R_j + \sum_{i,j\neq i} T_{i,j} = 1$. In combination with the geometry of the square with transmission coefficients shown in fig. 4.14 the relevant form of Equation (4.9) for each of the four

contacts can be rewritten in the form a matrix equation,

$$\begin{pmatrix} I_1 \\ I_2 \\ I_3 \\ I_4 \end{pmatrix} = \frac{2e^2N}{h} \begin{pmatrix} T_1 & -T_{12} & -T_{13} & -T_{14} \\ -T_{21} & T_2 & -T_{23} & -T_{24} \\ -T_{31} & -T_{32} & T_3 & -T_{34} \\ -T_{41} & -T_{42} & -T_{43} & T_4 \end{pmatrix} \begin{pmatrix} \mu_1 \\ \mu_2 \\ \mu_3 \\ \mu_4 \end{pmatrix} \tag{4.10}$$

where the normalisation ensures $T_1 = 1 - R_1$ and equivalent expressions for T_2, T_3, T_4 for contacts 2 to 4.

As can be seen in fig. 4.14 in both of the experimental orientations in $PtCoO_2$, contacts 1 and 3 and, separately, contacts 2 and 4 are equivalent in terms of their orientation relative to the hexagonal Fermi surface, which leads to the reduction of the transmission coefficients in the Equation (4.10): $T_1 = T_3$, $T_2 = T_4$, $T_{21} = T_{43}$, $T_{41} = T_{23}$, $T_{32} = T_{14}$, $T_{34} = T_{12}$, $T_{31} = T_{13}$, $T_{42} = T_{24}$. In addition to the symmetries of the transmission coefficients due to the geometry, there are also constraints due to current conservation, which ensures each row and column sums to the same value, and time reversal symmetry, which leads to $T_{ij}(B) = T_{ji}(-B)$ in the magnetic field for all values of i and j.

Equation (4.10) describes a set of four linear equations which must be solved for each of the experimental measurement configurations. This calculation determines the voltage in a single 2D layer. However, in a delafossite metal, there are effectively multiple 2D layers in parallel, with the number equal to $N_L = t/(d/3)$ where t is the sample thickness and d is the c-axis lattice constant. In combination with time-reversal symmetry and current conservation for the electronic transport in this lower-symmetry case it gives the following bend resistances:

$$R_{B1} = \frac{V_{B1}(B)}{I} = \frac{d}{3t}\frac{h}{2Ne^2}\frac{T_{41}T_{32} - T_{31}T_{42}}{D(T_{41} + T_{21})} \tag{4.11}$$

$$R_{B2} = \frac{V_{B2}(B)}{I} = \frac{d}{3t}\frac{h}{2Ne^2}\frac{T_{34}T_{21} - T_{31}T_{42}}{D(T_{41} + T_{21})}, \tag{4.12}$$

where D is a positive-definite collection of transmission coefficients that is symmetric in the field and equal to $T_{41}T_{34} + T_{21}T_{32} + T_{34}T_{31} + T_{32}T_{31} + T_{41}T_{42} + T_{21}T_{42} + 2T_{31}T_{42}$.

In materials with a circular Fermi surface, a collimated beam of electrons is directed along the square diagonal. The enhanced orientation for our hexagonal Fermi surface has the same geometry (fig. 4.14). Therefore, transmission coefficients $T_{31}T_{42}$ become larger than the first numerator term in Equations (4.11) and (4.12), and the bend voltage is negative in the ballistic regime. In the limit that horizontal and vertical transmission are equally likely, $T_{41}T_{32} = T_{34}T_{21}$ and the Bend 1 and Bend 2 voltages are equal.

However, the diminished orientation has another symmetry configuration (fig. 4.14). In this case, a beam of electrons is aligned to the vertical direction, and there are no corresponding horizontal or diagonal beams. Therefore, vertical transmission is significantly more probable than horizontal or diagonal transmission at zero magnetic field in the ballistic regime. Thus, the $T_{41}T_{32}$ term dominates and the bend 1 resistance is positive. At the same time, $T_{34}T_{21}$ is smaller than $T_{31}T_{42}$, which leads to the negative bend 2 resistance.

The Landauer-Büttiker analysis, therefore, shows that anisotropy in the probability of transmission of electrons between contacts originated from the hexagonal Fermi surface can explain the novel anisotropy observed in the ballistic regime junctions. As discussed in more detail in [65], the scale of the observed sheet resistance per Pd layer is also well captured using $N =$ 12,000.

4.4 Irradiation results and discussion

One of the conclusions that we drew in Ref. [65] was that the key parameter controlling the anisotropic ballistic effects described above is the dimensionless ratio l/w. In that project we varied w by keeping l constant. To fully test our hypothesis of l/w scaling, I wanted to do the complementary measurement of varying l in squares of constant w. For this, I made use of the

high energy electron radiation capabilities introduced in Section 3.5.

A simple initial measurement is to compare the temperature dependence of the two bend voltages and magnetoresistance before the irradiation experiment. The results of such measurements are presented in figure 4.15 for a diminished orientation $PtCoO_2$ square. The behaviour of the two bend voltages of an enhanced orientation square is similar to the circular Fermi surface one. Therefore, I concentrated my attention on high energy electron irradiation experiments on the diminished orientation squares.

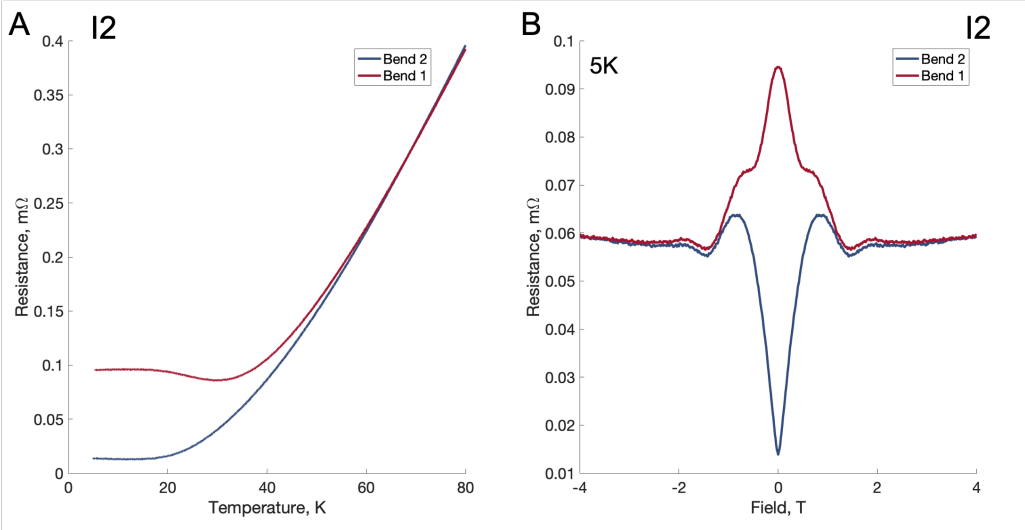

Figure 4.15: A: Cool down of bend 1 and bend 2 measurements of the square I2 with diminished orientation of the Fermi surface B: Magnetoresistance of the bend 1 and bend 2 measurements of the square I2 with diminished orientation of the Fermi surface.

Squares I1, I2 and I3, mounted specifically for high energy electron irradiation experiment using the epoxy-free method described in Section 3.3, have the diminished orientation of the Fermi surface. The length of the square side of I1 and I2 samples is around 15 μm and for I3 is 10 μm, suggesting from our previous results, that all the squares will show ballistic behaviour. This is confirmed by the example data shown in Fig. 4.15 for square I2. The magnetoresistance of this sample shows a strong ballistic anisotropy effect (fig. 4.15B). At zero field, the Bend 2 measurement is qualitatively similar

to those in the enhanced orientation. The Bend 1 measurement, however, has a peak at zero field. At larger magnetic field, the behaviour of both bend voltages becomes nearly identical.

4.4.1 In-situ measurements

The SIRIUS Pelletron linear accelerator allows to perform four-point in situ resistance measurements, and therefore monitor the increase of resistivity as a function of electron dose. However, it is possible to complete the measurement only of one voltage pair during irradiation. Thus, in diminished squares, I measured during the irradiation the bend 1 voltage pair.

The increase of the resistivity of the bulk $PtCoO_2$ S1 sample, as a function of electron dose, is shown in fig. 4.16. The dependence of resistivity on dose is linear. Our detailed defect studies of the bulk $PtCoO_2$ in Ref. [36] prove that the resistivity increase during irradiation is dominated by the defects in the conductive Pt/Pd planes, as expected in such two-dimensional systems.

However, the diminished squares I1 and I3 are in ballistic regime, and the resistivity increment of the bend 1 measurement shown in fig 4.16 are surprising. The data of the sample I3 is normalised between several irradiation steps due to the annealing. At low doses, when the defect concentration is still small, the resistivity increment of both square samples I1 and I3 is negative, i.e. as we introduce defects in the system, the resistance drops down! The resistivity increment is much lower in the I3 sample, probably due to the different initial purity of the samples.

Even though these results could seem at first glance counterintuitive, it proves the above assumption that the induced anisotropy is a result of the symmetry lowering by the sample shape and symmetry of the Fermi surface. Introduced point-like defects decrease the mean free path of electrons, and therefore, we can observe the ballistic-diffusive crossover. The drop in resistivity at low doses comes because the bend 1 resistance was enhanced over the bulk value due to ballistic physics that the irradiation suppresses. With the increase of the defect concentration, the resistivity increment increases,

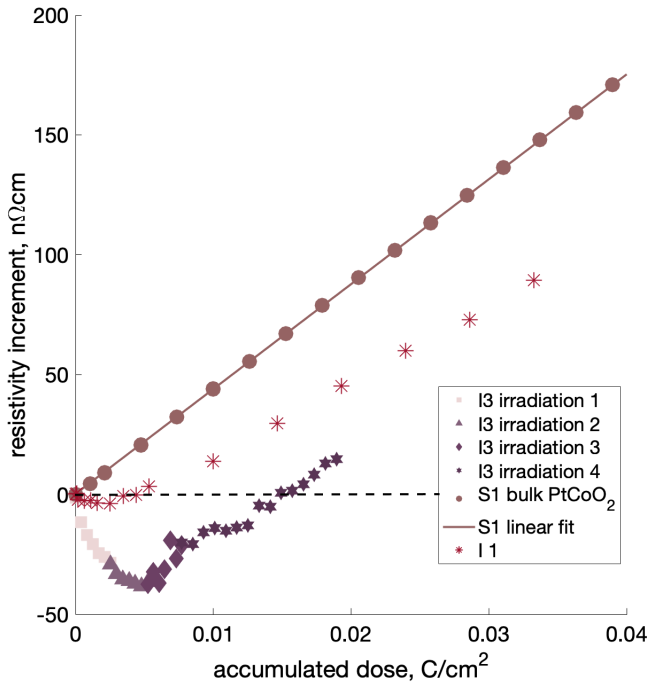

Figure 4.16: Resistivity increment of the bulk $PtCoO_2$ S1 sample with linear fit and bend 1 of two squares with diminished Fermi surface orientation during irradiation. The total dose is calculated using expression (3.1). The data of the sample I3 is normalised between several irradiation steps due to the annealing

and at higher electron doses, it becomes linear with the slope close to that of the bulk sample. Thus, the characteristic peak and a trough in bend 1 and bend 2 voltages at zero magnetic field shown in fig. 4.15B should shift closer during irradiation and become isotropic at the dose when the resistivity increment is the same as that of bulk material.

4.4.2 Elimination of anisotropy

I performed several magnetoresistance measurements at different electron doses to estimate the ballistic-diffusive crossover more quantitatively and qualitatively. The bend 1 and bend 2 resistances of the square I2 in the magnetic field normalised by the values before irradiation are shown in fig.

4.17. In each case, the quantity plotted is $V_{B1,B2}t/I$ where I is the measurement current, and t is the square thickness, to compare the irradiation data to that of the previous experiment on squares with variable width [65]. The thickness of the sample I2 is 1.3 μm. The magnetic field is applied along the c-axis.

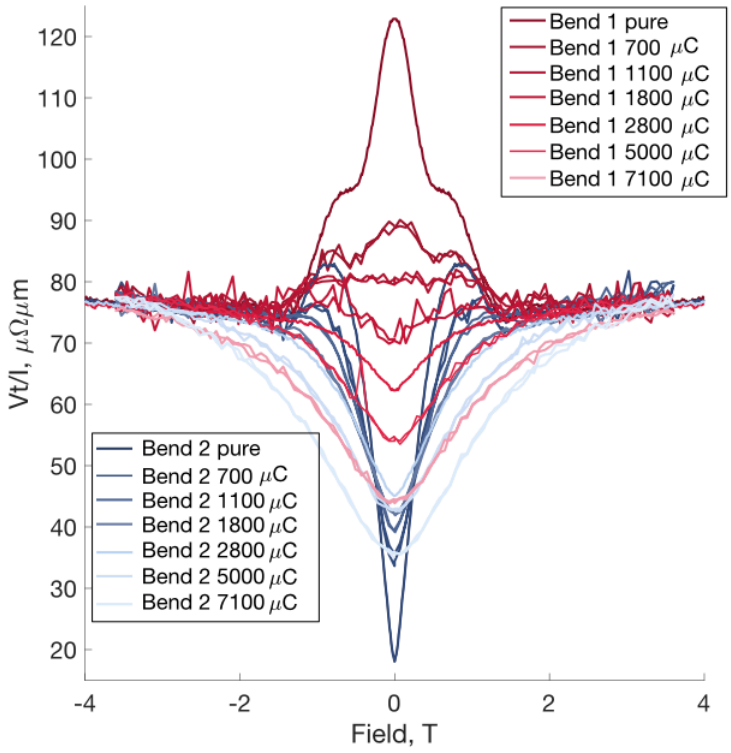

Figure 4.17: The magnetic field dependence of $V_{B1,B2}t/I$ at 5 K for I2 square with diminished orientation of the Fermi surface for several irradiation steps. Dose is in charge units.

In the pure square bend 1 and bend 2 resistivities exhibit strong ballistic behaviour. The bend 1 measurement has a peak at zero magnetic field, and bend 2 resistance has a trough. At a small dose of electron irradiation, the bend 1 resistivity changes significantly, but the bend 2 measurement does not undergo significant changes. The trough in bend 2 resistance measurements becomes smaller as the introduced defect number increases. The bend

1 resistance changes its behaviour dramatically with the rise of the electron dose, and at zero magnetic field also has a trough. However, there is still a difference between the two bend measurements. At high doses of electron irradiation, the trough in the bend 2 measurement becomes wider in a magnetic field and has a form of magnetic field dependence closer to that of bulk material. At the final dose of electron irradiation of 7100 μC, which equals a Frenkel pair concentration around 0.02% [36], the two bend voltages are not the same, even though both resistivities have similar dependence in magnetic field. At large magnetic field values, above around $w/r_c = 2$, the behaviour of both bend voltages becomes nearly identical. This suggests that electrons have tiny cyclotron orbits in comparison to the device size and transport becomes diffusive.

4.4.3 Determination of mean free path

An essential limit in any ballistic regime is how an effect decays as the various length scales are changed. In previous studies [65] of the ballistic effects in $PtCoO_2$ squares, we examined this decay by changing the square size. In the irradiation experiment, I change the mean free path of the sample, leaving the geometry of the square untouched. It is essential to accurately determine the mean free path to compare the geometric and electronic transport length scales between different squares.

In the Ohmic regime, for material with resistivity ρ, the transport mean free path, l, which is an average around the Fermi surface, can be calculated from the Drude formula (2.1):

$$l = \frac{m^* v_F}{ne^2\rho}, \tag{4.13}$$

where m^* is the effective mass of the transport electrons, v_F is the Fermi velocity, e is the electronic charge, and n is the density of carriers.

The derivation of this equation relies upon the existence of a local relationship between the current density and the electric field. However, that

does not exist in the ballistic regime, and the resistivity is undefined due to this intrinsic non-locality.

The desired mean free path is the value in a bulk device when the boundary scattering does not significantly contribute to the overall resistance, and the transport behaviour is diffusive. This property is nontrivial to determine when due to the design of the experiment, the initial size of the square is 15 μm. Another challenge is to determine the mean free path during irradiation, as it is changing.

The resistivity of the bulk crystal changes during irradiation from ρ_0 by $\Delta\rho$ as follows:

$$\rho = \rho_0 + \Delta\rho, \Delta\rho \propto Dose \tag{4.14}$$

thus,

$$l = \frac{C}{\rho} = \frac{C}{\rho_0 + \Delta\rho}, \tag{4.15}$$

where C is some constant.

However, the value that we are interested in is the ratio of the width of the sample to the mean free path. It depends on the irradiation dose in a following way:

$$\frac{w}{l} = \frac{w(\rho_0 + \Delta\rho)}{C} = \frac{w * Dose}{C_2} + \frac{w * \rho_0}{C}, \tag{4.16}$$

where C and C_2 are different constants.

To apply this method, the value w/l should be linear in the dose so that we can scale the dose axes to the non-irradiation results.

However, there is also the second possibility of mean free path determination. At high fields, as it is seen from the magnetoresistance data in fig. 4.17 many of the ballistic effects are suppressed. There is no clear dependence on the square size or mean free path, Fermi surface orientation or bend measurement configuration, suggesting that the behaviour is approximately diffusive.

Suppose the behaviour at high field values is assumed to be diffusive. In that case, the high field resistance and bulk sample magnetoresistance can be used to estimate the Ohmic contribution to the resistance of a square at

zero field. This would be the zero-field resistance for the bulk sample as if ballistic effects are negligible. Expressions from the diffusive regime can then be used with this value to determine the mean free path. This is supported by the fact that the cyclotron radius above 4 T is below 1.3 μm, much less than half of the irradiation square contacts' width, thus suggesting that the electrons are less able to sense the experimental geometry.

Therefore, to estimate the mean free path of the square during irradiation, I measured the resistance of two bend contacts at the magnetic field of 4 T. At this magnetic field, both bend resistances are almost the same, ensuring the elimination of the ballistic effect by the magnetic field. I used the magnetoresistance of the bulk $PtCoO_2$, known from a previous study [32] to estimate the Ohmic resistance contribution at zero field for the sample before irradiation. However, this approach to calculating the mean free path suffers complications as we irradiate the sample, because the value of magnetoresistance also changes during irradiation. Previous high energy irradiation studies of bulk $PtCoO_2$ [66] helped to estimate the diffusive resistance contribution at zero field for the square device during irradiation. The resistivity of the square was calculated via the Van der Pauw equation (4.8), and the mean free path was then estimated using the Ohmic expression (4.13). The mean free path of the samples I2 and I3 estimated by this method is shown in a table 4.1 below.

Table 4.1: Estimated mean free path

Total dose, μC	mfp of I2, μm
0	5.6
700	4.3
1100	3.7
1800	3
2800	2.3
5000	1.7
7100	1.3

Total dose, μC	mfp of I3, μm
0	7.4
400	6.0
800	5.1
1200	4.2
2800	2.7

4.4.4 Decay of ballistic anisotropy

The limits of this ballistic behaviour can be better characterised by quantifying how the anisotropy decays as a function of the mean free path. In previous studies, the depth of the dip in the magnetoresistance was used as a scale of the strength of the ballistic effects. A negative bend resistance observed in CVD-grown graphene was interpreted as demonstrating ballistic transport over at least 28 μm [70].

The form of the decay of the ballistic effect was studied in semiconductor heterostructures [71, 72, 49] The resistance, $\Delta V/I$, is usually shown to decay exponentially as:

$$\frac{\Delta V}{I} \propto e^{-\frac{w}{l_B}}, \tag{4.17}$$

where w is a characteristic length scale of the ballistic device, l_B is a fitted ballistic mean free path.

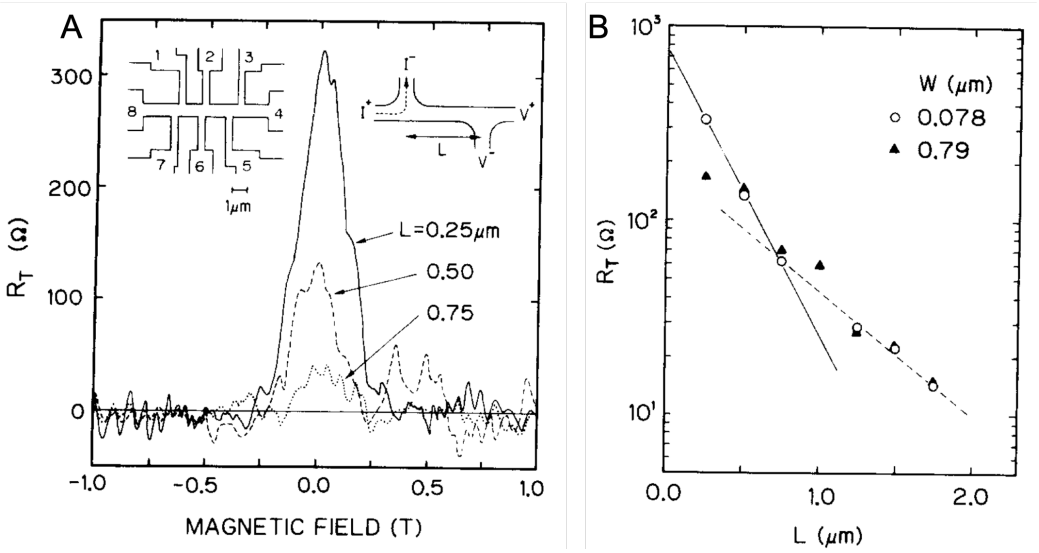

Figure 4.18: A: Magnetic field dependence of the resistance at different length L and a sketch of the device. B: The dependence of the junction resistance R (the size at zero field) on the length L for channels of two different widths W in a GaAs-AlGaAs 2DEG, reproduced from [71]

Sakamoto *et al.* [71] carefully studied the decay of the ballistic effects by measuring the transfer resistance of the device with the geometry shown in

fig. 4.18A. In the limit with $L = 0$, these junctions are typical cross junctions with width W. In the diffusive limit, when $L > W$, the voltage should be approximately zero as the voltage contacts are separated from the current path. However, in the ballistic regime, the picture is different. Electron trajectories along the axis of the device led to a non-zero voltage response at zero field shown in fig. 4.18A, as in the bend resistance. Fig. 4.18B shows the decay of this feature as a function of the length L. If the width of the junction is small enough, exponential decay with two different regimes occurs [72, 49]. The rapid decay at small L is attributed to boundary scattering within the junction and the slow decay at larger values of L to scattering within the bulk. The rapid decay is more sensitive to the boundary scattering specularity, while the slow decay length is more sensitive to impurity scattering in bulk.

In ballistic studies, the depth of the dip in the magnetoresistance at zero field serves as an indicator of the size of the ballistic effects. In a similar vein, I used the difference of resistance value $\Delta Vt/I$ between two bend voltages in the diminished orientation of the squares at zero field at 5 K. An example of the data before irradiation with method for determining the resistance is shown in fig. 4.19A. In the diffusive regime, this difference is zero. However, this is not the case for the trough alone, as it remains finite in the diffusive regime if the material has a bulk magnetoresistance. Thus, such an approach has more advantages for the delafossite materials as it allows the separation of the ballistic contribution from the Ohmic, ensuring the ΔV is a highly sensitive parameter for estimating the size of the ballistic signal.

Figure 4.19B shows the variation of $\Delta Vt/I$ with the ratio, w/l, of the square side w, to the mean free path l calculated in the previous section, for the two irradiated squares I2 and I3. The rate is similar between these two squares. However, there are two distinct regimes. At the small values of w/l, the decay is more rapid. When $w/l \sim 5$, the decay becomes slower. The decay exhibits the slow rate to at least $w/l \sim 13$, far beyond the traditional limits of the ballistic regime of $w/l \sim 1$.

There is also a good agreement between irradiation data and exponential

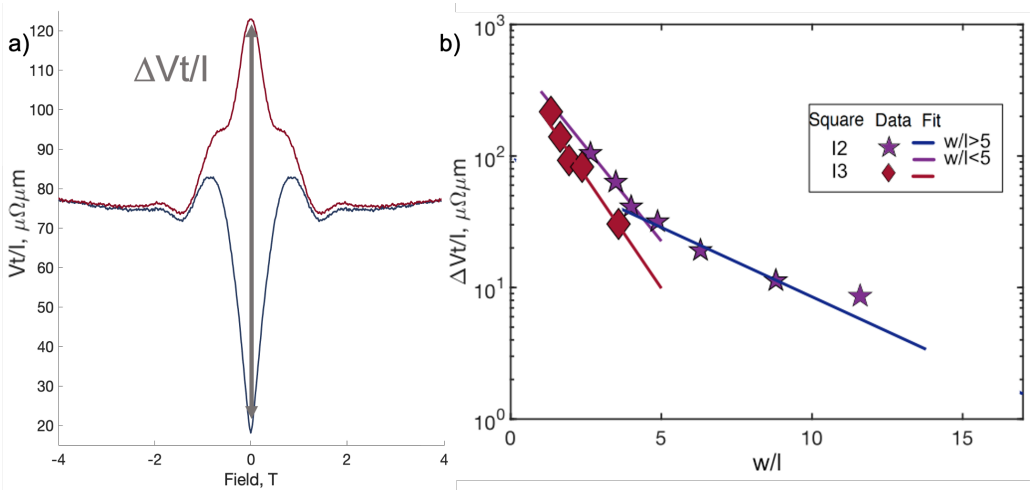

Figure 4.19: The decay of the difference between the peak and trough, $\Delta Vt/I$ as a function of the ratio of square size and mean free path for two irradiated diminished squares

decay (4.17) with two fitting constants:

$$\frac{\Delta Vt}{I} = Ae^{-\frac{b*w}{l}}, \tag{4.18}$$

where A is a constant and b has two different constant values: b_S and b_F as the decay has two distinct regimes: when $w/l < 5$ and $w/l > 5$.

The comparison of the ballistic decay between the irradiated squares and our previous studies [65] is shown in fig. 4.20. The magnitude of $\Delta Vt/I$ in squares D1 to D4 is measured in the same way as in fig. 4.19A. The orientation of the Fermi surface of squares D1 - D4 is the same as in I2 and I3 squares. The only difference between the D squares and two I squares is the method of changing the value of w/l. In D-squares, the mean free path was constant, and we changed the w of the square using FIB. Despite the completely different experimental methods, the ballistic decay is similar between D-squares and irradiated squares. The slopes of the two distinct regimes are also close to each other. And at the value of $w/l \sim 5$, the decay changes its behaviour.

For the rapid decay, when $w/l < 5$, the fitting constants b_F of (4.17)

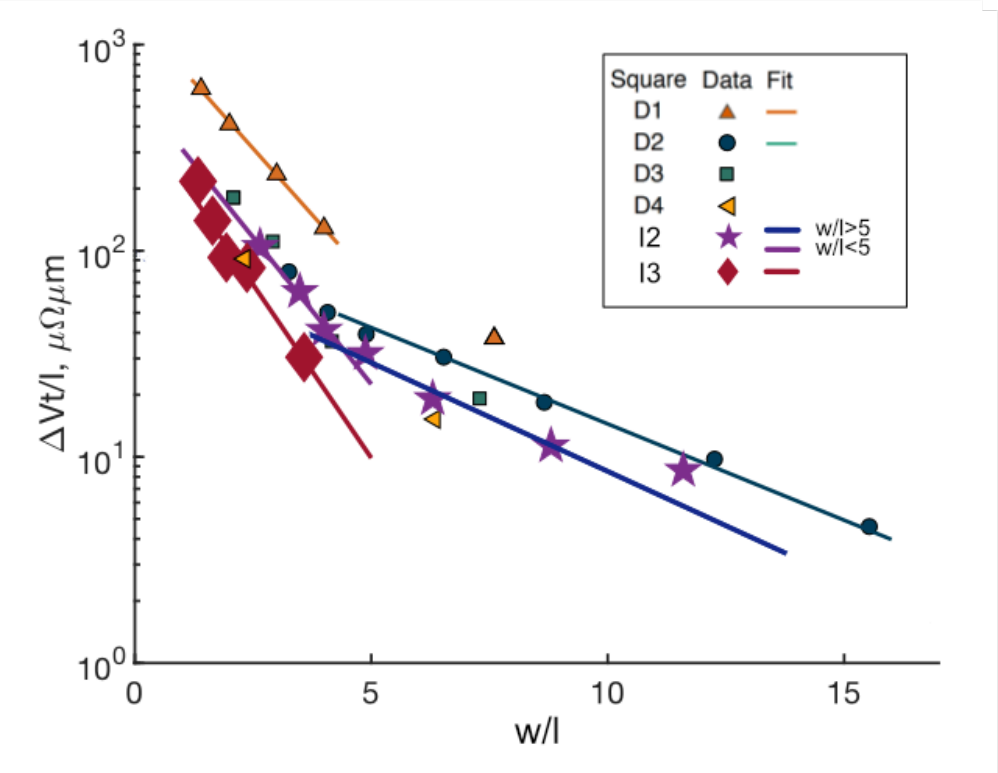

Figure 4.20: The decay of $\Delta Vt/I$, where ΔV = V_{B1} - V_{B2} at zero field, as a function of the ratio of the square side w to the mean free path l for four diminished orientation non-irradiated squares, D1 to D4, and irradiation results of I2 and I3 squares. Data courtesy of P. H. McGuinness

for irradiated squares I2 and I3 are 0.65 and 0.7 correspondently, which is in good agreement with the result from the non-irradiated D-sqaures, b_F = 0.65 [65]. At $w/l > 5$, the decay is a factor of three slower, with $b_S = 0.23$ for irradiated I2 square and $b_S = 0.21$ for D-squares.

On a qualitative level, this double decay agrees with the peak measured

within the transfer junction geometries in fig. 4.18. However, its origin is uncertain. It is important to note that the previously reported decay lengths were always smaller than the mean free path l. However, in $PtCoO_2$, the characteristic decay length, l/b, is around $1.5l$ for the rapid decay and $4.8l$ for the slow decay.

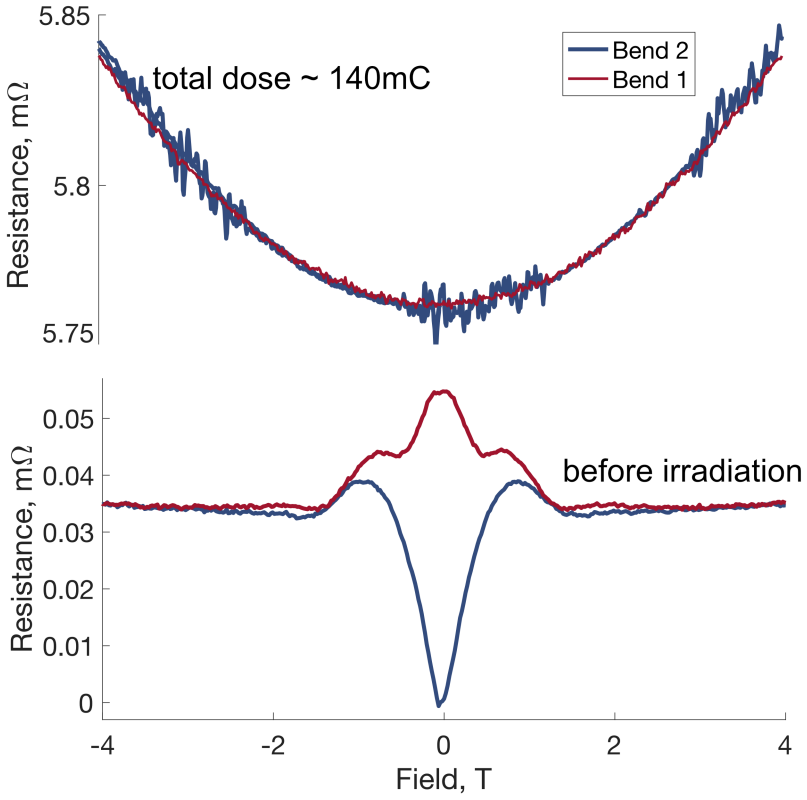

Figure 4.21: Resistance in the magnetic field before and after high dose of irradiation of the I1 diminished square. Upper graph has a large offset.

A possible reason for the long range of ballistic effects in $PtCoO_2$ is the non-circular Fermi surface. The transfer junction studies reported before have been performed on materials with circular Fermi surfaces. If an electron with a circular Fermi surface scatters on a defect in the bulk of the device, there is a vanishing chance that the direction of motion stays the same. However, in a hexagonal Fermi surface, there are only six primary electron

directions. Thus, the chance of the direction of motion after scattering not changing significantly increases.

During this irradiation experiment, I decreased the mean free path of the I2 square almost by a factor of four. However, as seen in fig. 4.17 this irradiation dose did not eliminate the ballistic effect completely. Thus, square I1 received a total dose of high energy electron irradiation of approximately 140mC, almost twenty times higher than the total irradiation dose of square I2. Before irradiation, the magnetoresistance shown in fig. 4.21 exhibits strong ballistic behaviour similar to all of the diminished squares. However, both bend 1 and bend 2 measurements are identical after irradiation, indicating that the higher dose of irradiation eliminated the anisotropic ballistic effect. This reaffirms that observed anisotropy originates from lowering symmetry by the device's geometry and the symmetry of the Fermi surface.

4.5 Conclusions

In conclusion, in this chapter, I explored the behaviour of micro-scale $PtCoO_2$ square-shaped junctions and bar-shaped ballistic devices. These devices have shown strongly ballistic behaviour but have also demonstrated a novel resistance anisotropy not observed before in other materials.

I performed a high energy electron irradiation experiment to study the origin of this induced anisotropy. The experimental data proves that this anisotropy in the ballistic regime stems from the non-circular Fermi surface of $PtCoO_2$ and symmetry lowering by device shape.

The level of anisotropy can be controlled by the length of the mean free path and the orientation of the Fermi surface. The scale of the anisotropy is a sensitive parameter for the size of the ballistic effects. In the square devices, this parameter decays with the rate that depends only upon the ratio of the mean free path to the square size length. The size of this ratio distinguishes two distinct decay regimes. These studies show, for the first time, that ballistic behaviour in the delafossite metals persists far outside

the typical definition of the ballistic regime, when the mean free path and square size are equal, possibly due to the non-circular Fermi surface.

The observed behaviour highlights the importance of carefully considering the Fermi surface symmetry when studying transport within ultra-pure materials. These studies emphasize the significance of including an accurate representation of the Fermi surface in theoretical modelling of ultrapure materials and considering the possible unconventional and long-range nature of any observed ballistic effects.

Chapter 5

The magnetic delafossite metal $PdCrO_2$

In the previous chapters, I have discussed the physics of the ultrapure metals, that belong to the delafossite family. In the whole group of delafossite materials, $PtCoO_2$ and $PdCoO_2$ exhibit exceptional properties because they are extremely pure as grown. In this chapter, I will discuss the physical properties of another exciting compound that belongs to this group. As I will show later, $PdCrO_2$ has a structure similar to that of $PdCoO_2$. The similar ionic picture of these two compounds influences the conformity of several physical properties. However, $PdCrO_2$ brings an essential peculiarity to the discussed $PdCoO_2$ heterostructure. Without changing the unique layered structure, it appends magnetism into it. These gifts of nature provide a unique opportunity to gain insight into the underlying physics by comparing two materials that are sufficiently similar that their differences can clearly be distinguished.

One such comparison concerns the transport properties of $PdCrO_2$. Direct comparison with those of the non-magnetic sister compound $PdCoO_2$ reveals significant extra scattering, which seems to originate in coupling to the antiferromagnetic-insulating layer. Intriguingly, at high temperatures, the scattering rate per kelvin is well approximated by the ratio of the Boltzmann constant to the Planck constant divided by 2π. The same behaviour

exists across many material classes including heavy fermion compounds and high temperature superconductors [73]. Since there is not yet a full understanding of this quasi-universality, $PdCrO_2$ might serve as a test-bed with which to compare the results of calculations aiming to address the issue.

5.1 Magnetic structure of $PdCrO_2$

In Chapter 2, I described the sister compound to $PdCrO_2$, $PdCoO_2$. The structure of these two compounds is similar: triangular coordinated ions of A^+ are situated between BO^{-2} octahedra (fig. 5.1) [74]. As in $PdCoO_2$, correlations are weak in the Pd^{1+} conductive layers. Unlike the non-magnetic $3d^6$ configuration of Co^{3+} in $PdCoO_2$, Cr in the CrO_2 layer has the configuration $3d^3$. First-principles calculations of the electronic band structure, Fermi surface and density-of-states (DOS) of $PdCrO_2$ show that two bands cross the Fermi level. Simple electron counting in the absence of correlation would say that the Fermi level should now sit in narrow Cr-derived bands [75, 76]. However, the ionic picture says that Cr^{3+} should be in a spin-3/2 state due to on-site correlation, and a large local moment, in real $PdCrO_2$ CrO_2 layers should be correlated electron insulators [5]. Thus, calculations in [75] were also performed for the non-collinear antiferromagnetic phase. The mostly Cr d-electron Fermi surface sheet becomes fully gapped at the Fermi level because of the magnetic ordering. Only one band crosses the Fermi level, which is then folded into the smaller magnetic Brillouin zone. At the Fermi level, the character of this band is mostly that of Pd d-states.

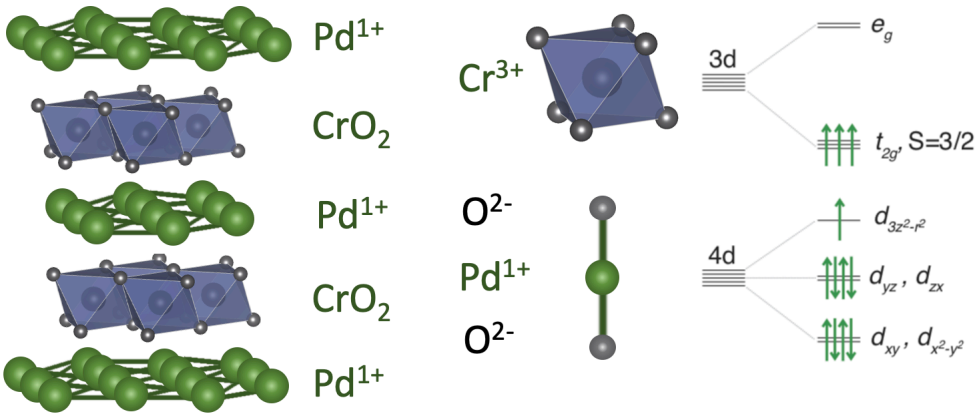

Figure 5.1: Crystal structure of $PdCrO_2$

The nearly octahedral crystal field splits the degenerate 3d electrons into

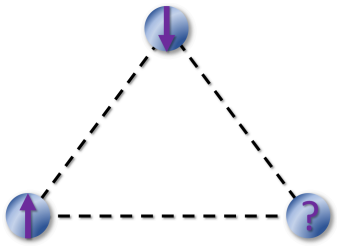

Figure 5.2: Example of the spin localisation in a frustrated system

t_{2g} and e_g orbitals [76]. In fig. 5.1 electrons of Cr site are placed in the t_{2g} level. Because Cr^{3+} has 3 electrons, the t_{2g} level is half-filled with expected sizable local Coulomb interaction. Strong Hund's rule coupling aligns the spins on each Cr site, giving a total spin of nearly 3/2, in this way we can say that the CrO_2 sheet is a Mott insulator [76, 77]. In the work [77], Frank Lechermann called this material a ' hidden Mott insulator' due to its real-space-selective insulating regime and good metallic system.

Mekata *et al.* confirmed the hypothesis of antiferromagnetism with the Neel temperature about 38 K by a neutron scattering experiment [78]. Local spins of the CrO_2 layer in a triangular lattice are unable to select a conventional antiferromagnetic configuration. The structure in the fig. 5.2 is said to be 'frustrated'. When the system is frustrated, it cannot minimise its total classical energy by reducing the interaction energy between each pair of interacting degrees of freedom, pair by pair. To relieve the frustration, the spins form commensurate states, rotating by 120°, to create an ordered magnetic state. Geometric magnetic frustration, where the exchange interactions between spins cannot be simultaneously satisfied, is interesting because it can lead to novel ground states and unusual excitations. It is vital to understand the mechanisms by which magnetic order condenses on frustrated lattices.

The Cr site spins start to arrange themselves into short-range, 120° antiferromagnetic order at 200 – 300 K [78, 76, 5]. However, the interlayer coupling is frustrated because Cr sites in each layer are centred between the Cr sites in adjacent layers. As the temperature decreases towards the

Neel temperature, the in-plane correlation length grows to 20 lattice spacings without interplane coherence. Then the layers lock together and form long-range order.

The authors in [79] proposed two possible scenarios of how magnetic order in $PdCrO_2$ is formed. The first one is called non-coplanar magnetic structure. It is originally referred to as a geometrical concept. In this proposed structure spins in each triangular *ab* layers lie in a vertical plane and change orientation from layer to layer. It exchanges clockwise and anticlockwise rotation in different Cr layers. The second possible structure of the system is coplanar. Unfortunately, it is very similar to a non-coplanar one, and they could barely be distinguished from each other by neutron scattering data.

To resolve this puzzle, Sun et al. in [80] performed neutron scattering measurements under applied uniaxial stress and applied magnetic field. They showed that the magnetic order of $PdCrO_2$ releases interlayer frustration by spontaneously lifting the three-fold rotational symmetry of the nonmagnetic lattice. Their experimental data proves that in an unstrained structure the rotational symmetry breaking appears in two aspects: the spins lie in the yz plane, and from plane to plane the magnetic order shifts along the y axis. The authors also presented resistivity measurement of the single crystal under applied uniaxial stress. The resistivity measurements, however, can not detect this rotational symmetry breaking. Electronic transport data indicates the presence of low-energy spin-wave modes when the lattice is close to triangularly symmetric.

5.2 Electronic structure of $PdCrO_2$

Another evidence that the CrO_2 layer is an insulator is the similarity of the Fermi surfaces of $PdCoO_2$ and $PdCrO_2$ above the Neel transition (fig. 5.3). The first experiment on studying the $PdCrO_2$ Fermi surface was reported by Sobota et al. [81]. They successfully distinguished surface and bulk states and showed that the bulk Fermi surface of $PdCrO_2$ at 50 K is almost identical

to that of nonmagnetic $PdCoO_2$. The bulk FS consists of a single hexagonal electron pocket attributed to one Pd 4d conduction electron per unit cell. This electronic structure shows a strong correspondence to that of $PdCoO_2$, consisting of a single hexagonal electron pocket from its Pd 4d electrons [27]. There is no scenario of how that can happen without CrO_2 being an insulator [5, 82]. However, the significant differences between the behaviour of $PdCrO_2$ and $PdCoO_2$ are expected below the antiferromagnetic transition. If it is true, and coupling between the conductive and magnetic layers is strong, then the Pd conduction can be used as a probe of the magnetic order.

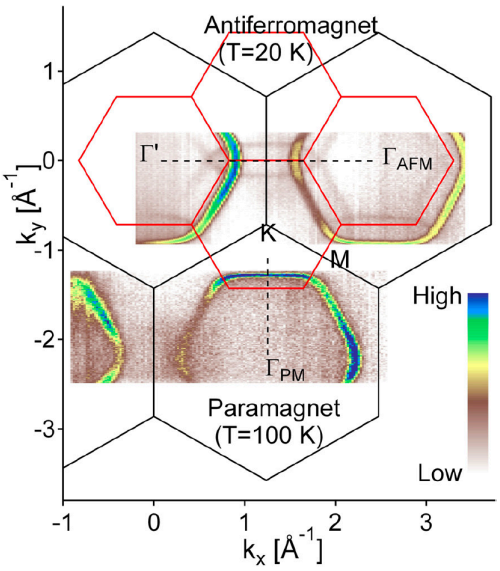

Figure 5.3: Photoemission spectra at 100 K in the paramagnetic state of $PdCrO_2$ show a single hexagonal Fermi surface (bottom), while those at 20 K show extra band folding (top). Figure from Noh et [83].

Sobota *et al.* [81] performed a number of band structure calculations. In these calculations, they computed the bulk band structure with antiferromagnetic spin configuration. The calculated Fermi surface was originating from a single hexagonal pocket and then folded into the antiferromagnetic Brillouin zone. This result of the first calculations proves that antiferromagnetic CrO_2 layer affects the Pd conduction. Unfortunately, in this work, they did not get an ARPES experimental results proving the calculations.

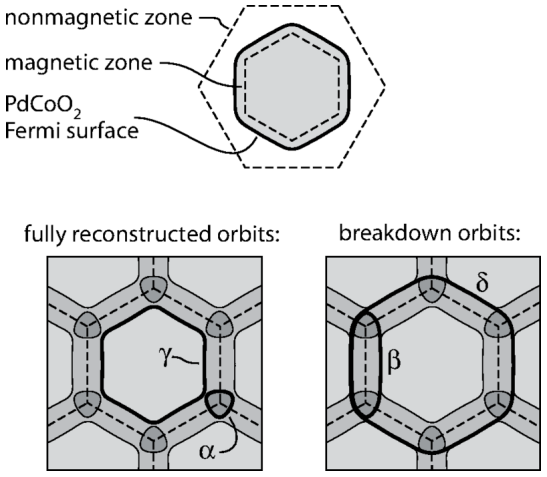

Figure 5.4: A two-dimensional model of the reconstruction. Top: the PdCoO2 Fermi surface in the 2D nonmagnetic zone, and magnetic zone arising. Bottom: reconstruction into the magnetic zone. The fully reconstructed orbits α and γ are illustrated in the left-hand panel, and the breakdown orbits β and δ in the right-hand panel. Figure from Hicks et [76].

Hicks *et al*. [76] reported qualitatively identical dHvA data to those of Ok et al [84] and performed an extended analysis. They showed how the $PdCrO_2$ Fermi surface could be reproduced by reconstructing the (nonmagnetic) $PdCoO_2$ Fermi surface into a reduced zone corresponding to a magnetic cell containing six Cr sites. They reported frequencies and effective masses for four quasiparticle orbits (fig. 5.4): α and γ - fully reconstructed orbits, β and δ - orbits coming from the breakdown effect. The effective mass and frequency of the δ orbit are very similar to the equivalent orbit in $PdCoO_2$. The β and δ orbits appear because the energy gap in the reconstructed band structure is no longer larger than $\hbar\omega_c$ (ω_c is a cyclotron frequency). In other words, electrons approaching the gap can tunnel through and jump to the other orbit [85].

Hicks et al.'s Fermi surface reconstruction can be understood in the following way. When electrons feel an additional periodic potential, due to magnetic order, the band structure is reconstructed. We can reconstruct the Fermi surface of the $PdCrO_2$ from the $PdCoO_2$ one by translating the non-

magnetic Fermi surface sections by combinations of reciprocal lattice vectors of the reduced zone until all portions of the original surface are within the reduced zone [76].

However, this standard picture could not explain the experimental observations of $PdCrO_2$ ARPES results reported by Sunko *et al.* in Ref. [82]. They discovered that replica features of $PdCrO_2$ Fermi surface need a different explanation: Mott insulator - free-electron coupling. Sunko and co-authors proved that the coupling allows the Pd electrons to feel the periodic potential due to the antiferromagnetic order, that this effect is far too weak to give a full replica band. However, when in the ARPES experiment, they removed an electron from the Mott-insulator layer, an electron from the conductive Pd layers hop to the magnetic layer. They deduced a $PdCrO_2$ Hamiltonian in which Kondo coupling is an interlayer effect. This Hamiltonian (5.1), with three hopping terms, describes the coupling between conductive and Mott-insulting layers in this material.

$$H_{eff} = -t_p \sum_{ij\sigma}^{n.n.} p^+_{i\sigma} p_{j\sigma} + \frac{4t_c^2}{U} \sum_{<ij>}^{n.n.} S_i S_j + \frac{4}{U} \sum_{ijk\sigma\sigma'}^{n.n.} g_{ij} g_{kl} p^+_{i\sigma} (S_j \sigma_{\sigma\sigma'}) p_{k\sigma'} \quad (5.1)$$

Here the first term denotes the hopping between Pd sites, the second term describes the effective spin-spin exchange in the Mott layer, and the last term describes a Kondo coupling between the localised Cr spin and Pd electrons on the neighbouring sites. The simple fig. 5.5 shows the hopping between sites with the proposed coupling.

This work [82] experimentally proved and described the special coupling that exists in $PdCrO_2$. $PdCrO_2$ therefore is a benchmark system for studies of the triangular lattice Hubbard model and Mott insulator-free electron coupling.

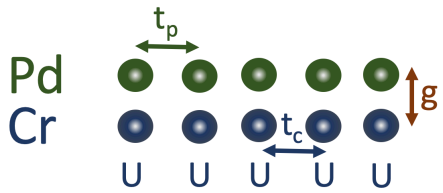

Figure 5.5: Hopping within (t_p, t_c) and between (g) the layers, and the on-site Coulomb repulsion on the Cr sites (U).

5.3 Transport properties of $PdCrO_2$

In previous sections, I described the magnetic and electronic structure of $PdCrO_2$ and discussed strong coupling between Mott insulating and conductive layers. The main question that I would like to discuss in this section is how this coupling affects electronic transport in $PdCrO_2$? As in $PdCoO_2$, the conduction of electrons happens in the Pd layer. But unlike $PdCoO_2$, the CrO_2 layer introduced antiferromagnetism in the system [5]. Thus, the transport properties of $PdCrO_2$ become of considerable interest.

In the work [76] Hicks *et al.* measured not only the dHvA effect in $PdCrO_2$ but also resistivity up to 500 K. They compared the resistivity of the $PdCrO_2$ with the non magnetic analog $PdCoO_2$ (fig. 5.6). Detailed measurements and analysis of the magnetisation and resistivity along the c-axis and in the ab plane were performed in work [12]. In both these works, the reported room-temperature resistivity of the $PdCrO_2$ is around 8.2 $\mu\Omega cm$ and anisotropy ratio $\rho_c/\rho_{ab} > 150$.

In fig. 5.6 there is a sharp cusp in the $PdCrO_2$ resistivity at T_N. Above the Neel temperature, the magnetic component of the resistivity remains well below its saturation value due to short-range correlation. In contrast to $PdCoO_2$, the $PdCrO_2$ resistivity is essentially linear from ~ 200 to at least 500 K. We can estimate the magnetic component of the resistivity by subtracting the resistivity of $PdCoO_2$ from that of $PdCrO_2$. This magnetic component continues to increase at temperatures well above room temperature, i.e.,

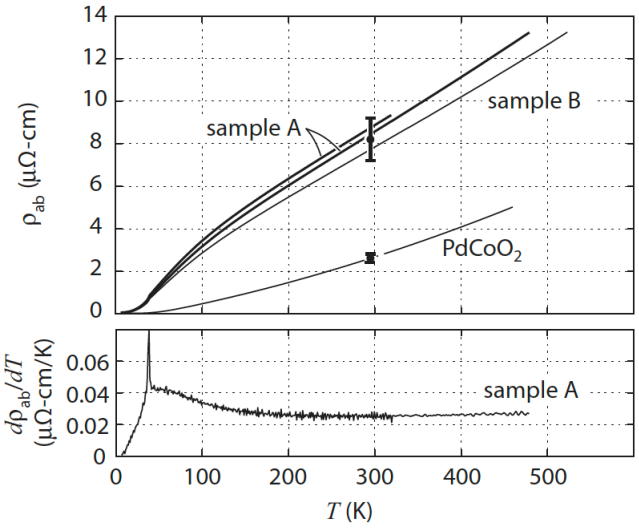

Figure 5.6: The resistivity of $PdCrO_2$ against temperature, for two samples and temperature dependence of the $PdCoO_2$ resistivity. Bottom panel: $\delta\rho/\delta T$ for sample A. Figure from Hicks et [76].

it continues to evolve to temperatures an order of magnitude greater than T_N due to short-range correlation. The increase and eventual saturation of the magnetic component as the temperature increases leads to a convex temperature dependence of the resistivity [76, 12]. The Weiss temperature of $PdCrO_2$ is around - 500 K [86]. So we expect the correlations between the Cr spins to persist to high temperatures.

The temperature derivative of the resistivity exhibits a clear peak at the Neel temperature (fig. 5.6). As temperature decreases, the magnetic component of the resistivity starts to decrease from temperatures well above the Neel temperature and suddenly drops at the Neel temperature. This happens because of the reduction of the randomness of the magnetic spins, associated with developing short-range spin correlation above the Neel temperature and long-range antiferromagnetic order at the Neel temperature [12, 78]. Such a temperature dependence of the resistivity indicates that the frustrated Cr spins affect the motion of the conduction electrons in the Pd layer.

In Ref. [87] Daou *et al.* performed a transport calculation for $PdCrO_2$.

At temperatures higher than the Neel temperature, the band structure of $PdCrO_2$ is very similar to that of the non-magnetic analogue $PdCoO_2$. They also extended the model to include magnetic scattering. The effect of incoherent magnetic scattering, when collisions randomise the electron direction, can only change dependence of the relaxation time on wave vector k. In turn, coherent magnetic scattering does not randomise the electron velocity, but it links two points on the Fermi surface via the magnetic wave vector. When the temperature reaches the Neel temperature, this leads to the opening of gaps at these points and reconstruction of the Fermi surface. The opening of gaps also heads to a loss of incoherent magnetic scattering from these regions. So, there is a small drop in resistivity at the Neel temperature in a zero field. As I discussed above, magnetic fluctuations exist on short length scales above the Neel temperature. They can cause scattering of both types without reconstructing the Fermi surface [87].

Conducting magnets display extraordinarily large anomalous Hall effects (AHE). One year after discovering the Hall effect, Hall reported that his effect was ten times larger in ferromagnetic iron [88]. This strong effect that he discovered in magnetic conductors is called the anomalous Hall effect. The anomalous characteristics of the Hall effect in ferromagnets and strong paramagnets was first explained theoretically by Karplus and Luttinder in [89]. They showed that electrons have an additional contribution to the group velocity in the external electric field applied to the solid due to the spin-orbit coupling. In the ferromagnetic conductor, the sum of these velocities over all band states can be non-zero and contributes to the Hall conductivity. Because this theory depends only on the band structure and does not contain impurity scattering, it is an intrinsic contribution to the AHE. Empirically, we can write the contribution to the Hall effect as:

$$\rho_H(H,T) = R_0(T)B + 4\pi R_s(T)M, \tag{5.2}$$

where R_0 is the ordinary Hall coefficient, and R_s is the anomalous Hall coefficient that characterises an additional contribution and M is magneti-

sation. The first term of this formula comes from the Lorenz force acting on conductive electrons. The second term represents the anomalous effect contribution due to spontaneous magnetisation. R_0 depends mainly on the densities of carriers. However, R_s depends on the variety of material specific parameters [90]. From this formula, we can see that ρ_{xy} should increase linearly with the magnetic field as expected from the Lorentz force. However, in ferromagnets, typically ρ_{xy} initially increases steeply in weak magnetic fields and saturates at large values. Thus, the spontaneous magnetisation in ferromagnets affects the hall resistivity.

Antiferromagnets, unlike ferromagnets, possess a non-spontaneous $q = 0$ magnetisation as in a zero magnetic field, the total spin is compensated. Thus, according to the equation (5.2) we do not expect the AHE in antiferromagnets. However, experiments prove that it is possible to have an anomalous Hall effect in a noncollinear antiferromagnet with zero magnetisation.

In frustrated spin systems, we can observe the unconventional anomalous Hall effect (UAHE) which cannot be accounted for by conventional AHE mechanisms based on spin-orbit interaction to magnetisation M.

However, the observation of UAHE has been limited to only bulk materials with the three-dimensional analogue to the triangular lattice [91]. The UAHE has not been experimentally reported nor theoretically expected in a two-dimensional triangular lattice [92]. In this way, $PdCrO_2$ becomes a material of high interest and in the same way extremely challenging. Takatsu *et al* in Ref. [92] reported observation of what they interpreted as an unexpected UAHE in $PdCrO_2$ from a transport study of single crystals. They observed that ρ_{xy} deviates from the field–linear dependence and even changes its sign, although M increases linearly with H (fig. 5.7). This behaviour sharply contrasts with the empirical behaviour expressed by equation (5.2). They also compared the $PdCrO_2$ with non-magnetic $PdCoO_2$ in order to extract the effects of the frustrated spins. Figures 5.7 (a) and (b) represent the field dependence of Hall resistivity of $PdCrO_2$ and $PdCoO_2$. Above the Neel

temperature, both these compounds exhibit a linear field dependence of the Hall resistivity with a negative slope. Such behaviour of the Hall resistivity indicates the dominance of electron-like carriers. However, the most remarkable difference between these compounds should appear below the Neel temperature. As we can see from the data of Takatsu *et al*, with decreasing temperature below the Neel temperature, the slope rapidly changes. This unusual non-linear field dependence has a hump around 10–30 kOe emerges at temperatures below 20 K.

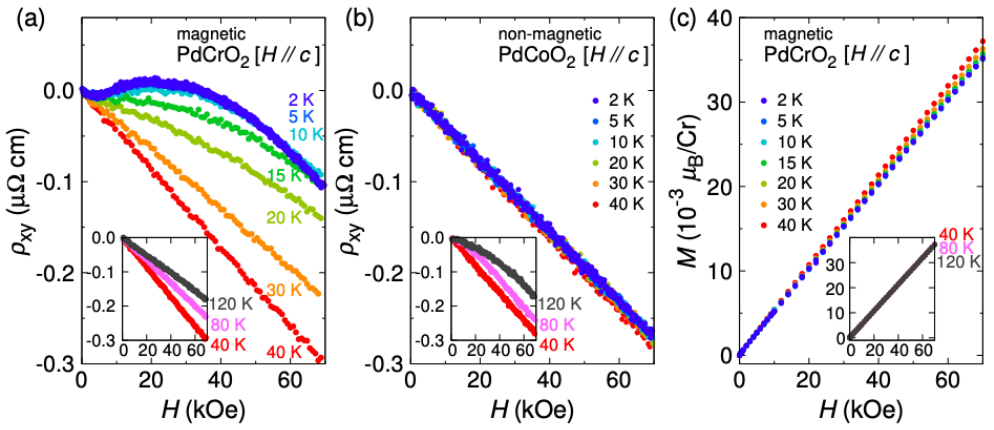

Figure 5.7: Field dependence of the Hall resistivity ρ_{xy} for (a) $PdCrO_2$ (T_N = 37.5 K) and for (b) non-magnetic $PdCoO_2$. (c) Field dependence of the magnetisation M for $PdCrO_2$. Figure from Takatsu et [92].

The theoretical understanding of UAHE in $PdCrO_2$ is a complicated problem. On the one hand, the conductivity is predominantly attributable to the Pd $4d^9$ electrons. However, at the same time, the field from Cr affects the Pd sites. The experimental data in [92] would be consistent with a non-coplanar magnetic structure of the Cr spins which would allow a finite scalar spin chirality in the presence of a magnetic field [93]. Whether one exists or not is still an open question.

All the experimental data discussed above were obtained in bulk single crystals. The geometrical uncertainty in an electronic transport experiment leads to more significant errors. Such issues could be crucial for the experi-

ment in extremely conductive materials. The microstructure procedure that I used in $PdCoO_2$ and $PtCoO_2$ (Section 3.2) can not only increase the accuracy of measurements. Restricting the crystal size (e.g. less than mean free path) can open new effects that we can not observe in bulk crystals. So far, no one has studied microstructures of $PdCrO_2$.

5.4 Is linear in temperature resistivity fundamental or strange?

As mentioned above in connection with Fig. 5.6, the resistivity of $PdCrO_2$ is remarkably linear in temperature between approximately 200 and 500 K. This raises further interesting questions about the physics of $PdCrO_2$.

The theory of conductivity, discussed in Section 2.1, was placed on a solid ground more than 60 years ago for the common metals. However, there are many materials whose transport properties are beyond the conventional paradigm. A well-known failure of text-books is 'strange metals' which have linear in temperature resistivity dependence well below the Debye temperature. In many compounds with linear in temperature resistivity, electrons seem to dissipate the energy as quickly as possible, as though they are bumping up against a fundamental quantum speed limit. In classical physics, there is no restriction concept of a time interval; it can be as short as you like. However, in quantum mechanics, there is an intrinsic time scale given by the temperature. The scattering rate per Kelvin in some systems is proportional to the ratio of two fundamental constants: the Planckian and Boltzmann constants (5.3). Intriguing indications for a minimum scattering time, or equivalently a maximum attainable scattering rate, are observed in systems diverse as laser-cooled atoms at 10^{-6} K and the quark-gluon plasma at 10^{12} K [94, 95]. Sitting near the middle of this range, strongly interacting electrons in solids can also be used to examine the concept of Planckian dissipation.

$$\frac{1}{\tau_P} \sim \frac{k_B T}{\hbar} \tag{5.3}$$

One finds the temperature dependence of the resistivity in 'strange metals' [73]:

$$\rho \sim \frac{m}{ne}\frac{k_B T}{\hbar} \tag{5.4}$$

The linear in temperature contribution to resistivity is consistent with the Drude formula (2.1) if the scattering rate is (5.3).

Remarkably, in many materials such as copper oxides, ruthenium oxides, iron pnictides, organic metals, and heavy-fermion compounds, the electrical resistivity is proportional to temperature precisely at a quantum critical point [96].

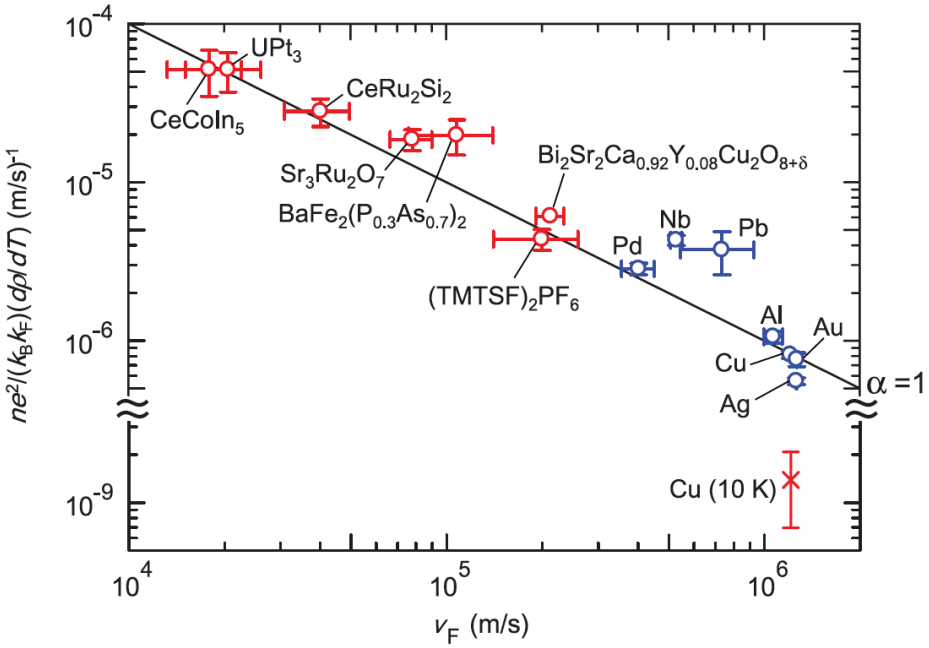

Figure 5.8: A wide range of metals in which the resistivity varies linearly with temperature have similar scattering rates per kelvin.Conventional metals for which T-linear resistivity is seen at high temperatures (blue symbols). The line marked $\alpha = 1$ corresponds to equation 5.3.Figure from Bruin *et al* [73]

Commonly quantum criticality is associated with the depression of energy scales toward zero temperature. Thus, the temperature becomes the only relevant energy scale. The natural question posed by this observation is whether linear in temperature behaviour is exclusive to quantum critical systems. Bruin *et al.* answered this question in Ref. [73]. They analysed the scattering rate per Kelvin in a wide variety of materials and summarised it in fig. 5.8. In addition to quantum critical systems, a different class of materials with linear in temperature resistivity shows the same dependence of the scattering rate (5.3).

5.4.1 Planckian scattering in conventional metals

Although the study of 'strange' metals associated with quantum criticality caused the current interest in Planckian dissipation, actually, it has a much longer history than that. In 1934 Peierls [97] noted that conventional metals such as Ag, Au, Cu, etc., have Planckian electrons at room temperature.

I showed in 2.1 that in materials in which phonon scattering dominates, electron-phonon processes in the high-temperature limit have a T-linear scattering rate that is conventionally expressed as equation 5.3. At high temperatures, phonon modes have a large wave vector q and relax electron momentum more effectively. The scattering of electrons, in this case, can be presented semiclassically as [98]:

$$\frac{1}{l} \sim nA \sim \frac{1}{a^3} < \Delta x^2 > \sim \frac{1}{a^3} \frac{k_B T}{K}, \tag{5.5}$$

where n is a density of scatters (phonons), A is a scattering cross section, Δx is the displacement of atom from equilibrium, a is lattice spacing and K is the atomic spring constant characterising energy that 'holds together' the crystal. For a large Fermi surface, $k_F \sim 1/a$, the inverse electronic lifetime, $1/\tau = v_F/l$, will be of order

$$\frac{1}{\tau} \sim \frac{D^2}{Ka^2 * E_F} \frac{k_B T}{\hbar}, \tag{5.6}$$

here D is the deformation potential, Ka^2 is the atomic binding energy. All lattice energy scales are eventually rooted in the electronic dynamics that hold the atoms together, thus, the deformation potential can be estimated $D \sim Ka^2 \sim E_F$, and it leads to the Planckian lifetime (5.3). It is important to note here that despite the short lifetime τ_P, the mean free path l is long: $l = v_F\tau \sim aE_F/\hbar * \hbar/k_BT = a * E_F/k_BT >> a$. This happens because the Fermi velocity is large. The electrons encounter many collisions per time because they move quickly. This is a difference with unconventional Planckian metals discussed in Ref. [73] with short mean free path and small velocities [99].

The above estimates suggest Planckian transport due to electron-phonon scattering above the system-dependent characteristic temperature, the Debye temperature. In contrast, quantum criticality has links with Planckian transport below this temperature. Even a low Debye temperature can not explain observed T-linear scattering down to zero temperature [100]. Therefore, it is possible that in unconventional metals, both mechanisms are present in different ranges of temperatures [101]. The fact that several different mechanisms lead to the Planckian dissipation in different temperature ranges highlights a potential universality that transcends microscopic detail.

5.4.2 Planckian bound and uncertainty principle

In the Boltzmann theory, the electrons are treated semiclassically. An electron is assumed to move with a wave vector k between scattering by phonons, electrons, defects, or some other disorder. For a Boltzmann description of transport, superposition of the single-particle Bloch states should form localised wavepackets. To get an electron quasiparticle with mean free path l and wavevector k_F the superposition should be formed with uncertainties in position $\Delta x \leq l$ and wavevector $\Delta k \leq k_F$. Thus, according to the uncertainty principle, $l \geq 1/k_F$. This expression is one version of the Mott-Ioffe-Regel limit. The Mott-Ioffe-Regel limit describes a minimum metallic conductivity compatible with a minimum mean free path, l, which equals the interatomic spacing a. In a semiclassical picture, it is natural that l cannot be much

smaller than interatomic space, a, since at that point, the concept of quasiparticle motion vanishes. However, a semiclassical theory itself breaks down when $l \sim a$ because the uncertainty in the k vector of an electron is comparable to the size of the Brillouin zone $\Delta k \leq 1/a$, which leads to $l \geq a$, so it is not clear whether this condition is one that dictates physical observation or the range of validity of a particular type of theory [102, 98].

As I showed in Section 2.1 the finite quasiparticle lifetime due to elastic scattering from the disorder at $T = 0$ is responsible for the residual resistivity of metals. However, it certainly violates the Planckian bound because $1/\tau_p \to 0$ as $T \to 0$. Thus, it is reasonable to suggest that the Planckian bound is intrinsically associated with an inelastic scattering that is capable of redistributing energy between particles and thermalising the system.

Inelastic scattering transfers energy between the single-particle eigenstates given by superpositions of Bloch states on some inelastic timescale τ_{in}. However, this scattering leads to a width ΔE in the single-particle energy. With the scattering rate $1/\tau_{in} \geq k_B T/\hbar$ the uncertainty principle gives $\Delta E \geq k_B T$ [98]. Therefore, the uncertainty in the single-particle energy is greater than the width of the Fermi-Dirac distribution. Thus, a Boltzmann description in terms of single-particle states requires $\tau_{in} \leq \tau_P$. Seen from this point of view, the Planckian bound is about the ability of quasiparticles to retain their existence in the face of inelastic many-body scattering [99].

5.4.3 Universal theory?

An experimental fact that an analysis procedure applied to an extensive range of materials in [73] consistently reveals a Planckian scattering rate suggests that this averaged timescale might actually have an intrinsic meaning [103]. The T-linear resistivity is observed in tuned quantum critical systems at low temperatures, in some cases down to below 100 mK. However, the same behaviour is seen up to almost 1000 K in conventional metals and some cuprates, implying that the linear law and quasi-universal scattering rate are independent of the microscopic details of the scattering.

5.4 Is linear in temperature resistivity fundamental or strange?

To estimate a timescale using the Drude approach (2.1), we require measurements of the resistivity ρ, effective mass m_* and density n. The complicated parameter is the effective mass as it can vary around the Fermi surface and between different sheets. The resistivity measurements could be challenging, however, in principle, relatively straightforward. Density can be estimated from the quantum oscillations as the frequency of the oscillations depends on the cross-sectional area of the Fermi surface [104]. The hall coefficient also can be used to determine the density, however, it is sensitive details of the scattering around the Fermi surface, and therefore a less reliable than quantum oscillations [105].

There are two commonly used ways to estimate the effective mass: quantum oscillations and the specific heat measurements. The specific heat also depends on the density of states at the Fermi surface. The amplitude of quantum oscillations depends on the cyclotron mass [104]. Quantum oscillations can separate the contributions from different Fermi sheets. This is important if the carriers in the heavy sheet do not contribute significantly to transport but can dominate the specific heat. In this case, the estimation of the effective mass for use in the Drude expression by specific heat is incorrect. Thus, the effective mass m_{*i} and densities n_i of each sheet of the Fermi surface can be determined by and used to define a timescale [73]:

$$\frac{1}{\tau} = \frac{e^2}{\sigma} \sum \frac{n_i}{m_{*i}}, \tag{5.7}$$

where σ is the conductivity. The heavy sheets of the Fermi surface in this expression give the suppressed contribution to the scattering rate.

However, the amplitude of quantum oscillations decays exponentially with temperature and with the effective mass [104]. Therefore, the values of the mass and density used in the Drude analysis in Ref. [73] are deduced from a low-temperature Fermi liquid-like regime where resistivity has T^2 dependence. The Dynamical Mean Field Theory (DMFT) studies of correlated Hubbard model-like systems also showed a strong temperature dependence of the effective mass in the T-linear region [106, 107]. This theory implies

the origin of the linear in T behaviour at low temperatures to be the electron-electron inelastic scattering.

The nature of the charge transport in the T-linear regime and the meaning of timescales extracted from resistivity should be understood better, as there are unusual temperature dependences of many quantities.

Thus, the Planckian dissipation problem brings up two main questions: why is it observed in a wide range of materials with different microscopies, and why does in the same material the Planckian rate exist in a wide temperature range. If the origin of the Planckian rate at low temperatures is electron-electron scattering according to the MFL theory and phonon scattering at high temperatures, the traditional transport theory discussed in Section 2.1 does not give the same gradient of the linear dependence. The fact that the same gradient is seen suggests the existence of a minimal equilibration time in the system. If this statement is correct, Matthiessen's rule discussed in Section 2.1 should be obeyed in the T-linear region. However, it is difficult to test in a controlled way, and the question has not been fully settled based on comparison of many different compounds. Preferably, a very precise experiment is required during which the residual resistivity of the material is increased in a controlled manner, and the results of the Planckian dissipation are compared before and after. One of the experimental targets of my research on $PdCrO_2$ was to perform such an experiment.

Chapter 6

Experimental results of the magnetic delafossite metal $PdCrO_2$ and discussion

As described in the review of its physical properties in Chapter 5, there is considerable motivation to perform transport measurements on well-defined structures and microstructures of $PdCrO_2$. Creating the devices on which to perform the experiments proved to be much more difficult than for $PdCoO_2$ and $PtCoO_2$, and became one of the main technical challenges that I had to overcome, as described in section 6.1. In the remainder of the chapter I will describe the transport and magneto-transport experiments that successful fabrication of working microstructures enabled.

6.1 New method of fabricating free-standing microstructures

Our group's standard procedures for making microstructures are not applicable for crystals with massive thermal expansion or contraction because of the substantial mechanical coupling between the insulating substrate and the metallic crystal. Because of this, microstructured crystals of $PdCrO_2$ mounted as described above break during cool down, when the temperature approaches the Neel temperature. Thus I developed a new free-standing microstructure method.

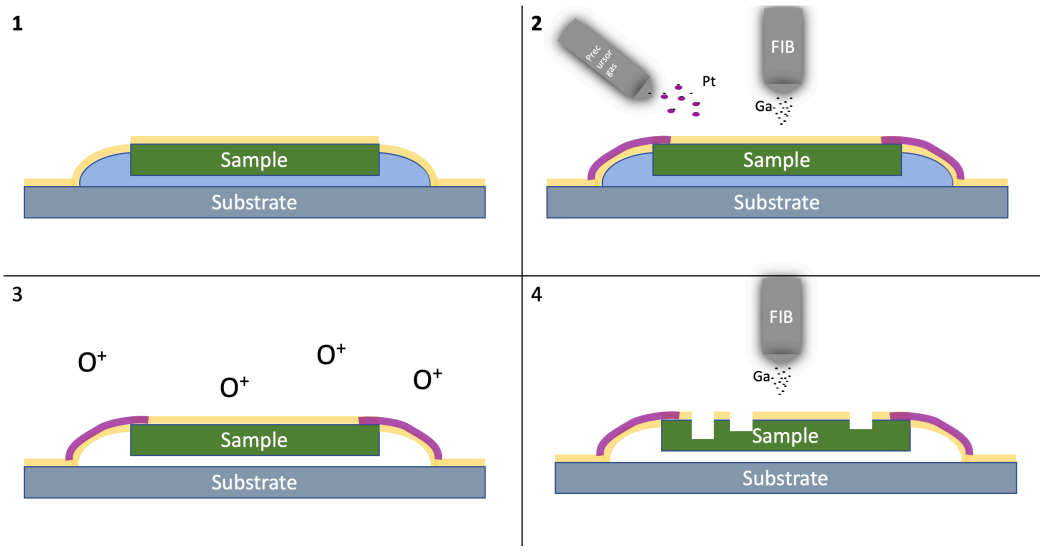

Figure 6.1: Schematic main steps of structuring a free-standing device

This method is mainly based on the Pt deposition FIB tool. A sketch of the following steps is shown in fig. 6.1. The first step in this method is the same as in Chapter 3. As-grown crystals are mounted on a drop of two-component glue on a pre-cleaned sapphire substrate. (In the irradiation experiment, to decrease the thickness of the substrate, we used cleaved mica as a substrate) Crystals are mounted in the glue by hand with the help of kapton micro-tools. Then, 200 nm of gold with a 5 nm sticking Ti layer is sputtered on the substrate with the crystal. The 2-component glue creates

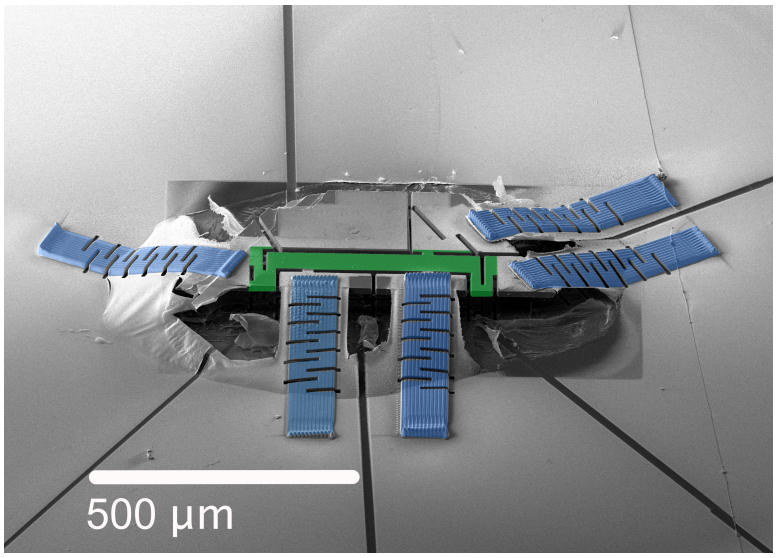

Figure 6.2: Electron image of free-standing microstructure of $PdCrO_2$ sample. Pt contacts are blue, green is the device.

very smooth contacts to the delafossite crystal. To decouple the crystal from the sapphire substrate is necessary to create a 'bridge' that will hold the crystal. Pt leads deposited by FIB on top of the glue will play the role of the 'bridge'. These leads should connect the crystal surface with the substrate. The thickness of Pt should be the same as or higher than the thickness of the crystal. We then sputter the second layer of gold to decrease the contact resistance of the device. Then the gold layer from the top of the glue drop should be removed using the FIB. The next step is to remove the glue drop using the oxygen plasma cleaner. The crystal, held by the deposited Pt leads, will remain. After these steps, the sample can be sculpted in a final device by the FIB. To further reduce the mechanical stress, it is also possible to make meanders on the Pt contacts. This geometry decouples the crystal from a substrate, and the sample is floating and held by the Pt leads. An example of one of my free-standing microstructures, made using this method, is shown in fig. 6.2. The Pt contacts with the meanders are shown in blue in this figure. The 'effective part' of the device is coloured in green.

6.2 Investigation of the Planckian dissipation in $PdCrO_2$ by high energy electron irradiation

The T-linear resistivity dependence of $PdCrO_2$ is experimentally observed in the temperature range 200 – 500 K, with the upper limit that of the measurement that was performed, not necessarily that of the T-linear behaviour [76]. The Debye temperature is approximately 340 K, as deduced from heat capacity measurements [11]. The textbook theory discussed in 2.1 suggests that resistivity should drop with temperature as T^5 far below the Debye temperature. From now on, I will analyse the temperature ranges lower than 300 K for technical experimental reasons - the fabrication of the microstructures means that it is dangerous to heat them to substantially above room temperature. The in-plane resistivity of $PdCoO_2$ is substantially nonlinear between 100 and 300 K (fig. 6.3), a feature attributed to prominent optical phonons. The magnetic component of the resistivity can be found by subtracting the resistivity of $PdCoO_2$ from that of $PdCrO_2$. The magnetic contribution to resistivity is expected to saturate when the Cr spins become completely uncorrelated. Fig. 6.3 shows the difference in temperature behaviours of $PdCoO_2$ and $PdCrO_2$. The magnetic component of resistivity increases at temperatures an order of magnitude greater than the Neel temperature.

$PdCrO_2$ brings further surprises in transport measurements. I calculated the scattering rate from the resistivity between 200 K and 300 K using the formula 2.1. The Fermi surface, effective mass and density of electrons are well known for $PdCrO_2$ [82, 76, 5]. Above the Neel temperature, the Fermi surface of $PdCrO_2$ is almost identical to that of nonmagnetic $PdCoO_2$. The bulk Fermi surface consists of a single hexagonal electron pocket attributed to one Pd 4d conduction electron per unit cell. However, for resistivity calculations, we can approximate the shape of the Fermi surface quite well to a circle because v_F and k_F are very weakly varying. The scattering rate per kelvin

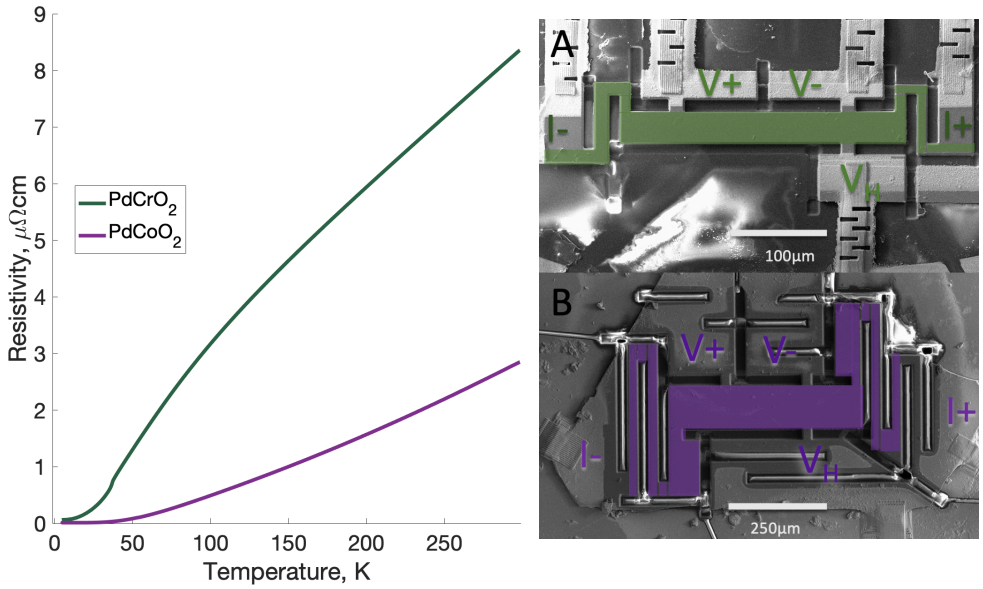

Figure 6.3: Left: Temperature dependence of the resistivity of $PdCrO_2$ green, and $PdCoO_2$ purple. Right: A) SEM image of $PdCrO_2$ microstructure, B) SEM image of $PdCoO_2$ microstructure

for $PdCrO_2$ in the temperature range 200 – 300 K can therefore be estimated with confidence and, surprisingly, it satisfies equation (5.3). Some unusual mechanism should exist in $PdCrO_2$ that changes the resistivity behaviour from $PdCoO_2$ one and forces electrons to have the Planckian scattering rate. Finding and understanding the physics of this mechanism in $PdCrO_2$ will be a small step towards resolving the Planckian dissipation problem. One of the ways to it is studying the scattering mechanisms that are varying significantly between the different Planckian materials. Understanding the microscopic scattering will answer the critical question: whether Planckian dissipation is associated with thermalisation, which demands the microscopic scattering to be inelastic. Thus, it motivates a study of Matthiessen's rule: is it obeyed in a Planckian compound? The easy experiment, which comes to mind first, is comparing the scattering rates in crystals of different qualities. However, the scattering centres might have a completely different nature in crystals for which the reason for the difference in quality is unknown, i.e. it

is then impossible to tell for sure if the scattering is inelastic and if it can be considered independent from the elastic one. The ideal method of studying Matthiessen's rule is introducing point-like defects into a compound in a controlled way. The irradiation by high energy electrons (Section 3.5) can provide a unique opportunity for this experiment. The light accelerated electrons have energy just enough for displacing one atom without creating a cascade reaction, thereby creating a vacancy and interstitial, i.e. a Frenkel pair. Thus, the temperature dependence of resistivity before and after high energy electron irradiation shows if Matthiessen's rule is obeyed. For this purpose, I performed a high energy 2.5 MeV electron irradiation experiment in $PdCrO_2$.

The irradiation by electrons with a maximum kinetic energy of 2.5 MeV was performed at the SIRIUS Pelletron linear accelerator operated by the Laboratoire des Solides Irradi´es (LSI) at the Ecole Polytechnique in Palaiseau, France (Section 3.5). The single crystals of $PdCrO_2$ were mounted using the free-standing microstructure method (Section 6.1).

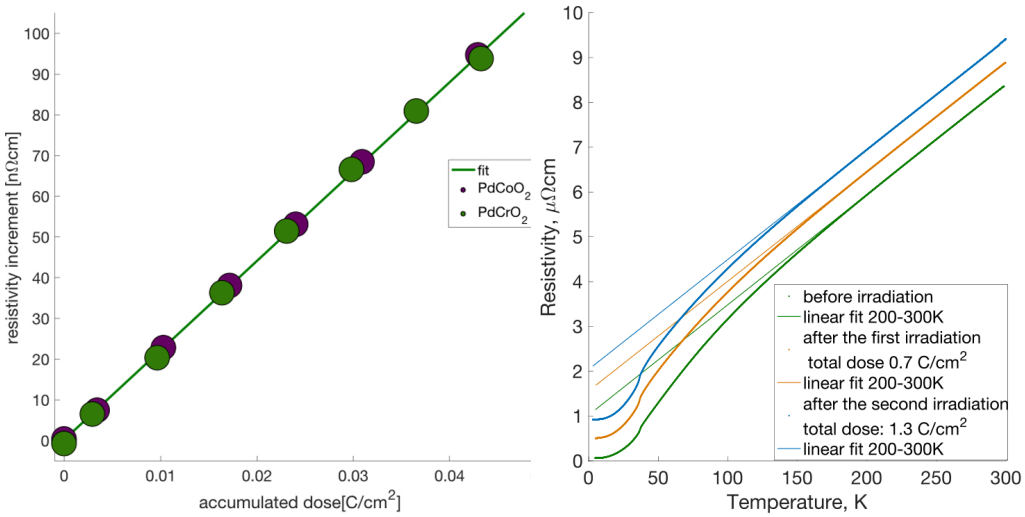

Figure 6.4: Left: Increase of resistivity as a function of electron dose for two delafossite metals: $PdCoO_2$, $PdCrO_2$, measured in situ at a temperature of 22 K. Right: Temperature dependence of $PdCrO_2$ resistivity with linear fir between 200 and 300 K for different doses.

6.2 Investigation of the Planckian dissipation in $PdCrO_2$ by high energy electron irradiation

The increase of the resistivity of $PdCoO_2$, and $PdCrO_2$ as a function of electron dose is shown in the left panel of fig. 6.4. Because the resistivity increases as a function of electron dose, I can conclude that electron irradiation introduces defects and that those defects contribute to resistivity. In these two compounds, the dependence of resistivity on dose is linear and has the same slope in the investigated range. Changing Pd to Pt in $PtCoO_2$ also results in a linear increase of resistivity, but with a higher gradient [36]. Taken together the observations indicate that the resistivity is dominated by defects in the conductive Pd or Pt planes, as expected in such two-dimensional systems. A high energy electron displaces a Pd atom in a conducting layer creating an interstitial and a vacancy, i.e. a Frenkel pair. The more rapid increase of resistivity with dose in $PtCoO_2$ is naturally explained by it presenting a higher scattering cross-section to the incoming electrons due to its higher atomic number. A given dose therefore creates more defects.

Calculations show that the most stable interstitial structure is for the interstitial atom (Pd) to bond to two O in the layer above, resulting in significant in-plane displacements of two Pd atoms. The bond lengths between the interstitial and the two oxygen atoms are not equal, while one of the nearby Pd is more displaced from its original site than the other. The bond lengths between the displaced Pd and the nearest two Pd atoms are similar. I can interpret it as a structure finding the balance by attempting to form equilibrium length bonds with the two O atoms above and the two Pd atoms below. Both the vacancy and the interstitial therefore present highly localised scattering centers to the conduction electrons.

It is often implicitly assumed that the various contributions to resistivity are additive, obeying Matthiessen rule 2.1. As emphasised above, in this case it was important not to accept that assumption, but to test it in a controlled manner. Measuring the transport properties of a single sample before and after electron irradiation offers a unique opportunity to do this. However, measurements of the sample before and after irradiation can become challenging. First of all, as we warm up the sample from the irradiation

temperature of 22 K, the defects become more mobile and may recombine, eliminating any added resistivity. Fortunately, in $PdCrO_2$ recombination probability is substantially less than 1. The added resistivity does decrease during the initial warm-up to room temperature but only to approximately 65% of its original value.

In the right panel of fig. 6.4 I show the temperature dependence of the resistivity of the $PdCrO_2$ with different electron doses. It is essential to specify that before and after electron irradiation experimental data was obtained from the same microstructure. Thus, I reduced the uncertainty of the experiment associated with different contact configuration and different original quality of the samples. The temperature dependence of resistivity remains nearly unchanged, with the defects adding an approximately temperature-independent offset, indicating a good agreement with Matthiessen's rule between 200 K and 300 K. The linear fit between 200 K and 300 K for all the doses has the same gradient within experimental error, proving that adding elastic scattering centres into the material does not change the scattering rate per Kelvin. Thus, I can conclude that, as Matthiessen's rule is obeyed in this range of temperatures, the inelastic scattering can indeed be considered independent from the elastic scattering, as postulated in equation 2.14. As Matthiessen's rule is obeyed, it adds to the evidence that inelastic processes are the key thing in Planckian dissipation.

6.3 Irradiation and the Hall effect signal

Even though creating defects in CrO_2 does not influence the temperature dependence of the in-plane transport properties in zero applied magnetic field, I was interested in investigating whether it would have an effect on the Hall voltage, particularly on the aspect of the behaviour previously attributed to the unconventional anomalous Hall effect (UAHE) reported in ref. [92] and reviewed in Section 5.3 above. Electron irradiation results might influence the UAHE from two sides: creating disorder in the conductive layer and in

the magnetic structure. To investigate it, I also performed magnetisation measurements of the $PdCrO_2$ single crystal before and after electron irradiation. This crystal was passively irradiated (no electrical contacts) and received a total dose of electron irradiation of around 0.7 C/cm^2. Thus, I can compare the magnetisation and Hall effect before and after electron irradiation in two crystals irradiated to the same electron dose.

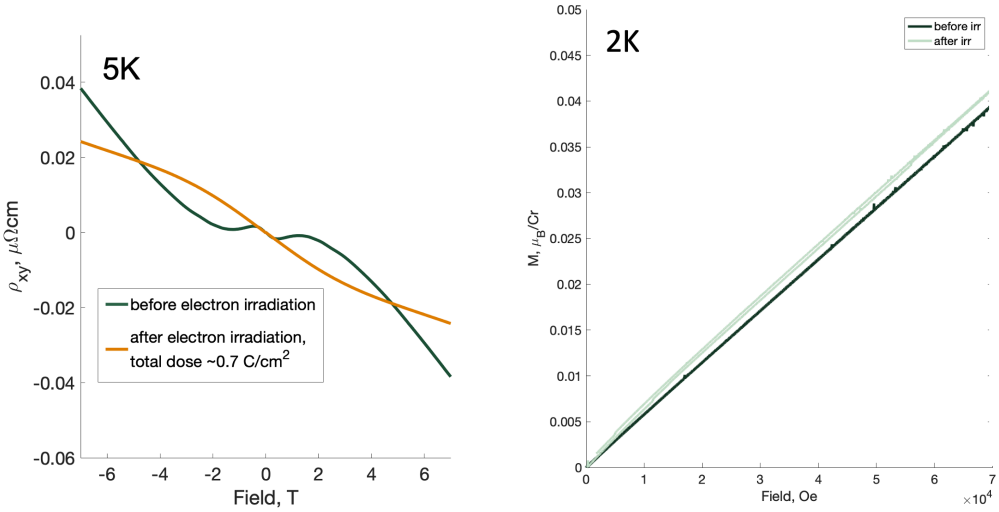

Figure 6.5: Left panel: the influence of electron irradiation on the field dependence of ρ_{xy} in $PdCrO_2$ at 5 K. Right panel: magnetisation of $PdCrO_2$ before and after electron irradiation at 2 K

In the left panel of fig. 6.5 the field dependence of ρ_{xy} at 5 K before and after electron irradiation is presented.The shape of the ρ_{xy} curve before irradiation is very similar to that reported for bulk single crystals in Ref. [92]. Surprisingly, the Hall data post-irradiation are very strongly altered, and this large change is not correlated with a similar change in magnetisation. As shown in the right panel of fig. 6.5, the magnetisation remains linear in field and is not changed dramatically. In a collaboration with Veronika Sunko and Philippa McGuinness, our combination of data on $PtCoO_2$, $PdCoO_2$ and $PdCrO_2$ was used, in combination with measurements at varying accelerator voltage, to calculate the absolute cross-section for the Pd in $PdCrO_2$ under electron irradiation. I therefore know that the defect density in these samples

after heating to room temperature is around 0.16%.

The magnetic structure of $PdCrO_2$ hardly can be changed by introducing such a small number of defects; however, this amount of disorder changes the behaviour of ρ_{xy}. The most remarkable feature of the proposed UAHE in $PdCrO_2$, changing the sign of the ρ_{xy} at around 3 T, disappears after electron irradiation. The overall behaviour of ρ_{xy} becomes more linear Thus, I can assume that the origin of the UAHE behaviour lies not only in the non-collinear antiferromagnetic layer. This unique experiment is only the first small step towards understanding the UAHE problem in $PdCrO_2$, which requires further experimental and theoretical development. Moreover, high energy electron irradiation can provide a novel opportunity for this experiment.

6.4 Ballistic or hydrodynamic in $PdCrO_2$?

6.4.1 Can we apply hydrodynamic theory to metals?

There has been considerable progress in understanding unconventional electron transport in micro-scale systems in the last two decades. The Fermi liquid theory provides a framework that introduces an electron fluid by considering the interactions between the electrons. Then the following question is can we apply a classical hydrodynamic description to the electrons in metals?

A classical hydrodynamic theory is only precise at length scales much larger than the inter-particle separation. In a fluid, the hydrodynamic theory exists on a scale where conservation laws can be applied to derive the equations of motion and define macroscopic observables. If one considers viscosity, the conserved quantity is momentum. However, electron transport is conventionally determined by the momentum-relaxing scattering processes and the hydrodynamic observables, therefore, are mostly irrelevant to the electron transport in a solid.

Electron transport is conventionally determined by the momentum-relaxing scattering of electrons and described semiclassically. If the momentum-re-

laxing mean free path is much smaller than any of the other characteristic lengths of the system, it is in the regime in which Ohm's law holds. Electron-defect scattering degrades momentum, and electron-phonon scattering degrades both the energy and momentum of the electron fluid, and therefore, neither energy nor momentum is a long-lived conserved quantity for electron transport. Transport resembles the viscous behaviour when the mean free path of collisions that do not transfer momentum to the lattice, i.e. the momentum conserving mean free path, l_{MC}, is smaller than the momentum relaxing mean free path, l_{MR} (e.g. with static defects and phonons) [108].

In most cases, the momentum conserving scattering is assumed to be electron-electron with $\tau_{MC} = \tau_{ee}$ ($l_{MC} = l_{ee}$) [109, 108, 110]. Impurities and phonons in a metal play the environment's role, providing unwanted scattering from the point of view of hydrodynamics. Momentum relaxation in metals happens through electron-defect scattering, both normal and umklapp electron-phonon scattering and umklapp electron-electron scattering. However, the probability of electron-phonon umklapp scattering decreases with decreasing the temperature, slowing momentum relaxation. On the other hand, with decreasing temperature, the rate of conserving momentum electron-electron normal collisions drops as the ratio T^2/T_F as described by Fermi liquid theory in Section 2.1.

Under the special circumstances of phonon drag, however, electron-phonon normal scattering conserves momentum. In the normal electron-phonon scattering process, the phonon distribution is assumed to be in local equilibrium. An applied electric field or temperature gradient can drive the phonon distribution out of equilibrium in a real metal. In this situation, a current carrying electron will drag the phonons along, and hence, no overall momentum relaxation is caused by the normal electron-phonon collisions [111].

In metals, the electron-phonon umklapp processes discussed in Section 2.1 exhibit an exponential suppression $e^{-T_U/T}$ with decreasing the temperature. Normal processes can be substantial enough to outweigh the rate of losing momentum to the lattice with a very low impurity concentration at

sufficiently low temperatures. Thus, the existence of phonon drag, where the phonons are dragged out of the equilibrium by current carrying electrons, can in principle support a momentum-conserving electron-phonon fluid if impurity scattering can be ignored [111]. Therefore, it is essential to have a low impurity concentration as a benchmark of the host material to observe hydrodynamic electron flow.

6.4.2 $PdCrO_2$ results

A long-standing question in the physics of solids is whether this regime in which the viscosity of the electron fluid has an observable effect on the measured resistivity is experimentally accessible or not.

There are theoretical proposals of phonon drag in $PdCrO_2$ below the Neel temperature [112]. Having very similar properties to that of $PdCoO_2$, $PdCrO_2$ is a therefore candidate for searching for the hydrodynamic regime. However, it introduces several complications to the unconventional transport problem. The first one is a strong coupling between the magnetic and conductive layers. The second one is that unlike $PdCoO_2$, $PdCrO_2$ has multiple Fermi surfaces below the Neel temperature.

My experimental studies in $PtCoO_2$ and $PdCoO_2$ (Chapter 4) show the significance of understanding ballistic effects in these systems. Unfortunately, we can not tune the transport regimes here to be purely ballistic or purely hydrodynamic. Thus, to understand the whole picture of unconventional transport, it is necessary firstly to investigate the ballistic-diffusive crossover. To perform a thorough comparison between the transport properties of the two materials, I performed systematic thinning down studies in a $PdCrO_2$ microstructure.

The ballistic experiment in $PtCoO_2$ (Section 4.2) showed that the orientation of the device according to the Fermi surface is vital in such experiments. Thus, I created two $PdCrO_2$ microstructures using the free-standing method (6.1) shown in fig. 6.6. I aligned the first bar (fig. 6.6 A and B) according to the high temperature Fermi surface, as shown in the picture. The two sides

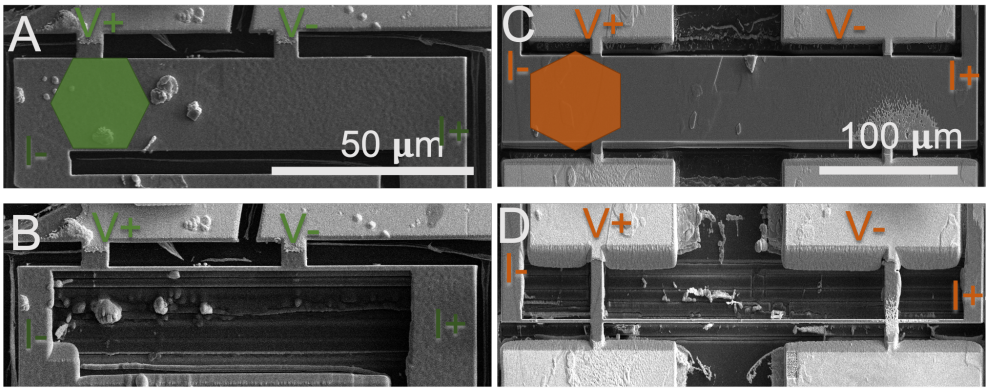

Figure 6.6: SEM images of the $PdCrO_2$ devices. A: initial bar oriented as 'hard' according to the high temperature Fermi surface. Its measured width is 22 μm. B: final size of the bar after several thinning down steps. Its measured width is 1 μm. C: initial bar oriented as 'easy' to the high temperature Fermi surface. Its measured width is 28 μm. D: final size of the bar after several thinning down steps. Its measured width is 1.4 μm

of the Fermi surface are parallel to the sides of the bar. This arrangement is called the 'hard' direction, as electrons have two priority directions towards the sample's edges. The second configuration is called 'easy', and it is 90 degrees rotated with respect to the 'hard' direction. Electrons have a priority direction along the bar (fig. 6.6 C and D).

The initial width of the 'hard' bar was 22 μm. The average low-temperature transport mean free path in the crystals I have studied of $PdCrO_2$, derived from the resistivity at 3 K, is around 2 μm. Because the initial width of the device is more than ten times larger than the expected mean free path, it seems reasonable to assume that electronic transport is ohmic at all temperatures. However, the value varies between each crystal due to differences in the concentration and form of growth defects and impurities. In the Ohmic regime, for material with resistivity ρ, the transport mean free path (l) for 2D metal can be calculated using the standard 2D expression:

$$\rho^{-1} = \frac{e^2}{hd} k_F l, \tag{6.1}$$

where h is Planck's constant, e the electronic charge and d the interlayer spacing.

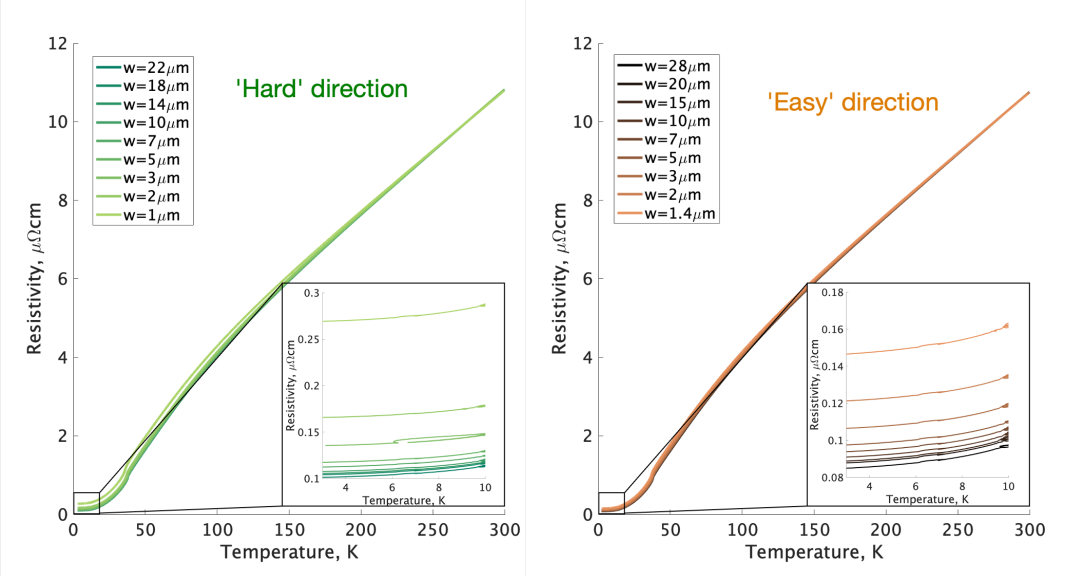

Figure 6.7: Temperature dependence of the resistivity of $PdCrO_2$ for several widths of the bars in two different orientations of the resistivity bar according to the Fermi surface: left figure - 'hard' direction, right figure - 'easy' direction.

The mean free path of the electrons in a 'hard' direction device at the temperature 3 K calculated using this method is around 1.7 μm and for 'easy' direction this value is around 2 μm. The mean free path is the value that would occur in the same crystal but within a bulk device, defined as when the boundary scattering does not significantly contribute to the resistance and the transport behaviour within the Ohmic regime. I performed these measurements for the following widths of the 'hard' channel: 22 μm, 18 μm, 14 μm, 10 μm, 7 μm, 5 μm, 3 μm, 2 μm and 1 μm. The channel oriented in the 'easy' direction had 28 μm, 20 μm, 15 μm, 10 μm, 7 μm, 5 μm, 3 μm, 2 μm, 1.4 μm widths.

The temperature dependence of the resistivity for all the widths of the 'hard' direction channel is shown in the left panel of the fig. 6.7. The value of the resistivity at high temperatures, where the mean free path is relatively

small, is close for all the channels. The influence of the boundaries becomes significant at low temperatures the mean free path becomes longer, boundary scattering plays an important role, and the as resistivity increases. I observed a similar qualitative behaviour of the resistivity in the channel oriented in the 'easy' direction, the right panel in the fig. 6.7.

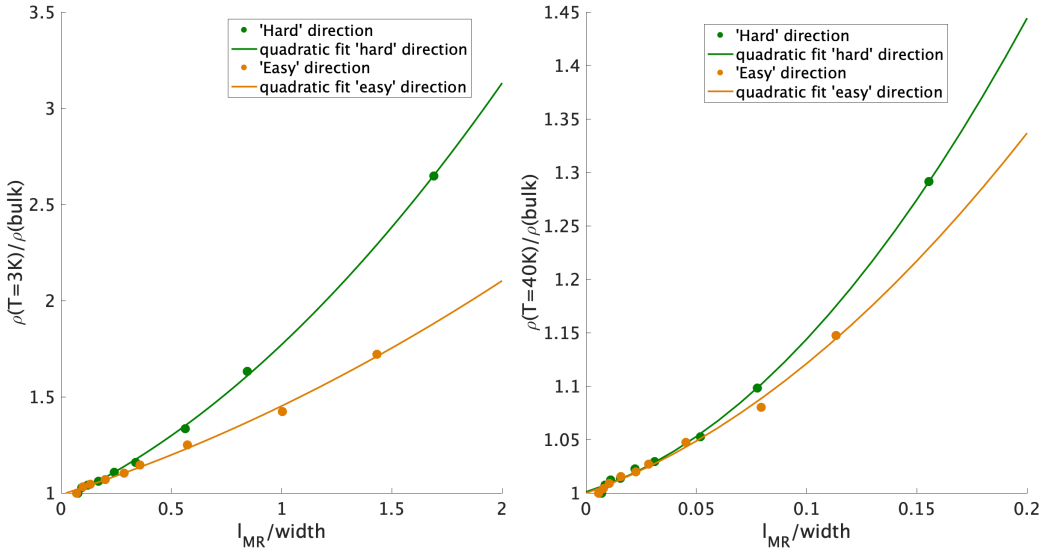

Figure 6.8: The increase of the resistivity normalised by the bulk resistivity against the ratio of the momentum relaxing mean free path to the width of the channel, left panel: at 3 K, right panel: at 40 K.

To analyse the influence of the boundaries and the effect of the mean free path, I plotted the increase of the resistivity at 3 K in 'easy' and 'hard' orientations of the channels normalised by their ohmic values against the ratio of the momentum relaxing mean free path to the width of the channel in the left panel of fig. 6.8. As in $PdCoO_2$, the influence of the boundary scattering becomes significant when the mean free path of the electrons becomes comparable with the width of the channel. As seen in the left panel of fig. 6.8 the resistivity increases strongly as a function of decreasing width for both orientations of the Fermi surface. The orientation of the channel according to the Fermi surface influences this dependence. There is a big difference in the resistivity behaviour in 'easy' and 'hard' channels. Unfortunately, the

relatively small mean free path of $PdCrO_2$ does not allow us to investigate the influence of the width of the channel on resistivity for values of l_{MR}/w much higher than one. However, the quadratic fit of the obtained data predicts a continued rise of the difference between 'easy' and 'hard' directions with increase of the l_{MR}/w value.

The simplest theoretical model that explains constricted geometries and boundary scattering, by Nordheim [48] assumes that Matthiessen's rule is valid for the combination of the resistivity in a wide channel ρ_{bulk} and the extra resistivity due to the boundary scattering in a narrow wire ρ_{bound}, leading to a total resistivity ρ:

$$\frac{\rho}{\rho_{bulk}} = 1 + \frac{l}{w}, \tag{6.2}$$

where l is the mean free path in a wide sample where boundary scattering is unimportant and w is the diameter of the wire. However, this model assumes fully diffuse boundary scattering. A more complicated model by Fuchs [49], was based on the Boltzmann equation and also accounted for possibilities of non-diffuse boundary scattering. The models described above assumed a circular Fermi surface in the 2D approximation appropriate to $PdCrO_2$ and that any scattering was isotropic, with an equal relaxation time around the Fermi surface. However, in Ref. [113] Bachmann *et al.* showed the influence of directional ballistic effects on transport properties of $PdCoO_2$. They also performed the kinetic calculations for a perfectly hexagonal Fermi surface that explained the experimental results.

In the Gurzhi regime of Ref. [108] with a circular Fermi surface, the low-temperature channel resistance increases monotonically as the inverse square of the channel width and should be direction independent. However, in Ref. [114] Cook *et al.* found via numerical solutions of the Boltzmann equation with a polygonal Fermi surface a substantial modification of the Gurzhi effect. According to their model the low-temperature resistivity behaviour in $PdCrO_2$ is closer to the hydrodynamic behaviour because of the quadratic contributions seen in the data of Fig. 6.8. However, this interpre-

tation has to be treated with considerable care, because the quadratic behaviour is seen at such low temperatures. The Fermi temperature of $PdCrO_2$ is around 27000 K. The inelastic Coulomb lifetime τ_{ee} of 2D a quasiparticle near to the Fermi surface:

$$\frac{1}{\tau_{ee}} = -\frac{k_B}{h} T_F (\frac{T}{T_F})^2 ln(\frac{T}{T_F}), \tag{6.3}$$

As the hydrodynamic regime is reached when electron-electron scattering events dominate momentum relaxing scattering events, at temperatures of 5 K in $PdCrO_2$, electron-electron scattering should be negligible, even in a polygonal Fermi liquid. If phonon drag were the source of momentum--conserving scattering, a strong T^{-5} dependence of the channel resistance is predicted at low temperatures, due to the temperature dependence of the viscosity [115, 116], I observe no sign of such a rise. It is therefore unlikely that this unconventional w scaling of the conductance results from a standard, temperature-dependent viscosity.

The data also give direct evidence that the fragmentation of the large Fermi surface into many small ones below the Neel temperature does not have a strong influence on the orientation dependence of the data, as expected since the gaps are very small and hence have very little effect on the unfolded Fermi surface. As is seen in the right panel of Fig. 6.8, the data above the Neel transition show the same qualitative trends as those at 3.5 K).

The above discussion shows that although the quadratic dependence of the resistivity is often considered the character of the viscous contribution of electron flow into the electron transport, it is premature to definitely conclude that there is a large hydrodynamic contribution in the case of delafossite metals. It will be important, however, to find an alternative explanation for the quadratic width dependence of the channel resistance that I have observed. Even if it is due to ballistic physics, that ballistic behaviour in $PdCrO_2$ persists far outside the point where the mean free path and width of the channel are equal, possibly due to the non-circular Fermi surface.

One of the methods used to identify viscous effects in graphene and in

semiconductors to investigate the influence of the viscosity of electrons and its relationship to ballistic effects is to measure the dependence of the resistivity on the number density of electrons and compare the results with theory [117, 118, 119, 120]. Unfortunately, in the case of delafossite metals, it is impossible to tune the system by changing the number of density of electrons because they are high carrier density metals in which gating could make only tiny relative changes to the carrier concentration.

The experiment on $PdCrO_2$ discussed in this section shows the importance of understanding ballistic effects and the difficulty in distinguishing the hydrodynamic effects from ballistic ones. The evidence suggests that the viscous effects do not play a major role in causing the observed behaviour. Although the unconventional electronic transport in $PdCrO_2$ may not be a result of hydrodynamics, the effect that anisotropy of the Fermi surface has on a ballistic-diffusive crossover is highlighted as an open issue. My experimental data set therefore provides an outstanding opportunity for further theoretical investigation of unconventional transport in the magnetic delafossite metal.

6.5 Magnetoresistance of the magnetic delafossite metal

The initial goal of my project was to study Planckian dissipation and the ballistic-diffusive cross-over in $PdCrO_2$. The successful creation of the novel method of free-standing microstructures broadens the experimental opportunities of studying electron transport in $PdCrO_2$. $PdCrO_2$ gives a novel opportunity to study the natural heterostructure of two completely different limiting states of electrons: free-electrons and Mott-insulator. Thus, it is crucial to study the influence of the Mott-insulator on the conductive layer in a magnetic field. I therefore set out to perform a systematic set of magnetotransport measurements on $PdCrO_2$, to form a dataset suitable for direct comparisons with those non-magnetic PdCoO2, in which the CoO_2 layers

can be thought of as band insulators.

The magnetoresistance $\Delta\rho_{ab}(\mathrm{H})/\rho_0(\rho_0 = \rho_{ab}(\mathrm{H}=0))$ of a microstructure of $PdCoO_2$ for temperatures from 5 K to 300 K is shown in the right panel of fig. 6.9. At all temperatures, the scale of the MR is small, never exceeding 30% at 9 T. In the framework of the nearly free electron model, ($PdCoO_2$ has a single band FS with an effective mass close to the free electron mass) at low fields such that $\omega_c\tau << 1$, the MR varies as the lowest even power of the magnetic field, B^2, owing to its symmetry under magnetic field reversal. At very high fields where $\omega_c\tau >> 1$, in a closed FS, the electrons tend to make many revolutions around the FS before getting scattered by impurities or a phonon, and the magnetoresistance is predicted to saturate. However, the saturation of $PdCoO_2$ magnetoresistivity at high field is not observed up to the highest field, where $\omega_c\tau$ is around 30. The behaviour of magnetoresistance at 5 K is noticeably different from that reported in ref. [32] due to long-range ballistic effects discussed in Section 4.4 and [65, 66]. The width of the device is around 90 μm, which with a mean free path of 20 μm can cause the ballistic behaviour at low temperatures. The $PdCoO_2$ device studied in Ref. [32] was 155 μm wide, so any residual ballistic effects were smaller. $PdCoO_2$ is a single band metal, and thus within the Drude theory of a single-band material with only one microscopic length scale, the magnetoresistance should vanish. As discussed in Ref. [32] two distinct scales can explain the presence of magnetoresistance in $PdCoO_2$, the magnetoresistance is non-zero and related to their difference, while the resistivity in the zero field will depend on some weighted average of the two. In metals with low rates of momentum relaxing scattering, more exotic contributions beyond standard Boltzmann transport in the relaxation time approximation can play a role in transport properties [32]. In $PdCoO_2$, however, these effects are all quite small, and there is little in the overall pattern of the magnetoresistance that is strongly different from the expectations for a high purity single-band metal.

The magnetoresistivity of $PdCrO_2$ $\Delta\rho_{ab}(\mathrm{H})/\rho_0(\rho_0 = \rho_{ab}(\mathrm{H}=0))$, in contrast to that of $PdCoO_2$, exhibits a very strong field dependence below the

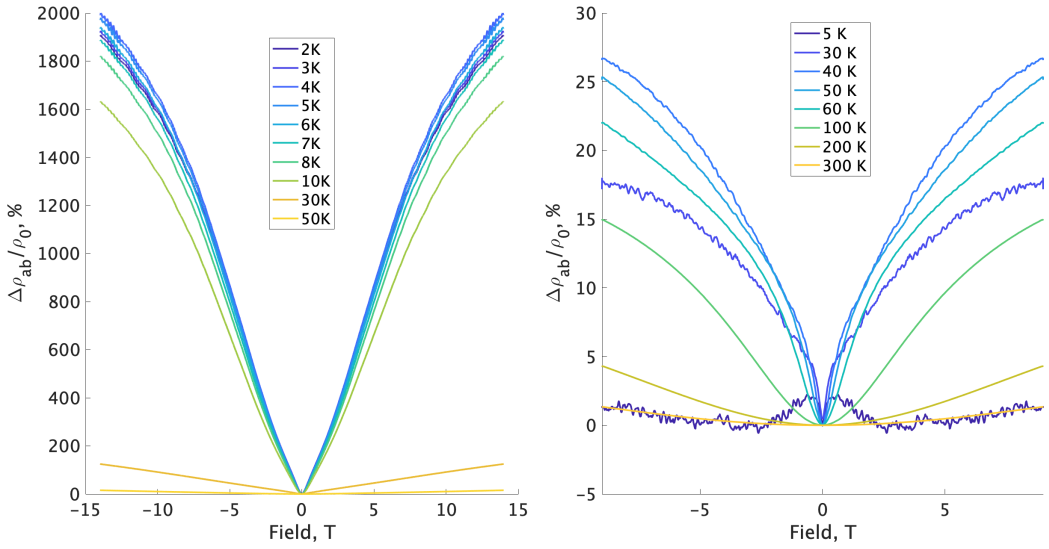

Figure 6.9: Left panel: Magnetic field dependence of the in-plane resistivity of $PdCrO_2$ in the temperature range from 2 K to 50 K in the field up to B = 14 T perpendicular to the ab-plane. Right panel: Magnetic field dependence of the in-plane resistivity of $PdCoO_2$ in the temperature range from 5 K to 300 K in the field up to B = 9 T perpendicular to the ab-plane.

Neel temperature (left panel in fig. 6.9). At the temperature 2 K the magnetoresistance reaches 2000% under 14 T magnetic field for the transverse geometry (H⊥I). Large magnetoresistance for a transverse geometry can often be attributed to a large Lorenz force due to multiple conduction bands. However, this large contribution from the Lorentz force should be suppressed for the longitudinal geometry when H ∥ I [121]. Thus, in a non-magnetic system, the magnetoresistance in transverse and longitudinal geometries should drastically differ, and the maximum longitudinal magnetoresistance is expected to be less than 100% [122]. In Ref. [84] Ok *et al.* measured both longitudinal and transverse magnetoresistance of $PdCrO_2$. The large longitudinal magnetoresistance is comparable with the transverse one, which indicates coupling between itinerant electrons and the Cr spins.

In this experiment, I obtained the value of magnetoresistance under a 14 T magnetic field almost five times larger than was ever reported [84, 123].

This extremely high value of magnetoresistance indicates the high purity of the single crystal of $PdCrO_2$ and also the significance of microstructures in the resistivity measurements.

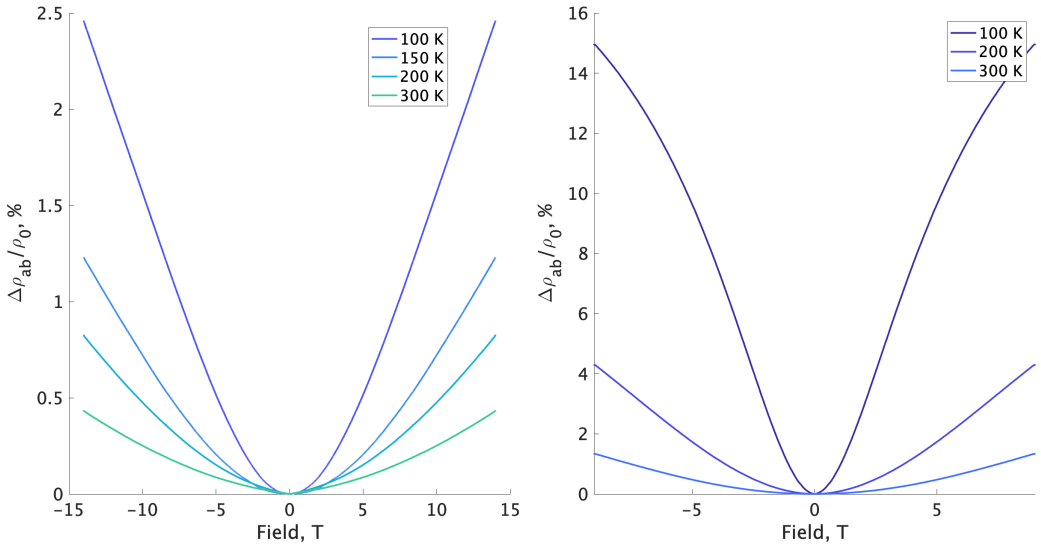

Figure 6.10: Left panel: Magnetic field dependence of the in-plane resistivity of $PdCrO_2$ in the temperature range from 100 K to 300 K in the field up to B = 14 T perpendicular to the ab-plane. Right panel: Magnetic field dependence of the in-plane resistivity of $PdCoO_2$ in the temperature range from 100 K to 300 K in the field up to B = 9 T perpendicular to the ab-plane.

Above the Neel temperature, the Fermi surfaces of $PdCrO_2$ and $PdCoO_2$ are similar. However, the resistivity of $PdCrO_2$ in the magnetic field is higher than that of $PdCoO_2$, presumably due to the magnetic scattering. To compare the behaviour of these two compounds in magnetic fields, I plotted the magnetoresistivity of the $PdCrO_2$ at temperatures 100, 150, 200, 300 K in the left panel of fig. 6.10 and that of the $PdCoO_2$ at 100, 200, 300 K in the right panel of fig. 6.10. Both compounds have the magnetoresistivity value much lower at these temperatures. However, the absolute value of magnetoresistivity of $PdCoO_2$ is larger than that of $PdCrO_2$ at the same temperatures. This high temperature magnetoresistance looks conventional in form in both compoounds, and the smaller scale in $PdCrO_2$ is qualitatively consistent with

its shorter mean free path.

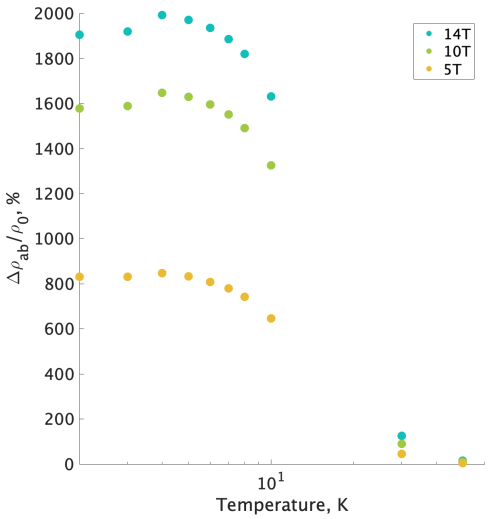

Figure 6.11: Temperature dependence of the magnetoresistance of $PdCrO_2$ under 5 T, 10 T and 14 T magnetic field

This discussion suggests that the very large magnetoresistance in $PdCrO_2$ may be associated with the development of magnetic order. However, the relationship is not trivial. One of the surprises that $PdCrO_2$ brings in these studies is the temperature dependence of the magnetoresistance shown in fig. 6.11. It shows a rather strong drop in value that onsets at temperatures higher than 10 K, far below the Neel temperature.

The unusual behaviour of magnetoresistance occurs at low temperatures. The value of magnetoresistance in the magnetic field of 14 T reaches its maximum around 4 K. The same behaviour is observed at 10 T. With decreasing magnetic field, this effect weakens. At a magnetic field of 5 T, the value of magnetoresistance is almost constant between 2 K and 5 K.

Below the Neel temperature, electrons in a conductive Pd layer feel an additional periodic potential of the CrO_2 layer, due to magnetic order, and the band structure is reconstructed [76, 82]. The gaps (ϵ_g) opened at the antiferromagnetic Brillouin zone boundary are small, on the order of 40 meV [84]. For the reconstructed Fermi surface (fig. 5.4), the coexistence of the

electron-like γ and the hole-like α pockets should induce a strong magnetic field dependence of the resistivity. However, in a larger magnetic field, there is a probability for the electrons to tunnel through the gap (ϵ_g) in k space from one part of the Fermi surface to another with sufficient cyclotron energy [104]. This can occur at high magnetic fields, known as magnetic breakdown. The criterion for magnetic break down is that the separation ($\hbar\omega_c$, where ω_c is a cyclotron frequency) between Landau levels should become comparable to or greater than the energy gap (ϵ_g):

$$\hbar\omega_c \geq \frac{\epsilon_g^2}{E_F}, \tag{6.4}$$

The probability for the magnetic breakdown is described by:

$$p = exp(B_0/B), \tag{6.5}$$

where B_0 is the breakdown field.

For the $PdCrO_2$ energy gap of 40 meV the breakdown field B_0 is around 6.9 T. As the magnetic breakdown occurs above this value, a contribution from the nonmagnetic Fermi surface (δ in fig. 5.4) becomes more dominant, which should cause the saturation of the magnetoresistance. However, the expected behaviour is not observed in the experiment. In addition, the existence of the temperature dependence of the breakdown probability p and energy gap ϵ_g can not explain the unusual temperature behaviour of the magnetoresistance shown in fig. 6.11.

This is all consistent with the above discussion about longitudinal magnetoresistance: there is no evidence that the very large low temperature magnetoresistance of $PdCrO_2$ has an origin in conventional orbital effects. The data therefore provide another opportunity for in-depth theoretical work.

6.5.1 Magnetoresistance of the magnetic delafossite metal in a restricted geometry

In the mesoscopic regime, the transport in delafossites is no longer isotropic in the ab-plane, unlike in the bulk where the triangular in-plane lattice has high enough symmetry that isotropy is enforced in the transport. In zero magnetic field in both $PdCrO_2$ and $PdCoO_2$ in the mesoscopic regime, the boundary scattering and low symmetry of the Fermi surface play a significant role in electron transport. However, the experiment discussed above (Section 6.5) showed that $PdCrO_2$ has dramatically different behaviour in magnetic field from that of $PdCoO_2$ due to the exotic coupling happening between Mott-insulating layers and conducting layers. The main issue I will discuss in this section is how the boundary scattering in the mesoscopic regime influences the unusual magnetotransport in $PdCrO_2$.

The magnetoresistance of $PdCoO_2$ in the mesoscopic regime was well measured and discussed in [47]. For the accurate comparison of two mesoscopic regimes under a magnetic field of the Mott-insulator and band-insulator heterostructures, I performed magnetotransport measurements for the two $PdCrO_2$ samples, with 'easy' and 'hard' Fermi surface orientations according to the channel, discussed in the Section 6.4.

At mesoscopic widths in $PdCoO_2$, a peak in the MR is observed in fig. 6.12 A. A precursor of the ballistic peak starts appearing in the magnetoresistance at a width three times larger than the mean free path, which with decreasing channel width dramatically increases. However, the ballistic behaviour is not observed in the magnetoresistance of $PdCrO_2$ (fig. 6.12 C and E).

In $PdCoO_2$ at 2 K, the peak in ρ_{xx}/ρ_{bulk} in fig. 6.12B appears at the exact value of w/r_c around 1 for every channel width, which is a clear manifestation of ballistic behaviour that is dictated solely by boundary scattering. However, ρ_{xx}/ρ_{bulk} in $PdCrO_2$ in fig. 6.12 D and F does not have the ballistic peak even for the lowest w/l_{MR} value. At the same time, at zero magnetic fields, the resistivity of the $PdCrO_2$ increases with decreasing the width of the channel, apparently due to the boundary scattering. And when w/r_c reaches 1 the

6.5 Magnetoresistance of the magnetic delafossite metal

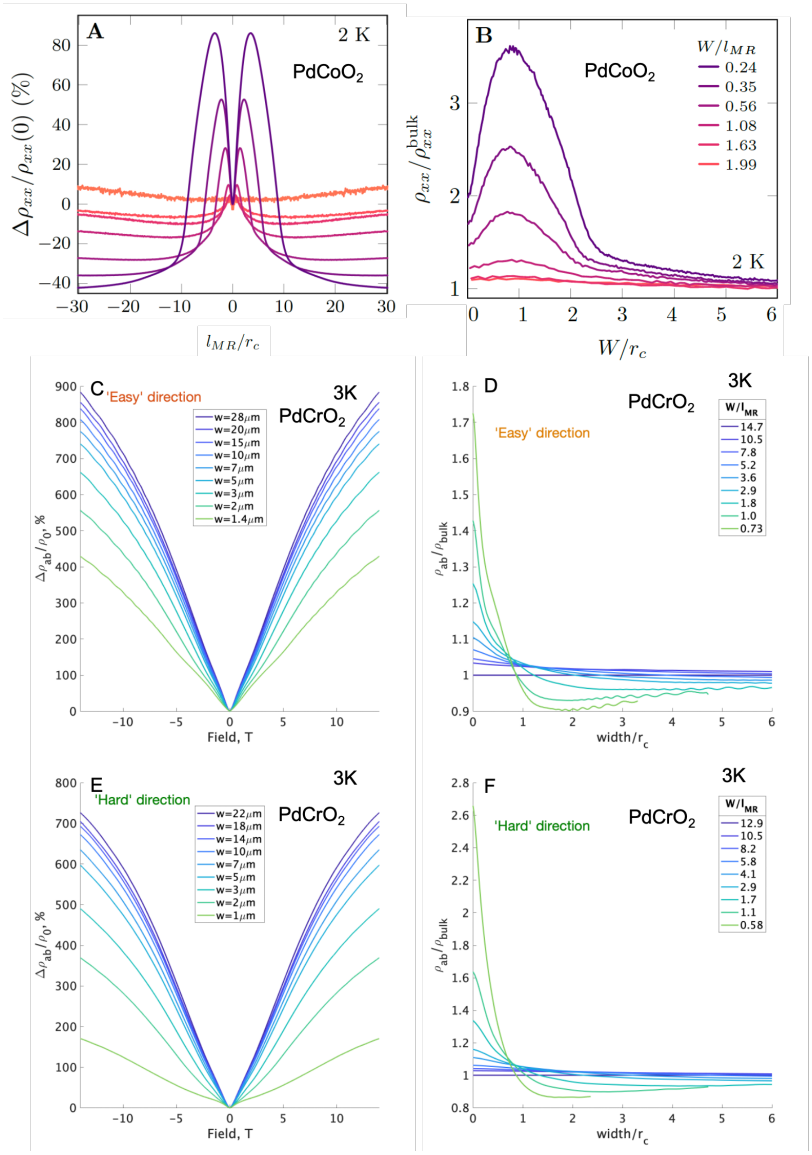

Figure 6.12: A: $PdCoO_2$ magnetoresistance at 2 K against the ration of the mean free path to r_c. Reproduced from [47]. B: bulk normalised resistivity as a function of the ration of the width to the cyclotron radius at different values of w/l_{MR}. Reproduced from [47]. C: magnetoresistivity measured in $PdCrO_2$ at 3 K for the 'easy' orientation of the Fermi surface. D: the dependence of the ratio of ρ_{ab}/ρ_{bulk} of $PdCrO_2$ at 3 K for 'easy' direction of the Fermi surface orientation on w/r_c for several values of w/l_{MR}, E and F: the same for the 'hard' orientation of the Fermi surface

ρ_{xx}/ρ_{bulk} actually drops below the diffusive limit (fig. 6.12 D and F).

My experimental data shows the unexpected behaviour of $PdCrO_2$ in the ballistic regime in the magnetic field. The direct comparison of band insulator and Mott-insulator heterostructures proves that the exotic interlayer coupling in $PdCrO_2$ causes unexpected physics. However, the origin of this is not clear so far. My experimental results provide a unique data set for future theoretical developments.

6.5.2 SdH effect in the magnetic delafossite metal

On close examination, I noticed the oscillations of magnetoresistance obtained from the bulk free-standing microstructure of $PdCrO_2$ (fig. 6.9A), which is presumably the Shubnikov-de Haas effect. Shubnikov and de Haas first observed oscillations in the field dependence of the electrical resistivity in 1930 [104]. This discovery led to the discovery of the de Haas-van Alphen oscillations in magnetic properties. Magnetic quantum oscillations became a powerful tool for studying electronic dispersion and Fermi surface geometry.

In an external magnetic field H, the only permitted states of an electron in k-space are so-called Landau levels (fig. 6.13 A). In a simple case of the free electron gas with spherical Fermi surface, the Landau levels are circular cylinders with a common axis in the direction of the magnetic field H. As the magnetic field is increased, the tube expands and varnishes infinitely rapidly when the tube reaches the size of the Fermi surface. The passing and vanishing of smaller tubes through the Fermi surface happens at equal intervals of $1/H$. Thus, the degeneracy and even (at constant chemical potential) particle number oscillate with period $1/H$ which depends on the size of the underlying Fermi surface:

$$\Delta\frac{1}{H} = \frac{2\pi e}{\hbar A}, \tag{6.6}$$

where A is extremal cross-section of the Fermi surface in the plane perpendicular to the applied magnetic field.

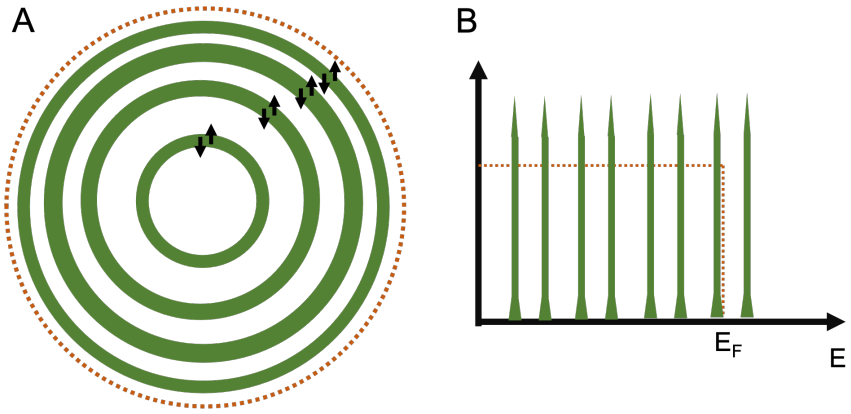

Figure 6.13: A: Schematic sketches of Landau tubes for a circular Fermi surface B: Spikes represent the Landau-quantised quasiparticle density of states

This oscillation transfers to the density of states (fig. 6.13B), so it also affects electrical transport. However, the theory of the SdH effect is more complicated than that of the dHvA effect, as it involves the problem of electron scattering in a magnetic field. In 1965 Pippard showed that the probability of scattering is proportional to the number of states into which the electron can be scattered. This probability determines the relaxation time and the resistivity of a metal oscillates with the oscillation of the electron density of states at the Fermi energy. However, the SdH effect is not easy to observe.

At finite temperatures thermal broadening of the Fermi function means that Landau levels no longer depopulate individually in the way sketched in fig. 6.13B. The thermal damping factor R_T has the form:

$$R_T = \frac{X}{sinhX}, \tag{6.7}$$

with X:

$$X = \frac{2\pi^2 r m^* k_B T}{e\hbar B}, \tag{6.8}$$

Here, m^* is the 'cyclotron effective mass'. Thus, studying the temperature

dependence of the oscillation amplitude gives information about the effective mass of the electrons. This construction is called a Lifshitz-Kosevich formula.

In the presence of disorder, the spikes in the density of states in fig. 6.13 B will be washed out in accordance with the uncertainty principle. The impurity damping factor R_D is conventionally expressed in terms of an 'equivalent impurity temperature' the Dingle temperature T_D, as defined the expression:

$$R_D = exp(\frac{-2\pi^2 r m^* k_B T_D}{e\hbar B}), \tag{6.9}$$

Here r is the order of the harmonics, T_D is the Dingle temperature and m^* is cyclotron effective mass from the analysis of the R_T damping factor.

Thus, the total damping will be a combination of disorder and temperature [104]. However, as discussed above, delafossite metals are extremely pure systems. Thus, the observation of the SdH effect is possible in these metals.

The second derivative of the magnetoresistance of $PdCrO_2$ for different temperatures shown in fig. 6.14 exhibits oscillatory behaviour periodic in $1/H$. For a more detailed analysis of the quantum oscillations of the resistivity, I performed a fast Fourier transform (FFT) presented in fig. 6.15 A and B for the two field regions: 3 – 6 T and 7 – 10 T. This analysis gives two frequencies of the quantum oscillation: around 102 T and 830 T. Four dHvA frequencies were measured in [76]: 0.83 kT for the α pocket, 3.45 kT for the β (breakdown orbit), 10.52 kT for the γ pocket and 27.40 kT for the δ pocket (breakdown orbit) (see fig. 5.4). The frequency of 810 T that I observed in magnetoresistivity is close to the 0.83 kT frequency of the α pocket. However, in the dHvA experiment, the frequency of 102 T was not observed.

The Fermi surface of layered metals is a warped cylinder. Such a Fermi surface can have two close extremal cross-section areas A_1 and A_2 by the planes in k-space perpendicular to magnetic field H, which give two relative quantum oscillations frequencies according to the equation (6.6). The observed magnetic quantum oscillations are given by the sum of oscillations

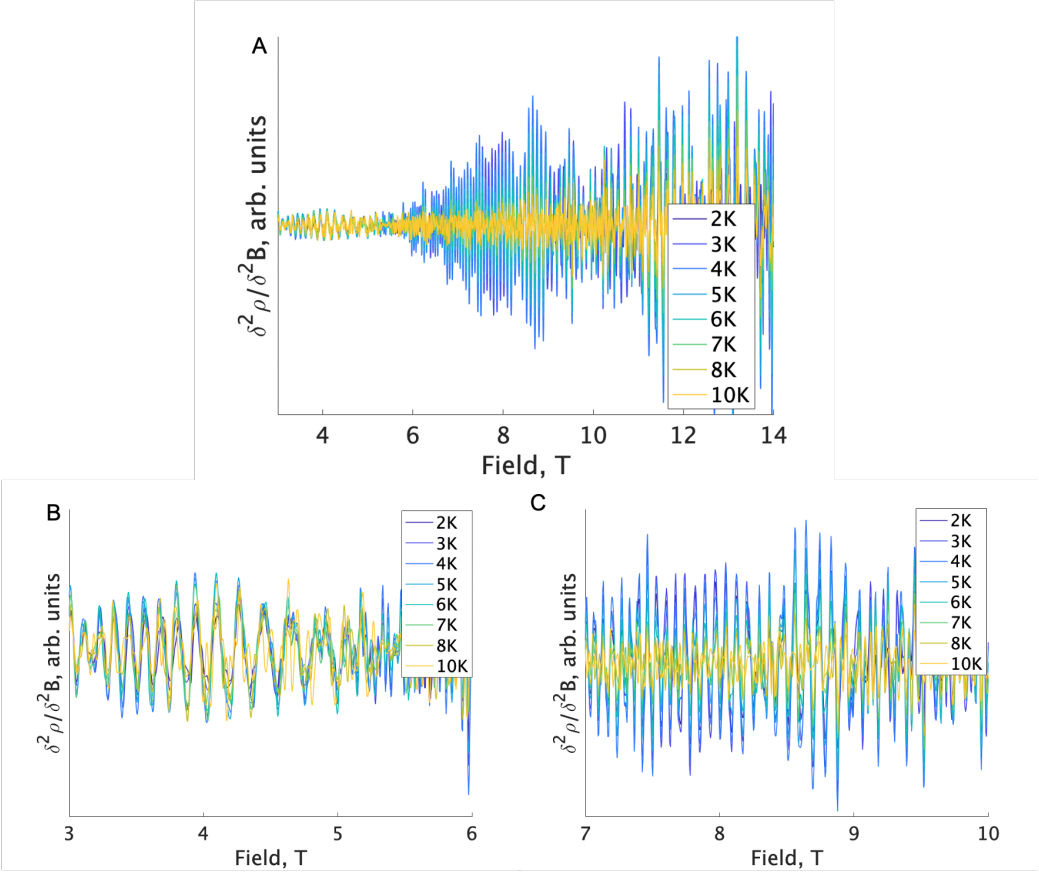

Figure 6.14: A: the second derivative of magnetoresistivity of $PdCrO_2$ in the temperature range from 2 K to 10 K. B: the first type of oscillations at the second derivative of magnetoresistivity of $PdCrO_2$ at temperature range from 2 K to 10 K, magnetic fields from 2 T to 5 T. C: the second type of oscillations at the second derivative of magnetoresistivity of $PdCrO_2$ at temperature range from 2 K to 10 K, magnetic fields from 11 T to 14 T.

with these two frequencies, which gives the beats of an amplitude, typical to quasi-two-dimensional metals with the frequency of $\Delta F = F_1$ - F_2. Another feature of electron transport in magnetic field in quasi 2D metals is the so--called slow oscillations which come from the mixing of two close frequencies F_1 and F_2 and have the frequency equal to the doubled beat frequency [124].

However, $PdCrO_2$ does not give two close enough frequencies to cause the oscillations with frequency of 102 T. Furthermore, these quantum oscillations exist at low fields below $\sim$ 6 T. To try to understand the origin of these

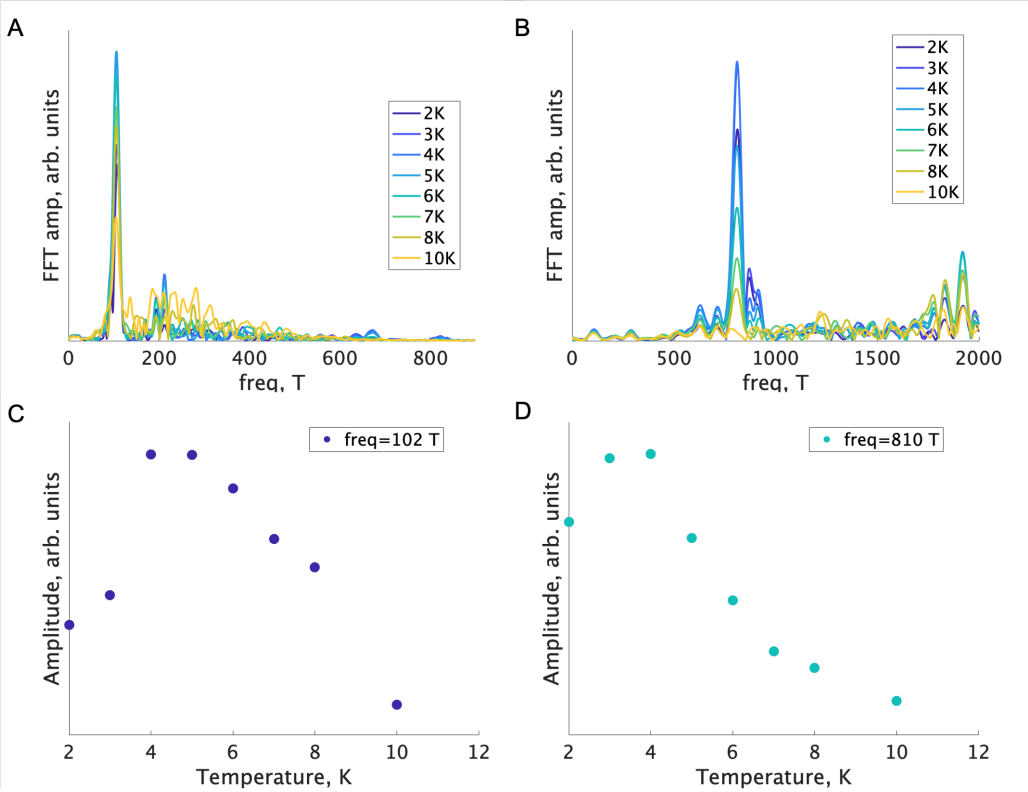

Figure 6.15: A: FFT of the second derivative of $PdCrO_2$ magnetoresistivity from 3 T to 6 T. B: FFT of the second derivative of $PdCrO_2$ magnetoresistivity from 7 T to 10 T. C: temperatures dependence of the FFT peak amplitude with 102 T frequency. D: temperatures dependence of the FFT peak amplitude with 810 T frequency.

quantum oscillations, I performed measurements at different temperatures from 2 to 10 K, to calculate the effective mass according to the Lifshitz-Kosevich formula (6.7). The temperature dependence of the amplitude of both oscillations shown in fig. 6.15 C and D is the second surprise that $PdCrO_2$ brings in these measurements. The temperature dependences have apparent peaks at $\sim$ 4 K. According to the Lifshitz-Kosevich formula, the amplitude of the quantum oscillations should decrease with increasing the temperature. Thus, the calculation of the effective mass from the SdH effect is questionable. In contrast to my SdH data, the amplitudes of dHvA measurements in [76] are well fitted using the LK expression and the anomalous behaviour

is only seen in SdH measurements. This may suggest that the strange behaviour of $PdCrO_2$ arises only from specific conduction channels, which do not significantly contribute to the dHvA measurements.

The deviation between SdH and dHvA can arise due to the difficulty in disentangling the contributions to the conductivity from the different Fermi surface sheets. The explanation of the SdH effect is based on the assumption that $\delta\rho/\rho$ is proportional to the density of states. Thus, the temperature dependence is well described by the Lifshitz-Kosevich formula. However, for multiband systems, the situation can be more complicated due to the different contributions to the conductivity from each band, and this effect will not influence the dHvA results [104].

In some charge transfer salts [125, 126] anomalous quantum oscillations, whose SdH amplitudes deviated from conventional behaviour, were explained by metallic edge states. These systems have highly conducting quasi-two-dimensional planes. The deviation between SdH and dHvA in these materials is explained within a simple model based on spin damping effects due to the interaction of the conduction electrons with the weak magnetic moments in the sample and the presence of the strong correlation between the induced average magnetisation and an anomalous behaviour of the quantum oscillations of the resistivity and magnetisation.

However, $PdCrO_2$ has a complex, layered structure. Thus, unfortunately, it is difficult unequivocally to explain the anomalous behaviour of quantum oscillations that I observed in $PdCrO_2$. However, the magnetoresistance already hints at some unconventional physics, so it will be interesting to see if a unified picture can be developed in which the quantum oscillations are also explained.

6.6 Conclusions

In conclusion, in this chapter, I explored the transport properties of the magnetic delafossite metal $PdCrO_2$. To overcome the technical challenges, I

developed a new method of fabricating microstructures discussed in Section 6.1 and successfully implemented it in $PdCrO_2$ microstructures.

$PdCrO_2$ obeys Planckian scattering in a wide range of temperatures between 200 - 500 K, whilst this behaviour is not observed in the sister compound $PdCoO_2$. To understand the origin of this behaviour, I performed a high energy irradiation experiment in $PdCrO_2$. The results of this experiment discussed in Section 6.2 prove that Planckian dissipation depends only on inelastic scattering events, which also agrees with theoretical discussion in Section 5.4.

During this high energy electron experiment, I also studied the influence of the point-like defects on unconventional anomalous Hall effect (UAHE) in $PdCrO_2$. This is the first measurement of the influence of the defects on UAHE shown in Section 6.3. The change of the UAHE with adding point-like defects is dramatic.

The new method of microstructure fabrication also allowed to study unconventional transport regimes in $PdCrO_2$. This material was a suitable candidate for searching a hydrodynamic transport alongside with $PdCoO_2$, however, the thinning down experiment that I performed in the $PdCrO_2$ microstructure devices discussed in Section 6.4 indicates that the increase of the resistivity originates from ballistic behaviour rather than hydrodynamic behaviour. However, the behaviour of the $PdCrO_2$ thinned down microstructures in the magnetic field is significantly different from that of $PdCoO_2$. Thus, it is premature to conclude the purely ballistic effects as the origin of unconventional behaviour of $PdCrO_2$.

The magnetoresistance measurements of $PdCrO_2$ microstructures showed unexpected results. The Shubnikov de Haas effect (SdH) observed in Section 6.5.2 exhibits an unusual temperature dependence that does not obey the Lifshitz-Kosevich expression. Unfortunately, it is impossible to explain the anomalous behaviour of $PdCrO_2$ due to its complex, layered structure. However, my experimental results provide a foundation for future theoretical developments.

Chapter 7

Conclusions and outlook

In conclusion, in the first part of my thesis, I explored the electronic transport of non-magnetic delafossite metals $PtCoO_2$ and $PdCoO_2$ on the scale of the mean free path. These materials have metallic carrier densities, quasi-2D transport and a hexagonal Fermi surface. This is unique set of properties within ultrapure materials, making them ideal for testing many assumptions regarding transport within ultraclean materials.

I have explored transport in non-magnetic delafossite materials within the ballistic regime when the device geometry is on the scale of the mean free path. Measuring the transport within square-shaped junctions and long bars of $PtCoO_2$ demonstrated a novel resistance anisotropy, which only exists within the ballistic regime and is attributable to the non-circular Fermi surface. I explored the origin of this anisotropy by a defect introduction study performed using high energy electron irradiation. The impact of these defects on transport in unconventional regimes proved that the observed transport anisotropy stems from the non-circular Fermi surface of $PtCoO_2$ and symmetry lowering by device shape. Our studies of non-irradiated $PtCoO_2$ junctions have shown that ballistic effects remain present at a square size over 15 times larger than the mean free path. The high energy electron irradiation experiment, which changed the electron mean free path, confirmed two distinct decay regimes. For the first time, these studies show that ballistic behaviour

in the delafossite metals persists far outside the typical definition, perhaps due to the non-circular Fermi surface.

Therefore, this study has demonstrated that the shape of the Fermi surface can have profound effects on the phenomena observed within the unconventional regimes. It is crucial to consider the shape of the Fermi surface within any model of such systems. In particular, the scales over which ballistic effects are observed may be enhanced by the symmetry of the Fermi surface, indicating that the Fermi surface should be carefully considered in interpreting possible signals of other unconventional transport effects, such as those of electron hydrodynamics.

In the second part of the thesis, I studied electron transport in the magnetic delafossite metal $PdCrO_2$, in which nearly free and Mott-localised electrons exist in alternating layers, forming a natural heterostructure that is of high interest for the study of electron transport. However, studying microstructured devices of $PdCrO_2$ is technically quite challenging. A new method of fabricating 'free standing' microstructures overcame this challenge and enabled me to explore this new experimental area.

$PdCrO_2$ exhibits a Planckian bound in a wide range of temperatures from 200 K to 500 K. The high energy electron irradiation experiment performed in $PdCrO_2$ proved the theoretical suggestion that the Planckian bound is intrinsically associated with an inelastic scattering. It provides a novel perspective to the search for a universal law to account for Planckian dissipation.

The new method of device fabrication also allowed studying unconventional transport regimes in $PdCrO_2$. The observed resistivity behaviour at first sight implies a hydrodynamic regime, however, the detailed analysis and careful comparison with non-magnetic delafossite metals demonstrates the importance of considering the influence of ballistic physics on the observed properties.

The careful comparison of $PdCrO_2$ magnetotransport with that of the non-magnetic sister compound $PdCoO_2$ showed the strong impact of the coupling between conductive and magnetic layers on the transport. The SdH

oscillations observed in $PdCrO_2$ exhibit completely different results to the dHvA effect examined previously [76]. It gives an unexpected frequency not seen in the dHvA effect and also does not obey the temperature Lifshitz-Kosevich dependence.

The exotic coupling between conductive and magnetic layers in $PdCrO_2$ has been discovered in Ref. [82]. However, its influence on both magnetic and conductive properties is not completely understood. The magnetic structure of $PdCrO_2$ is rather complex and was studied in detail using powder and single-crystal neutron diffraction. However, all previous inelastic neutron scattering measurements were limited to powder samples [93]. The observed spectrum had additional broadening, which the linear spin-wave calculations could not reproduce and may be due to Kondo or magnon-phonon interactions. Details of the low-energy spectrum are also not known. Moreover, determining the weak out-of-plane interactions is also difficult using the powder data and requires Q-resolved single-crystal measurements. For this reason it is very important to carry out single crystal inelastic neutron scattering on $PdCrO_2$.

Figure 7.1: Part of the mosaic consists of $PdCrO_2$ single crystals on the Al sample holder for inelastic neutron scattering experiment.

However, this will not be easy, because the experiment will require 0.3 g of $PdCrO_2$. As $PdCrO_2$ grows in tiny single crystals with a typical weight of around 0.01 g, preparing samples for this experiment is a big challenge.

Thus, the final sample for the scattering experiment is a mosaic consisting of around thirty coaligned single crystals. Part of this mosaic structure on an Al plate is shown in fig. 7.1.

The experiment has been held up by the temporary closure of the NIST reactor in the USA, but it is in my opinion the most important piece of future work that needs to be performed on $PdCrO_2$. It can determine the exchange interactions and give further insight into the coupling between the conduction electrons and the Mott layer, by studying the way that it influences the spin dynamics. This should in turn help understand the unusual features in the transport data that I have reported in this thesis.

Bibliography

[1] L. Pfeiffer, K. W. West, H. L. Stormer, and K. W. Baldwin, *Electron mobilities exceeding 10^7 cm^2/Vs in modulation-doped GaAs*, Applied Physics Letters **55**, 1888 (1989).

[2] K. I. Bolotin, K. J. Sikes, J. Hone, H. L. Stormer, and P. Kim, *Temperature-dependent transport in suspended graphene*, Phys. Rev. Lett. **101**, 096802 (2008).

[3] C. R. Dean, A. F. Young, M. I. Meric, C. Lee, L. Wang, S. Sorgenfrei, K. Watanabe, T. Taniguchi, P. Kim, K. L. Shepard, and J. Hohe, *Boron nitride substrates for high-quality graphene electronics*, Nature Nanotechnology **5**, 722 (2010).

[4] T. Liang, Q. Gibson, M. N. Ali, M. Liu, R. J. Cava, and N. P. Ong, *Ultrahigh mobility and giant magnetoresistance in the Dirac semimetal Cd_3As_2*, Nature Materials **14**, 280 (2015).

[5] A. P. Mackenzie, *The properties of ultrapure delafossite metals*, Rep. Prog. Phys. **80**, 032501 (2017).

[6] R. D. Shannon, C. T. Prewitt, and D. B. Rogers., *Chemistry of noble metal oxides. II. Crystal structures of platinum cobalt dioxide, palladium cobalt dioxide, coppper iron dioxide, and silver iron dioxide*, Inorganic Chemistry **10**, 719 (1971).

[7] R. D. Shannon, D. B. Rogers, C. T. Prewitt, and J. L. Gillson., *Chemistry of noble metal oxides. III. Electrical transport properties and crys-*

tal chemistry of ABO_2 compounds with the delafossite structure, Inorganic Chemistry **10**, 723 (1971).

[8] R. D. Shannon, D. B. Rogers, and C. T. Prewitt, *Chemistry of noble metal oxides. I. Syntheses and properties of ABO_2 delafossite compounds*, Inorganic Chemistry **10**, 713 (1971).

[9] M. Tanaka, M. Hasegawa, and H. Takei, *Crystal growth of $PdCoO_2$, $PtCoO_2$ and their solid-solution with delafossite structure*, J. Cryst. Growth **4**, 440 (1997).

[10] M. Tanaka, M. Hasegawa, and H. Takei, *Growth and anisotropic physical properties of $PdCoO_2$ single crystals*, J. Phys. Soc. Japan **65**, 3973 (1996).

[11] H. Takatsu, S. Yonezawa, S. Mouri, S. Nakatsuji, K. Tanaka, and Y. Maeno, *Roles of High-Frequency Optical Phonons in the Physical Properties of the Conductive Delafossite $PdCoO_2$*, Journal of the Physical Society of Japan **76**, 104701 (2007).

[12] H. Takatsu, S. Yonezawa, C. Michioka, K. Yoshimura, and Y. Maeno, *Anisotropy in the magnetization and resistivity of the metallic triangular-lattice magnet $PdCrO_2$*, Journal of Physics: Conference Series **200**, 012198 (2010).

[13] P. Drude, *Zur elektronentheorie der metalle*, Annalen der physik **306**, 566 (1900).

[14] J. M. Ziman, *Electrons and phonons. The theory of transport phenomena in solids*, Oxford University Press, Amen House, London E.C.4, 1960.

[15] E. Grüneisen, *Die Abhängigkeit des elektrischen Widerstandes reiner Metalle von der Temperatur*, Annalen der Physik **450**, 530 (1933).

[16] N. W. Ashcroft and N. D. Mermin, *Solid State Physics*, Harcourt College Publisher, 1976.

[17] P. A. Schroeder, *Low-temperature electron transport properties of the alkaline metals*, Physica B + C **109**, 1901 (1982).

[18] A. H. MacDonald, R. Taylor, and D. J. W. Geldart, *Umklapp electron--electron scattering and the low-temperature electrical resistivity of the alkali metals*, Phys. Rev. B **23**, 2718 (1981).

[19] A. A. Abrikosov, *Fundamentals of the theory of metals*, Elsevier Science Publisher, 1988.

[20] M. Polini and G. Vignale, *The quasiparticle lifetime in a doped graphene sheet*, No-nonsense Physicist , 107 (2016).

[21] N. E. Hussey, A. P. Mackenzie, J. R. Cooper, Y. Maeno, S. Nishizaki, and T. Fujita, *Normal-state magnetoresistance of Sr_2RuO_4*, Physical Review B **57**, 5505 (1998).

[22] M. Tanaka, M. Hasegawa, T. Higuchi, T. Tsukamoto, Y. Tezuka, S. Shin, and H. Takei, *Origin of the metallic conductivity in $PdCoO_2$ with delafossite structure*, Physica B **245**, 157 (1998).

[23] T. Higuchi, T. Tsukamoto, M. Tanaka, H. Ishii, K. Kanai, Y. Tezuka, S. Shin, and H. Takei, *Photoemission study on $PdCoO_2$*, Journal of Electron Spectroscopy and Related Phenomena **92**, 71 (1998).

[24] T. Higuchi, D. Baba, Y. Yokoyama, M. Hasegawa, H. Takei, A. Fukushima, S. Shin, and T. Tsukamoto, *Electronic Structure of Delafossite-Type Oxide $PtCoO_2$ by Resonant-Photoemission Spectroscopy*, Japanese Journal of Applied Physics **42**, 5698 (2003).

[25] V. Eyert, R. Frésard, and A. Maignan, *On the Metallic Conductivity of the Delafossites $PdCoO_2$ and $PtCoO_2$*, Chem. Mater **20**, 2370 (2008).

[26] A. Damascelli, *Probing the Electronic Structure of Complex Systems by ARPES*, Physica Scripta **T109**, 61 (2004).

[27] H. J. Noh, J. Jeong, J. Jeong, E.-J. Cho, S. B. Kim, K. Kim, B. I. Min, and H.-D. Kim, *Anisotropic Electric Conductivity of Delafossite $PdCoO_2$ Studied by Angle-Resolved Photoemission Spectroscopy*, Phys. Rev. Lett. **102**, 256404 (2009).

[28] P. Kushwaha, V. Sunko, P. J. W. Moll, L. Bawden, J. M. Riley, N. Nandi, H. Rosner, M. P. Schmidt, F. Arnold, E. Hassinger, T. K. Kim, M. Hoesch, A. P. Mackenzie, and P. D. C. King, *Nearly free electrons in a 5d delafossite oxide metal*, Science Advances **1**, e1500692 (2015).

[29] C. W. Hicks, A. S. Gibbs, A. P. Mackenzie, H. Takatsu, Y. Maeno, and E. A. Yelland, *Quantum Oscillations and High Carrier Mobility in the Delafossite $PdCoO_2$*, Phys. Rev. Lett. **109**, 116401 (2012).

[30] F. Arnold, M. Naumann, H. Rosner, N. Kikugawa, D. Graf, L. Balicas, T. Terashima, S. Uji, H. Takatsu, S. Khim, A. P. Mackenzie, and E. Hassinger, *Fermi surface of $PtCoO_2$ from quantum oscillations and electronic structure calculations*, Phys. Rev. B **101**, 195101 (2020).

[31] K. P. Ong, J. Zhang, J. S. Tse, and P. Wu, *Origin of anisotropy and metallic behavior in delafossite $PdCoO_2$*, Phys. Rev. B **81**, 115120 (2010).

[32] N. Nandi, T. Scaffidi, P. Kushwaha, S. Khim, M. E. Barber, V. Sunko, F. Mazzola, P. D. C. King, H. Rosner, P. J. W. Moll, M. König, J. E. Moore, S. Hartnoll, and A. P. Mackenzie, *Unconventional Magneto--Transport in Ultrapure $PdCoO_2$ and $PtCoO_2$*, npj Quantum Materials **3**, 1 (2018).

[33] J. Bass, W. P. P. Jr, and P. A. Schroeder, *The temperature-dependent electrical resistivities of the alkali metals*, Rev. Mod. Phys. **62**, 645 (1990).

[34] R. Daou, R. Frésard, V. Eyert, S. Hébert, and A. Maignan, *Unconventional aspects of electronic transport in delafossite oxides*, Science and Technology of Advanced Materials **18**, 919 (2017).

[35] R. Daou, R. Frésard, S. Hébert, and A. Maignan, *Large anisotropic thermal conductivity of the intrinsically two-dimensional metallic oxide $PdCoO_2$*, Phys. Rev. B **91**, 041113 (2015).

[36] V. Sunko, P. H. McGuinness, C. S. Chang, E. Zhakina, S. Khim, C. E. Dreyer, M. Konczykowski, H. Borrmann, P. J. W. Moll, M. König, D. A. Muller, and A. P. Mackenzie, *Controlled Introduction of Defects to Delafossite Metals by Electron Irradiation*, Phys. Rev. X **10**, 021018 (2020).

[37] S. Reyntjens and R. Puers, *A review of focused ion beam applications in microsystem technology*, Journal of Micromechanics and Microengineering **11**, 287 (2001).

[38] D. P. Basile, R. Boylan, B. Baker, K. Hayes, and D. Soza, *Fibxtem—Focussed Ion Beam Milling for TEM Sample Preparation*, MRS Proceedings **254**, 23 (1991).

[39] K. Narayan and S. Subramaniam, *Focused ion beams in biology*, Nature methods **12**, 1021 (2015).

[40] R. Clampitt, K. L. Aitken, and D. K. Jefferies, *Intense field-emission ion source of liquid metals*, Journal of Vacuum Science and Technology **12**, 1208 (1975).

[41] R. L. Seliger, J. W. Ward, V. Wang, and R. L. Kubena, *A high-intensity scanning ion probe with submicrometer spot size*, Applied Physics Letters **34**, 310 (1979).

[42] N. S. Smith, W. P. Skoczylas, S. M. Kellogg, D. E. Kinion, P. P. Tesch, O. Sutherland, A. Aanesland, and R. W. Boswell, *High brightness inductively coupled plasma source for high current focused ion beam applications*, Journal of Vacuum Science & Technology B: Microelectronics and Nanometer Structures Processing, Measurement, and Phenomena **24**, 2902 (2006).

[43] K. Gamo, N. Takakura, N. Samoto, R. Shimizu, and S. Namba, *Ion beam assisted deposition of metal organic films using focused ion beams*, Japanese Journal of Applied Physics **23**, L293 (1984).

[44] J. M. D. Teresa, R. Córdoba, A. Fernández-Pacheco, O. Montero, P. Strichovanec, and M. R. Ibarra, *Origin of the difference in the resistivity of as-grown focused-ion-and focused-electron-beam-induced Pt nanodeposits*, Journal of Nanomaterials **2009**, 1 (2009).

[45] A. Reguer, F. Bedu, D. Tonneau, H. Dallaporta, M. Prestigiacomo, A. Houel, and P. Sudraud, *Structural and electrical studies of conductive nanowires prepared by focused ion beam induced deposition*, Journal of Vacuum Science & Technology B: Microelectronics and Nanometer Structures Processing, Measurement, and Phenomena **26**, 175 (2008).

[46] M. E. Barber, *Uniaxial Stress Technique and Investigations into Correlated Electron Systems*, PhD Thesis, University of St Andrews (2017).

[47] N. Nandi, *Can Hydrodynamic Electrons Exist in a Metal? A Case Study of the Delafossite Metals $PdCoO_2$ and $PtCoO_2$*, PhD thesis, TU Dresden 2019 .

[48] L. Nordheim, *The Anomalous Skin Effect and the Reflectivity of Metals I II*, Acta Scientiae et Industriae **131** (1934).

[49] K. Fuchs, *The conductivity of thin metallic films according to the electron theory of metals*, Mathematical Proceedings of the Cambridge Philosophical Society **34**, 100–108 (1938).

[50] T. Thornton, *Ballistic Transport in GaAs Quantum Wires - a Short History*, Superlattices and Microstructures **23**, 601 (1998).

[51] S. Masubuchi, K. Iguchi, T. Yamaguchi, M. Onuki, M. Arai, K. Watanabe, T. Taniguchi, and T. Machida, *Boundary Scattering in Ballistic Graphene*, Phys. Rev. Lett. **109**, 036601 (2012).

[52] P. J. W. Moll, P. Kushwaha, N. Nandi, B. Schmidt, and A. P. Mackenzie, *Evidence for hydrodynamic electron flow in $PdCoO_2$*, Science **351**, 1061 (2016).

[53] M. D. Bachmann, A. L. Sharpe, A. W. Barnard, C. Putzke, M. König, S. Khim, D. Goldhaber-Gordon, A. P. Mackenzie, and P. J. W. Moll, *Super-geometric electron focusing on the hexagonal Fermi surface of $PdCoO_2$*, Nature Communications **10**, 1 (2019).

[54] Y. V. Sharvin, *A Possible Method for Studying Fermi Surfaces*, Journal of Experimental and Theoretical Physics **48** (1965).

[55] M. D. Bachmann, *Manipulating Anisotropic Transport and Superconductivity by Focused Ion Beam Microstructuring*, PhD Thesis, 2019, The University of St Andrews, UK .

[56] J. Wu, H. P. Nair, A. T. Bollinger, X. He, I. Robinson, N. J. Schreiber, K. M. Shen, D. G. Schlom, and I. Bovzovic, *Electronic nematicity in Sr_2RuO_4*, Proceedings of the National Academy of Sciences **117**, 10654 (2020).

[57] R. A. Borzi, S. A. Grigera, J. Farrell, R. S. Perry, S. J. S. Lister, S. L. Lee, D. A. Tennant, Y. Maeno, and A. P. Mackenzie, *Formation of a Nematic Fluid at High Fields in $Sr_3Ru_2O_7$*, Science **315**, 214 (2007).

[58] L. J. van der Pauw, *A Method of Measuring the Resistivity and Hall Coefficient on Lamellae of Arbitrary Shape*, Philips Technical Review **20**, 220 (1958).

[59] H. C. Montgomery, *Method for Measuring Electrical Resistivity of Anisotropic Materials*, Journal of Applied Physics **42**, 2971 (1971).

[60] G. Timp, H. U. Baranger, P. D. Vegvar, J. E. Cunningham, R. E. Howard, R. Behringer, and P. M. Mankiewich, *Propagation around a Bend in a Multichannel Electron Waveguide*, Phys. Rev. Lett. **60**, 2081 (1988).

[61] N. Goel, J. Graham, J. C. Keay, K. Suzuki, S. Miyashita, M. B. Santos, and Y. Hirayama, *Ballistic transport in InSb mesoscopic structures*, Physica E-low-dimensional Systems & Nanostructures **26**, 455 (2005).

[62] V. Daumer, I. Golombek, M. Gbordzoe, E. G. Novik, V. Hock, C. R. Becker, H. Buhmann, and L. W. Molenkamp, *Quasiballistic transport in HgTe quantum-well nanostructures*, Appl. Phys. Lett. **83**, 1376 (2003).

[63] C. Bock, S. Weingart, E. Karaissaridis, U. Kunze, F. Speck, and T. Seyller, *Influence of structural properties on ballistic transport in nanoscale epitaxial graphene cross junctions*, Nanotechnology **23**, 395203 (2012).

[64] Y. Hirayama, T. Saku, S. Tarucha, and Y. Horikoshi, *Ballistic electron transport in macroscopic four-terminal square structures with high mobility*, Applied Physics Letters **58**, 2672 (1991).

[65] P. H. McGuinness, E. Zhakina, M. König, M. D. Bachmanns, C. Putzke, P. J. W. Moll, S. Khim, and A. P. Mackenzie, *Low-symmetry non-local transport in microstructured squares of delafossite metals*, arXiv preprint **arXiv:2111.00985** (2021).

[66] P. H. McGuinness, *Probing Unconventional Transport Regimes in Delafossite Metals*, PhD Thesis, University of St Andrews (2021).

[67] R. Landauer, *Spatial variation of currents and fields due to localized scatterers in metallic conduction*, IBM Journal of Research and Development **1**, 223 (1957).

[68] M. Buttiker, *Symmetry of electrical conduction*, IBM Journal of Research and Development **32**, 317 (1988).

[69] S. Bandyopadhyay, *Physics of Nanostructured Solid State Devices*, Springer Science and Business Media, 2012.

[70] L. Banszerus, M. Schmitz, S. Engels, M. Goldsche, K. Watanabe, T. Taniguchi, B. Beschoten, and C. Stampfer, *Ballistic Transport Exceeding 28 μm in CVD Grown Graphene*, Nano Letters **16**, 1387 (2016).

[71] T. Sakamoto, Y. Takagaki, K. Gamo, S. Namba, S. Takaoka, and K. Murase, *Impurity and boundary roughness scattering in GaAs-Al_xGa_{1-x} electron waveguides*, Solid State Communications **80**, 535 (1991).

[72] Y. Takagaki, T. Sakamoto, K. Gamo, S. Namba, S. Takaoka, and K. Murase, *Ballistic mean free path in GaAs-AlGaAs electron waveguides*, Superlattices and Microstructures **8**, 97 (1990).

[73] J. A. N. Bruin, H. Sakai, R. S. Perry, and A. P. Mackenzie, *Similarity of Scattering Rates in Metals Showing T-Linear Resistivity*, Science **339**, 804 (2013).

[74] H. Takatsu and Y. Maeno, *Single crystal growth of the metallic triangular-lattice antiferromagnet $PdCrO_2$*, Journal of Crystal Growth **312**, 3461–3465 (2010).

[75] D. Billington, D. Ernsting, T. Millichamp, C. Lester, S. B. Dugdale, D. Kersh, J. A. Duffy, S. R. Giblin, J. W. Taylor, P. Manuel, D. D. Khalyavin, and H. Takatsu, *Magnetic frustration, short-range correlations and the role of the paramagnetic Fermi surface of $PdCrO_2$*, Scientific Reports **5**, 1 (2015).

[76] C. W. Hicks, A. S. Gibbs, L. Zhao, P. Kushwaha, H. Borrmann, A. P. Mackenzie, H. Takatsu, S. Yonezawa, Y. Maeno, and E. A. Yelland, *Quantum oscillations and magnetic reconstruction in the delafossite $PdCrO_2$,* Physical Review B **92**, 014425 (2015).

[77] F. Lechermann, *Hidden Mott insulator in metallic $PdCrO_2$*, Phys. Rev. Materials **2**, 085004 (2018).

[78] M. Mekata, T. Sugino, A. Oohara, Y. Oohara, and H. Yoshizawa, *Magnetic structure of antiferromagnetic $PdCrO_2$ possible degenerate helices on a rhombohedral lattice*, Physica B **213**, 221 (1995).

[79] H. Takatsu, G. Nénert, H. Kadowaki, H. Yoshizawa, M. Enderle, S. Yonezawa, Y. Maeno, J. Kim, N. Tsuji, M. Takata, Y. Zhao, M. Green, and C. Broholm, *Magnetic structure of the conductive triangular-lattice antiferromagnet $PdCrO_2$*, Phys. Rev. B **89**, 104408 (2014).

[80] D. Sun, D. A. Sokolov, J. M. Bartlett, J. Sannigrahi, S. Khim, P. Kushwaha, D. D. Khalyavin, P. Manuel, A. S. Gibbs, H. Takagi, A. P. Mackenzie, and C. W. Hicks, *Magnetic frustration and spontaneous rotational symmetry breaking in $PdCrO_2$,* Phys. Rev. B **100**, 094414 (2019).

[81] J. A. Sobota, K. Kim, H. Takatsu, M. Hashimoto, S.-K. Mo, Z. Hussain, T. Oguchi, T. Shishidou, Y. Maeno, B. I. Min, and Z.-X. Shen, *Electronic structure of the metallic antiferromagnet $PdCrO_2$ measured by angle-resolved photoemission spectroscopy*, Phys. Rev. B **88**, 125109 (2013).

[82] V. Sunko, F. Mazzola, S. Kitamura, S. Khim, P. Kushwaha, O. Clark, M. Watson, I. Marković, D.Biswas, L. Pourovskii, T. Kim, T.-L. Lee, P. Thakur, H.Rosner, A. Georges, R. Moessner, T. Oka, A. Mackenzie, and P. King, *Probing spin correlations using angle resolved photoemission in a coupled metallic/Mott insulator system*, Science Advances **6**, 611 (2020).

[83] H.-J. Noh, J. Jeong, B. Chang, D. Jeong, H. S. Moon, E.-J. Cho, J. M. Ok, J. S. Kim, K. Kim, B. I. Min, H. K. Lee, J.-Y. Kim, B.-G. Park, H.-D. Kim, and S. Lee, *Direct observation of localized spin antiferromagnetic transition in $PdCrO_2$ by angle-resolved photoemission spectroscopy*, Scientific Reports **4**, 3680 (2014).

[84] J. M. Ok, Y. J. Jo, K. Kim, T. Shishidou, E. S. Choi, H.-J. Noh, T. Oguchi, B. I. Min, and J. S. Kim, *Quantum Oscillations of the Metallic Triangular-Lattice Antiferromagnet $PdCrO_2$*, Phys. Rev. Lett. **111**, 176405 (2013).

[85] J. R. Reitz, *Magnetic breakdown in metals*, Journal of Physics and Chemistry of Solids **25**, 53 (1964).

[86] H. Takatsu, H. Yoshizawa, S. Yonezawa, and Y. Maeno, *Critical behavior of the metallic triangular-lattice Heisenberg antiferromagnet $PdCrO_2$*, Phys. Rev. B **79**, 104424 (2009).

[87] R. Daou, R. Frésard, S. Hébert, and A. Maignan, *Impact of short-range order on transport properties of the two-dimensional metal $PdCrO_2$*, Phys. Rev. B **92**, 245115 (2015).

[88] E. H. Hall, *XVIII. On the Rotational Coefficient in nickel and cobalt*, The London, Edinburgh, and Dublin Philosophical Magazine and Journal of Science **12**, 157 (1881).

[89] R. Karplus and J. M. Luttinger, *Hall Effect in Ferromagnetics*, Phys. Rev. **95**, 1154 (1954).

[90] D. Boldrin and A. Wills, *Anomalous Hall Effect in Geometrically Frustrated Magnets*, Advances in Condensed Matter Physics **2012** (2012).

[91] Y. Taguchi, Y. Oohara, H. Yoshizawa, N. Nagaosa, and Y. Tokura, *Spin Chirality, Berry Phase, and Anomalous Hall Effect in a Frustrated Ferromagnet*, Science **291**, 2573 (2001).

[92] H. Takatsu, S. Yonezawa, S. Fujimoto, and Y. Maeno, *Unconventional Anomalous Hall Effect in the Metallic Triangular-Lattice Magnet Pd-CrO_2*, Phys. Rev. Lett. **105**, 137201 (2010).

[93] M. D. Le, S. Jeon, A. I. Kolesnikov, D. J. Voneshen, A. S. Gibbs, J. S. Kim, J. Jeong, H. J. Noh, C. Park, J. Yu, T. Perring, and J. G. Park, *Magnetic interactions in $PdCrO_2$ and their effects on its magnetic structure*, Phys. Rev. B **98**, 024429 (2018).

[94] G. Policastro, D. T. Son, and A. O. Starinets, *Shear Viscosity of Strongly Coupled N=4 Supersymmetric Yang-Mills Plasma*, Phys. Rev. Lett. **87**, 081601 (2001).

[95] S. Chakravarty, *Quantum critical fluctuations, Planckian dissipation, and compactification scale*, arXiv preprint **arXiv:1907.12163** (2019).

[96] S. Sachdev and B. Keimer, *Quantum criticality*, Physics today **64**, 29 (2011).

[97] R. E. Peierls, *Quantum theory of solids*, Clarendon Press, 1996.

[98] S. A. Hartnoll and A. P. Mackenzie, *Planckian Dissipation in Metals*, arXiv preprint **arXiv:2107.07802** (2021).

[99] S. A. Hartnoll, *private communication*, (2021).

[100] E. H. Hwang and S. D. Sarma, *Linear-in-T resistivity in dilute metals: A Fermi liquid perspective*, Physical Review B **99**, 085105 (2019).

[101] C. H. Mousatov and S. A. Hartnoll, *Phonons, electrons and thermal transport in Planckian high T_C materials*, npj Quantum Materials **6**, 1 (2021).

[102] O. Gunnarsson, M. Calandra, and J. E. Han, *Colloquium: Saturation of electrical resistivity*, Rev. Mod. Phys. **75**, 1085 (2003).

[103] F. D. M. Haldane, *Fermi-surface geometry and Planckian dissipation*, arXiv preprint **arXiv:1811.12120** (2018).

[104] D. Schoenberg, *Magnetic oscillations in metals*, Cambridge University Press, 1984.

[105] N. P. Ong, *Geometric interpretation of the weak-field Hall conductivity in two-dimensional metals with arbitrary Fermi surface*, Phys. Rev. B **43**, 193 (1991).

[106] X. Deng, J. Mravlje, R. Žitko, M. Ferrero, G. Kotliar, and A. Georges, *How Bad Metals Turn Good: Spectroscopic Signatures of Resilient Quasiparticles*, Phys. Rev. Lett. **110**, 086401 (2013).

[107] X. Deng, K. Haule, and G. Kotliar, *Transport Properties of Metallic Ruthenates: A DFT + DMFT Investigation*, Phys. Rev. Lett. **116**, 256401 (2016).

[108] R. N. Gurzhi, *HYDRODYNAMIC EFFECTS IN SOLIDS AT LOW TEMPERATURE*, Soviet Physics Uspekhi **11**, 255 (1968).

[109] A. Andreev, S. A. Kivelson, and B. Spivak, *Hydrodynamic description of transport in strongly correlated electron systems*, Phys. Rev. Lett. **106**, 256804 (2011).

[110] A. Lucas and S. A. Hartnoll, *Resistivity bound for hydrodynamic bad metals*, Proceedings of the National Academy of Sciences **114**, 11344 (2017).

[111] Y. G. Gurevich and O. L. Mashkevich, *The electron-phonon drag and transport phenomena in semiconductors*, Physics Reports **181**, 327 (1989).

[112] Y. B. Kudasov, *Skew band structure and anomalous conductivity of* $PdCrO_2$, arxiv.org preprint **arXiv:2006.05453** (2020).

[113] M. D. Bachmann, A. L. Sharpe, A. W. Barnard, C. Putzke, T. Scaffidi, N. Nandi, S. Khim, M. König, D. Goldhaber-Gordon, A. P. Mackenzie, and P. J. W. Moll1, *Directional ballistic transport in the two-dimensional metal $PdCoO_2$*, arXiv preprint **arXiv:2103.01332**.

[114] C. Q. Cook and A. Lucas, *Electron hydrodynamics with a polygonal Fermi surface*, Phys. Rev. B **99**, 235148 (2019).

[115] A. Levchenko and J. Schmalian, *Transport properties of strongly coupled electron-phonon liquids*, arXiv preprint **arXiv:2005.09694** (2020).

[116] X. Huang and A. Lucas, *Electron-phonon hydrodynamics*, Phys. Rev. B **103**, 155128 (2021).

[117] D. A. Bandurin, I. Torre, R. K. Kumar, M. B. Shalom, A. Tomadin, A. Principi, G. H. Auton, E. Khestanova, K. S. Novoselov, I. V. Grigorieva, L. A. Ponomarenko, A. K. Geim, and M. Polini, *Negative local resistance caused by viscous electron backflow in graphene*, Science **351**, 1055 (2016).

[118] M. J. M. Jong and L. W. Molenkamp, *Hydrodynamic electron flow in high-mobility wires*, Phys. Rev. B **51**, 13389 (1995).

[119] K. R. Kumar, D. A. Bandurin, F. M. D. Pellegrino, Y. Cao, A. Principi, H. Guo, G. H. Auton, M. B. Shalom, L. A. Ponomarenko, G. Falkovich, and K. Watanabe, *Superballistic flow of viscous electron fluid through graphene constrictions*, Nature Phys **13**, 1182–1185 (2017).

[120] H. Guo, E. Ilseven, G. Falkovich, and L. S. Levitov, *Higher-than-ballistic conduction of viscous electron flows*, Proceedings of the National Academy of Sciences **114**, 3068 (2017).

[121] H. K. Pal and D. L. Maslov, *Necessary and sufficient condition for longitudinal magnetoresistance*, Phys. Rev. B **81**, 214438 (2010).

[122] Q. Li, B. T. Liu, Y. F. Hu, J. Chen, H. Gao, L. Shan, H. H. Wen, A. V. Pogrebnyakov, J. M. Redwing, and X. X. Xi, *Large Anisotropic Normal-State Magnetoresistance in Clean MgB_2 Thin Films*, Phys. Rev. Lett. **96**, 167003 (2006).

[123] S. Arsenijevic, J. M. Ok, P. Robinson, S. Ghannadzadeh, M. I. Katsnelson, J. S. Kim, and N. E. Hussey, *Anomalous Magnetothermopower in a Metallic Frustrated Antiferromagnet*, Phys. Rev. Lett. **116**, 087202 (2016).

[124] T. I. Mogilyuk and P. D. Grigoriev, *Magnetic oscillations of in-plane conductivity in quasi-two-dimensional metals*, Phys. Rev. B **98**, 045118 (2018).

[125] S. Hill, P. S. Sandhu, J. S. Qualls, J. S. Brooks, M. Tokumoto, N. Kinoshita, T. Kinoshita, and Y. Tanaka, *Bulk quantum Hall effect: Evidence that surface states play a key role*, Phys. Rev. B **55**, R4891 (1997).

[126] S. V. Demishev, J. Vanacken, L. Weckhuysen, F. Herlach, Y. Bruynseraede, and V. V. Moshchalkov, *The anomalous temperature dependence of the quantum oscillation amplitude in organic conductors $(ET)_2XHg(SCN)_4 (X = K, Tl)$*, EPL (Europhysics Letters) **42**, 455 (1998).